Modeling and Control of Controllable Electric Loads in Smart Grid

by

Mingxi Liu
B.Eng., Harbin Institute of Technology, 2010
M.A.Sc., University of Victoria, 2012

A Thesis Submitted in Partial Fulfillment of the
Requirements for the Degree of

DOCTOR OF PHILOSOPHY

in the Department of Mechanical Engineering

Modeling and Control of Controllable Electric Loads in Smart Grid

by

Mingxi Liu
B.Eng., Harbin Institute of Technology, 2010
M.A.Sc., University of Victoria, 2012

Supervisory Committee

Dr. Yang Shi, Supervisor
(Department of Mechanical Engineering)

Dr. Nedjib Djilali, Departmental Member
(Department of Mechanical Engineering)

Dr. Hong-Chuan Yang, Outside Member
(Department of Electrical & Computer Engineering)

Supervisory Committee

Dr. Yang Shi, Supervisor
(Department of Mechanical Engineering)

Dr. Nedjib Djilali, Departmental Member
(Department of Mechanical Engineering)

Dr. Hong-Chuan Yang, Outside Member
(Department of Electrical & Computer Engineering)

ABSTRACT

Renewable and green energy development is vigorously supported by most countries to suppress the continuously increasing greenhouse gas (GHG) emissions. However, as the total renewable capacity expands, the growth rate of emissions is not effectively restrained. An unforeseen factor contributing to this growth is the regulation service, which aims to mitigate power frequency deviations caused by the intermittent renewable power generation and unbalanced power supply and demand. Regulation services, normally issued by supply-side balancing authorities, leads to inefficient operations of regulating generators, thus directly contributing to the emissions growth. Therefore, it is urged to find solutions that can stabilize the power frequency with an increased energy using efficiency.

Demand response (DR) is an ideal candidate to solve this problem. The current smart grid infrastructure enables a high penetration of smart residential electric loads, including heating, ventilation, and air conditioning systems (HVACs), air conditioners (A/Cs), electric water heaters (EWHs), and plug-in hybrid electric vehicles (PHEVs). Beyond simply drawing power from the grid for local electric demand, those loads can also adjust their power consumption patterns by responding to the control signals sent to them. It has been proved that, if appropriately aggregated and controlled, power consumption of demand-side residential loads possesses a huge potential for providing regulation services. The research of DR is pivotal from the the application perspective due to the efficient usage of renewable energy generation and the high power quality. However, many problems remain open in this area due to the load heterogeneity, device physical constraints, and computational and communication restrictions. In order to move one step further toward industry applications, this PhD thesis is concerned with two cruxes in DR program design: Aggregation Modeling and Control; it deals with two main types of terminal loads: Thermostatically Controlled Appliances (TCAs) (Chapters 2-4) and PHEVs (Chapter 5).

This thesis proceeds with Chapter 1 by reviewing the state-of-the-art of DR. Then in Chapter 2, the focus is put on modeling and control of TCAs for secondary frequency control. In order to explicitly describe local TCA dynamics and to provide the aggregator a clear global view, TCAs are aggregated by directly stacking their individual dynamics. Terminal TCAs are assumed in a general case that an arbitrary number of TCAs are equipped with varying frequency drives (VFDs). A centralized model predictive control (MPC) scheme is firstly constructed. In the design, to tackle the TCA lockout effect and to facilitate the MPC scheme, a novel approach for converting time-integrated interdependent logic constraints into inequality constraints are proposed. Since a centralized MPC scheme may introduce non-trivial computational load by using this aggregation model, especially when the number of TCAs increases, a distributed MPC (DMPC) scheme is proposed. This DMPC scheme is validated through a more practical case study that all TCAs are subject to pure ON/OFF control.

Chapter 3 targets on aggregation modeling and control of TCAs for the provision of primary frequency control. To efficiently reduce the computational load to facilitate the primary frequency control, the explicit monitoring of terminal TCAs must be compromised. To this end, a 2-D population-based model is proposed, in which TCAs are clustered into state bins according to their temperature information and running status. Within the proposed aggregation framework, individual TCA dynamics' evolutions develop into TCA population migration probabilities, thus the computational load of the centralized controller is dramatically reduced. Based on this model, a centralized MPC scheme is proposed for the primary frequency control.

The previously proposed population-based model provides a promising direction for the centralized control. However, in traditional population-based model, TCA lockout effect can only be considered when implementing the control signals. This will cause a mismatch between the nominal control signals and the actually implemented ones. To conquer this, in Chapter 4, an improved population-based model is studied to explicitly formulate the TCA lockout effect in the aggregation model. A DMPC scheme is firstly constructed based on this model. Furthermore, since the predictions of regulation signals may not be available or they may include severe disturbances, a control scheme that does not require future regulation signals is urged. To this end, an optimal control scheme, in which a novel penalty is included to maximize the regulation capability, is proposed to facilitate the most practical scenario.

Another type of terminal loads that has a huge potential in providing grid services is PHEV. At this point, Chapter 5 presents the aggregation and charging control of

heterogeneous PHEVs for the provision of DR. In contrast to using battery state-of-charge (SOC) solely as the system state, a new aggregation model is proposed by introducing a novel concept, i.e., charging requirement index. This index combines the SOC with drivers' specified charging requirements, thus inherently providing the aggregation model with richer information. A centralized MPC scheme is proposed based on this novel model. Both of the model and controller are validated through an overnight valley-filling case study.

Finally, the conclusions of the thesis are summarized and future research topics are presented.

Contents

Supervisory Committee ii

Abstract iii

Table of Contents vii

List of Tables xii

List of Figures xiii

Acknowledgements xvi

Dedication xviii

Nomenclature xix

1 Introduction 1

1.1 Smart Grid and Demand Response (DR) 1

1.1.1 Overview 1

1.1.2 Categories of DRs 3

1.1.3 Benefits of DR 8

1.1.4 Policies Supporting DR and Some Rooted Barriers 10

1.2 Literature Review on DR 13

1.2.1 DR with TCAs 14

1.2.2 DR with PHEVs 19

1.3 Research Motivations and Contributions 22

1.4 Organization of the Thesis 24

2 Direct Aggregation and MPC for TCAs Providing Balancing Service 26

2.1 Introduction 26

2.1.1 Background and Literature Review 26

2.1.2 Research Objectives and Contributions 30

2.1.3 Chapter Organization 31

2.2 Centralized MPC Design 31

2.2.1 Thermal Dynamic Model of a Single TCA Unit 31

2.2.2 Centralized MPC Scheme for Balancing Signal Tracking (without considering lockout effect) 32

2.2.3 Centralized MPC Scheme Considering Lockout Effect 38

2.2.4 Interdependent Logic Conditions to Inequality Constraints . . 41

2.2.5 Case Study 49

2.3 DMPC Design 62

2.3.1 DMPC Scheme 62

2.3.2 Distributed Objective Function 64

2.3.3 State and Input Constraints 66

2.3.4 Lockout Effect Constraints 67

2.3.5 Control Scheme Description 69

2.3.6 Case Study 70

2.4 Conclusions 73

3 Population-Based Aggregation Model and MPC for a Large Population of TCAs 74

3.1 Introduction 74
    3.1.1 Background and Literature Review 74
    3.1.2 Research Objectives and Contributions 75
    3.1.3 Chapter Organization 76
3.2 Problem Formulation 77
    3.2.1 Second-Order TCA Dynamics 77
    3.2.2 2-D Population-Based Model 78
    3.2.3 Aggregate Dynamics 80
    3.2.4 Derivations of System Matrix $A(k)$ 81
    3.2.5 Other System Matrices and The Control Signal 87
3.3 Controller Design 88
    3.3.1 Centralized MPC Scheme 88
    3.3.2 Control Signal Implementation 92
3.4 Case Study 93
    3.4.1 Parameter Selection 93
    3.4.2 Desired Trajectory Construction 94
    3.4.3 System Performance and Analyses 95
3.5 Conclusion 100

4 Lockout-Induced Population-Based Aggregation Model and Control of Aggregated Heterogeneous TCAs 101

4.1 Introduction 101
    4.1.1 Background and Literature Review 101
    4.1.2 Research Objectives and Contributions 103
    4.1.3 Chapter Organization 104
4.2 Aggregation Model Development 104
    4.2.1 Lockout-Induced Population-Based Model 104

4.2.2 Control Vector $\mathscr{U}(k)$ 107

4.2.3 Input Matrix $\mathscr{B}(k)$ 107

4.2.4 System Matrix $\mathscr{A}(k)$ 108

4.2.5 Analytical Derivations of $\mathscr{A}(k)$ 110

4.2.6 System Output 113

4.3 DMPC Design 114

4.3.1 The DMPC Scheme 114

4.3.2 Constraints 120

4.3.3 DMPC Algorithm 121

4.3.4 Case Study 124

4.4 Optimal Control Design 129

4.4.1 Centralized MPC 129

4.4.2 Optimal Control 132

4.4.3 Control Signal Implementation 134

4.4.4 Case Study 135

4.5 Conclusions 138

5 Aggregation and Charging Control of PHEVs in Smart Grid: A Cyber-Physical Perspective 140

5.1 Introduction 140

5.1.1 Background and Literature Review 140

5.1.2 Research Objectives and Contributions 143

5.1.3 Chapter Organization 144

5.2 Aggregation Model Development 144

5.2.1 PHEV Battery Charging Model 144

5.2.2 Charging Requirement Index 144

5.2.3 Index-Based Aggregation Model 146

5.2.4 Analytical Derivation of the System Dynamic Function 147

5.3 Controller Design 158

5.3.1 Charging Profile 158

5.3.2 MPC Scheme 159

5.3.3 Control Signal Implementation 162

5.4 Case Study 163

5.4.1 Parameter Selection 163

5.4.2 System Performance and Analyses 164

5.5 Conclusion 169

6 Conclusions and Future Work **171**

6.1 Conclusions 171

6.2 Future Work 174

A Publications **176**

Bibliography **179**

List of Tables

Table 1.1 Classifications of DR programs. 4

Table 2.1 Truth table of $r_i(k+j|k)$, $r_i(k+j-1|k)$, $\psi_{i1}(j)$, and $\phi_{i1}(j)$. . . 46

Table 5.1 Monte Carlo simulation parameters. 156

Table 5.2 Simulation parameters. 163

List of Figures

Figure 1.1 The conceptual scheme of a smart grid for controlling TCAs. . 15
Figure 1.2 The conceptual scheme of a smart grid for controlling PHEVs' charging. 20
Figure 1.3 Organization of this thesis. 25

Figure 2.1 First-order ETP model. 32
Figure 2.2 Illustration of $t_{\mathrm{on}_i}(k)$ and $t_{\mathrm{off}_i}(k)$. 39
Figure 2.3 Ambient temperature profiles with different averages. 50
Figure 2.4 Construction of balancing signals (1000 TCAs, winter weather profile). 52
Figure 2.5 Indoor air temperature evolution (winter) responding to load following control signal. 53
Figure 2.6 Load following signal tracking (winter). 54
Figure 2.7 Control signals sent to TCAs in the load following tracking scenario. 54
Figure 2.8 Indoor air temperature evolution (spring) responding to load following signal. 56
Figure 2.9 Load following signal tracking (spring). 56
Figure 2.10 Indoor air temperature evolution (winter) responding to ACE signal. 58
Figure 2.11 ACE signal tracking (winter). 58

Figure 2.12 Control signals sent to TCAs in the ACE tracking scenario. . . 59
Figure 2.13 indoor air temperature of 20 agents (±2°C) and outdoor temperature. 71
Figure 2.14 Load balancing signal tracking performance. 72

Figure 3.1 The 2-D population-based model. 79
Figure 3.2 Indoor air temperature, building mass temperature, and ambient temperature. 95
Figure 3.3 Comparison of the desired trajectory and the aggregated power consumption under the proposed control protocol. 96
Figure 3.4 The desired trajectory tracking error. 96
Figure 3.5 Comparisons between the actual and calculated switchings. . . 97

Figure 4.1 Population migration by adding lockout bins. 105
Figure 4.2 Indoor air temperature evolution and ambient temperature. . . 126
Figure 4.3 Desired trajectory tracking and error. 126
Figure 4.4 Comparisons between the actual and calculated switchings. . . 128
Figure 4.5 Temperature evolution by employing three different controllers. 136
Figure 4.6 Regulation flexibility of three controllers. 137
Figure 4.7 Tracking error of three controllers. 137

Figure 5.1 Look-up chart for the Range-to-Range derivation of $A(u)$. . . . 151
Figure 5.2 4th-order curve fitting of $a_{55}(u_5)$. 155
Figure 5.3 Comparisons between the Monte Carlo simulations with the calculated probabilities. 158
Figure 5.4 Baseline load profile and optimal valley-filling profile per household. 159
Figure 5.5 Parameter distributions in the case study. 164
Figure 5.6 Valley-filling performance of three controllers. 165

Figure 5.7 Index trajectories of all 1000 PHEVs. 166

Figure 5.8 State trajectories. 167

Figure 5.9 Control signal trajectories of 10 state bins. 168

Figure 5.10Individual charging rate trajectories of all 1000 PHEVs. 169

Figure 5.11SOC trajectories of all 1000 PHEVs. 170

ACKNOWLEDGEMENTS

First of all, I would like to give Dr. Yang Shi, my supervisor, my sincere thanks for all of his help and encouragement during my Master's and PhD study. It was him who led me to the gate of academic research; it was him who taught me how to be a man; it was him who was always there whenever I needed. He is a sensitive researcher who can always spot the leading edge of his area; he is a rigorous professor that even a tiny mistake is unacceptable; he is also a painstaking supervisor who usually discusses with me on my research till late night. With no doubt, he is the best friend, with whom I can share the happiness and sadness. During my past six years study at the University of Victoria, Dr. Yang Shi selflessly provided me precious opportunities, greatly promoting me in my academic career.

I would like to thank the Supervisory Committee Members, Dr. Nedjib Djilali and Dr. Hong-Chuan Yang for their constructive comments. They have been continuously supporting and helping me since my PhD Candidacy Exam. I also want to express my appreciations to the External Member, Dr. Mo-Yuen Chow, for his insightful suggestions in improving this thesis.

I am delighted to have Dr. Zuomin Dong as the Chair of the Department of Mechanical Engineering at the University of Victoria. His help to me never ends since the first day I stepped into the campus.

Moreover, it is really my luck to know and work with my group members and friends in the Applied Control and Information Processing Lab at the University of Victoria. Past senior students, current professors or professional engineers, Dr. Hui Zhang, Dr. Ji Huang, Dr. Jian Wu, and Dr. Huiping Li will be my role models forever. I also want to thank Dr. Xiaotao Liu, Yiming Zhao, Bingxian Mu, Yuanye Chen, Chao Shen, Jicheng Chen, Kunwu Zhang, Wei Chen, Lei Zuo, Ying Li, Xiang Sheng, and Qianyan Shen for the happy time we have spent on this small island.

Thanks for my beautiful wife Jingwen Tang's love and care. Because of her, the long journey to the PhD degree has never been torturous. I will bear her words in mind for the rest of my life "*Growing is pipping, it is supposed to be tough.*"

At last, but the most importantly, I would like to thank my parents and all my families. They are always my solid backings. I love them all with all my heart.

Victoria, BC, Canada
April, 2016

To my beloved parents and Jingwen

Nomenclature

Abbreviations

ACE	Area Control Error
AGC	Automatic Generation Control
AMR	Automated Meter Reading
ARRA	American Recovery and Reinvestment Act
CHP	Combined Heating and Power
CPS	Cyber-Physical System
C&I	Commercial and Industrial
DLC	Direct Load Control
DMPC	Distributed Model Predictive Control
DOE	Department of Energy
DR	Demand Response
DSM	Demand Side Management
EIA	Energy Information Administration
EISA	Energy Independence & Security Act
EMS	Energy Management System
ETP	Equivalent Thermal Parameter
EV	Electric Vehicle
EWH	Electric Water Heater
FEA	Federal Energy Administration
FERC	Federal Energy Regulatory Commission
GHG	Greenhouse Gas
HVAC	Heating, Ventilation, and Air Conditioning
ICE	Intercontinental Exchange
ILC	Interruptible Load Control

INLP	Integer Nonlinear Programming
ISO	Independent System Operator
LMP	Locational Marginal Price
LTV	Linear Time-Varying
MHSE	Moving Horizon State Estimator
MINLP	Mixed-Integer Nonlinear Programming
MIQP	Mixed-Integer Quadratic Programming
MPC	Model Predictive Control
NIST	National Institute of Standards and Technology
NMPC	Nonlinear Model Predictive Control
PAP	Priority Action Plans
PHEV	Plug-in Hybrid Electric Vehicle
PV	Photovoltaic
QP	Quadratic Programming
RTO	Regional Transmission Operator
SGIP	Smart Grid Policy Panel
SOC	State-of-Charge
TCA	Thermostatically Controlled Appliance
TOU	Time-of-Use
VFD	Varying Frequency Drive
VG	Virtual Group
V2G	Vehicle-to-Grid
V2H	Vehicle-to-Home
V2V	Vehicle-to-Vehicle

Chapter 1

Introduction

This Chapter elaborates the background, state-of-the-art, and literature review of demand response (DR) in smart grid. It also details the motivations and contributions of this thesis. The organization of this thesis is presented at the end of this Chapter.

1.1 Smart Grid and Demand Response (DR)

1.1.1 Overview

Smart grid usually refers to the utility electricity delivery system which combines modern communication, computation, and transmission technologies. Different from the traditional unidirectional electricity grid, through the two-way digital communication network and computer processing technology, smart grid makes it possible to improve the efficiency, economics, and sustainability of the production and distribution of electricity in an automated fashion [1]. In old days, utilities have had to send technicians to terminal users to read meters, detect fault devices, and measure voltages. Nowadays, with smart meters and sensors equipped, the information can be automatically fed back to the utility. Furthermore, the two-way digital communication network also allows connected devices being controlled by the utility in order to achieve a high grid efficiency. The Department of Energy (DOE) of USA also defines some important functional characteristics for smart grid [2, 3]:

- **Self-healing** from power disturbance events, which reveals the grid reliability. Smart grid can make full use of the modern technology to improve fault detection and allow self-healing of the network without the intervention of technicians.
- Enabling **active participation by consumers** in DR programs. DR can improve the grid efficiency by providing ancillary services, e.g., regulation, load balancing, load adjustment, peak curtailment, and time-of-use (TOU) pricing.
- **Operating resiliently** against physical and cyber-attack.
- **Providing high-quality power** for 21st century needs. By integrating DR, the possibility of encountering poor power quality including blackouts, power cuts, and brownouts can be dramatically reduced.
- **Accommodating all generation and storage options**. Based on smart grid infrastructure and through DR programs, power generation intermittency caused by the penetration of renewable energy, e.g., photovoltaic (PV) arrays and wind farms, can be solved, which results in a full integration of renewable energy.
- **Enabling new products, services, and markets**.
- **Optimizing assets and operating efficiency**.

The above functional characteristics reveal the significant roles of smart grid in modern electricity grid and the key role of DR in smart grid. According to Federal

Energy Regulatory Commission (FERC) and DOE, DR is defined as [4,5]: "*Changes in electric usage by end-use customers from their normal consumption patterns in response to changes in the price of electricity over time, or to incentive payments designed to induce lower electricity use at times of high wholesale market prices or when system reliability is jeopardized.*". In the traditional wholesale market, the power of the supplier market was excessively large due to the inactive demand side of the market. Stated in [6], enabling DR can increase economic efficiency in electricity markets and improve system reliability. DR, enabled by the two-way digital communication network, provides end-users with opportunities to participate in the operation of electric grid, and enables them to contribute to achieving a higher-efficiency grid. The traditional electricity grid balances the power supply and demand by building regulating generators or adjusting rotational speeds of existing generators in the supply side; in contrast, in modern smart grid, DR plays an important role in balancing the electric power grid from the demand side. Traditionally, DR can be utilized to gain peak shaving and peak shifting by providing the end-users with TOU pricing, critical peak pricing, variable peak pricing, and critical peak rebates. The independent system operator (ISO) can also achieve direct load control (DLC) of the air conditioners (A/Cs), electric water heaters (EWHs), plug-in hybrid electric vehicles (PHEVs), etc., for other ancillary services by offering financial incentives or lower electricity bills to end-users.

1.1.2 Categories of DRs

In current market, various categories of DR programs exist to fulfill different objectives. According to the surveys released by FERC, the total number of classifications of DR programs increased from 12 in 2006 to 15 in 2008, and to 15^+ after 2012 [7,8]. In general, those programs can be divided into two main groups: incentive-based DR and time-/price-based DR, whose details are briefly summarized in Table 1.1. According to [7], the top four DR programs that possess over 80% potential peak reduction are as bolded in Table 1.1, thereinto, 29%, 24%, 15%, and 12% for load as capacity resource, interruptible load control (ILC), DLC, and TOU pricing, respectively. Those top four DR programs are detailed as follows.

Table 1.1: Classifications of DR programs.

Incentive-based programs	Time-based programs
• Demand bidding and buyback • **DLC** • Emergency demand response • **ILC** • **Load as capacity resource** • Non-spinning reserves • Regulation services • Spinning reserves	• Critical peak pricing with control • Critical peak pricing • Peak time rebate • Real-time pricing • **TOU pricing** • System peak response transmission tariff

1.1.2.1 DLC

DLC is one type of DR programs by which the program operator remotely shuts down or cycle a customer's electrical equipment on short notice. It is the most rapidly developing DR program, which is primarily offered to residential and small commercial customers, and has already been operating for at least three decades. Back to 1960s, a lot of utilities initialized, developed, and deployed large DLC programs and expanded those programs significantly during 1980s and 1990s. In 1985, 175 residential and 99 commercial DLC programs came into use. The 2006 FERC survey reported that 234 utilities in the US claimed the use of DLC programs [9]. In 2012, a total number of 489 new types of DLC programs, which was almost 25 times than the ILC, came into the market. After the boom in 2012, during the calendar year of 2013-2014, only 38 new types came out. And by prediction, through 2015 to 2017, only 18 new types of programs may come online.

Back to old days and currently, DLC programs are mainly designed for peak load reduction during the time of system peak demand. This type of service only requires a one-way switch to connect to the condensing unit of an A/C or the immersion element in an EWH. There exist two options of adjusting the demand: The first option is to simply shut down or adjust the duty cycle without changing the setpoint; in the second option, the utility can adjust the setpoint of an A/C or EWH in order to adjust the demand. After an event, the setpoint will be set back to the customer's preset value. For example, during the summer, the utility can remotely adjust the setpoint temperature upward to reduce demand. In some of the programs, the adjusting/shutting down number is also capped to protect the end-users' comfort level. In 2012 FERC survey [7], the peak reductions by DLC programs are 1638 MW, 6940 MW, 666 MW, and 534 MW for commercial & industrial (C&I), residential, wholesale, and others, respectively.

As the rapid development of smart grid technology and the deepening penetration of renewable energy generation, DLC gradually comes into use for providing ancillary services. These services are of importance from the perspectives of both the grid and customers. By receiving the ancillary services, e.g., balancing power supply and demand, intermittent generation of wind/solar energy is not necessary to be curtailed to fulfill the demand, instead, the demand can be efficiently adjusted to match the supply. Since this service requires a fast response, shutting down A/Cs or EWHs can immediately provide the required response. It is worth mentioning that, a single customer is not capable of providing this service due to its limited capacity. Thus aggregators between the ISO and customers must exist to aggregate the power consumption of a sufficient number of customers to match the supply. One issue in this program is that, customers' load may be adjusted downward, resulting in decreased bills, or upward, resulting in increased bills. However, these decreased or increased bills are solely based on the retail/wholesale price offered to the customers. Since this service deepens the penetration level of renewable energy generation, the wholesale market price will definitely be reduced. In long term, this reduced wholesale/retail price reflects a reduction in the electricity bill. In addition, the load of each customer is only slightly adjusted, thus no sensible difference is caused in the terminal side. To achieve this service, the two-way digital communication network in smart grid must exist and advanced meters that can measure and transfer data in short time period must be installed. Till July 2013, 45.8 million advanced meters, which is 30.2% of the total meters, have been installed across the US. With the ancillary service provided by this program and other technologies, in the US till April 2014, the wind energy generation had been expanded to 174.7 TWh, which is 4.25% of all generated electricity. The increasing rate is around 20% compared to the generation in 2013. Predicted by the DOE, almost 20% of all electricity generation will come from wind farm in 2030 [10]. According to the data collected from the Intercontinental Exchange (ICE) [11] and US Energy Information Administration (EIA) [12], the trend of the electricity wholesale price keeps going down since 2008.

1.1.2.2 ILC

ILC has been deployed for decades to adjust electricity consumption under tariffs or contracts that provide rate discounts or bill credits for customers agreeing to be curtailed or interrupted for the purpose of load reduction during system contingencies. In some instances, the demand reduction may be affected by actions of the ISO after notice to the customers in accordance with contractual provisions. Customers participating in this program must curtail their demand according to the contingencies, otherwise they will be penalized. However, the number of times or hours that a utility can call interruptions is capped. ILC is usually offered to large customers, which may range from 200 kW to 3 MW. Though employed for a long time, according to the 2012 survey [7], the total number of utilities providing ILC programs decreased from 183 in 2010 to 158 in 2012. In the survey, the reported potential peak reductions by ILC were 14268 MW, 45 MW, 685 MW and 649 MW for C&I, residential, wholesale market, and others, respectively. In this thesis, ILC will not be deployed because it is a mandatory and interruptible behaviour unilaterally decided by the ISO.

1.1.2.3 Load as Capacity Resource

In this program, terminal loads serve as the demand side resources that are committed to making pre-specified load reductions when system contingencies arise. Load as capacity resource becomes a dominant DR program in 2012 with the total capacity of 20000 MW, which is more than twice of the number in 2010. This type of program has the largest potential peak reductions in 2012, which were 2649 MW, 77 MW and 16600 MW for C&I, residential, and wholesale market, respectively.

1.1.2.4 TOU Pricing

TOU pricing program is the only one in the top four that is time-based. In this program, the electricity unit price varies by time period, and the time periods are typically longer than one hour within a 24-hour day. Among all DR programs, TOU rates reflect the average cost of generating and delivering power during those time periods. It is the most prevalent and oldest program, especially for residential users. Before TOU pricing becoming widely spread, flat electricity rate was the most common form, which was determined by the ISO or the regional transmission operator (RTO) according to the auction market. The highest bidding under the cap together with other lower biddings that can cover the consumption were the successful biddings. However, this scheme did not successfully protect the customers or the suppliers at all because, on the one hand, since the rate was flat, customers did not reduce their electricity use no matter what the price was. Consequently, the peak load was not reduced at all. On the other hand, suppliers barely made profit because peak plants only ran a few hours a year. As a result, as long as the peak demand is high, the electricity rate cannot be lowered. To solve this problem, some economists like William Hogan suggested to remove the bidding cap to protect the peak plants [13]. However, this action directly resulted in a price soaring like the high price in California, USA in 2000. For years, economists and policy makers struggled to solve the inelastic wholesale market from the supply side. After tons of failures, it was realized that this problem was due to the inactive demand side. If the customers could be notified about varying electricity rates, i.e., higher rate at peak hours and lower rate at off-peak hours, they might make adjustments accordingly, which can reduce the peak or move the peak.

Dating back to late 1970s and early 1980s, the Federal Energy Administration (FEA) started to sponsor 16 demonstration TOU pilots. Till now, the number of utilities offering residential TOU pricing increased slightly from 144 in 2010 to 151 in 2012, while the number of customers enrolled in this program increased dramatically from 1.1 million in 2010 to 2.1 million in 2012. The reported potential peak reductions are 6425 MW, 858 MW, 789 MW, and 69 MW for C&I, residential, wholesale, and others, respectively.

1.1.3 Benefits of DR

As detailed in the previous section, though in various forms, DR in general benefits not only the participants but also the electricity grid [7, 8, 14]. Firstly, the reliability of the electric grid can be well maintained by DR programs. This reliability refers to the electric system's capability of withstanding sudden disturbances, e.g., imbalance between power supply and demand. Some DR programs can be deployed to provide ancillary services, e.g., regulation and frequency response, spinning reserve and non-spinning reserve, which are similar to a generator except changing the demand instead of the supply. By participating in DR programs, end-users can help reduce the risk of outages, thus protecting the grid and themselves.

Secondly, DR allows a higher-level penetration of renewable energy [15]. The intermittent generation of renewable energy, e.g., PV array and wind farm, severely restricts its integration into the power grid. DR programs targeting at ancillary services can be deployed to effectively maintain the power and frequency balance between two sides. For example, in order to avoid the inefficient curtailment of wind generation, demand can be adjusted upward through DR programs [4], which can also serve as an option of peak shifting.

Thirdly, successful DR can provide congestion relief, improved reliability, and a lower capacity requirement, further resulting in a long-term wholesale electricity price reduction because of a more sophisticated utilization of available infrastructures and reduction of committing expensive generation units [15–18].

In addition, the successful implementation of DR can effectively reduce the wholesale energy prices and their volatility [19, 20]. Customers participating in the DR program can expect savings on electricity bill from two points of view: 1) incentives provided, and 2) long-term electricity price reduction.

Meanwhile, ISOs and distribution utilities can benefit from avoided generation cost as well as avoided or deferred transmission and distribution costs. Since DR can begin to serve in a relatively rapid fashion, they can contribute to the problem resolution on a shorter time frame than building new generation, transmission, or distribution infrastructure [9].

Finally, DR is promising in conservation effects, both directly from load reductions that are not made up at another time and indirectly from increased customer awareness of their energy usage and costs [21]. DR also has potential in environmental benefits by reducing emissions of generation plants during peak periods. However, reductions during peak periods should be balanced against possible emissions increases during off-peak hours, as well as from the increased use of on-site generation. If the implementation of DR contributes to reducing generation facility constructions, there may be additional environmental and aesthetic benefits. These conservation and environmental impacts can be either positive or negative, and will likely vary by region.

1.1.4 Policies Supporting DR and Some Rooted Barriers

Though, from the perspectives of economics and power grid reliability, DR programs show great benefits and promising development trends, the process of implementing DR programs to C&I and even residential customers is still in a low pace. To date, several acts have been issued to eliminate the barriers for entry and attracting more customers that are capable of providing DR. Take the US as an example, the US government boosts its pace to DR by the following sample policies.

- **FERC Order No. 719** [8, 22, 23]: Order No. 719 was issued on October 17, 2008 to amend its regulations under the Federal Power Act for improving the wholesale electricity market, specifically for the DR and market pricing during the shortage of operating reserve, long-term power contracting, market-monitoring policies, and responsiveness of ISO, RTO, and customers. Targeting at ancillary services, Order 719 states that 1) DR resources are required to meet necessary technical requirements; 2) DR resources are allowed to specify the frequency and duration of their service through the use of additional bidding parameters; 3) RTOs and ISOs need to perform a small DR resource assessment to evaluate the technical feasibility and value to the market of such smaller resources; 4) RTOs and ISOs accept biddings/offers from DR resources for ancillary services comparable to any other ancillary-service-capable resources. The above regulations modified and improved the existing rules for RTOs and ISOs and mandatorily require the customers be capable of providing these services.

- **FERC Order No. 745** [8, 24]: Order No. 745 was issued on March 15, 2011, in which FERC amended its regulation to ensure that the participated customers must be compensated for the service they provide at the market price for energy, referred to as the locational marginal price (LMP), in the case that they are capable of balancing power supply and demand and when dispatch of that DR is cost-effective. This approach helps to ensure the competitiveness of organized wholesale energy markets and remove barriers to the participation of DR resources, thus ensuring reasonable wholesale rates.

- **FERC Order No. 1000** [25]: Order No. 1000 was issued on July 21, 2011 to amend the transmission planning and cost allocation requirements in Order No. 890 to ensure that public utility transmission providers must consider all types of resources including DR on a comparable basis in transmission planning.

- **American Recovery and Reinvestment Act (ARRA)** [26]: The ARRA was issued on January 6, 2009. It allocated a significant amount of funding to the DR program in two areas: regional smart grid demonstration and utility-scale energy storage demonstration. The total funding provided by ARRA for the above projects was $4.5 billion.

Though the above acts and orders have improved the existing DR framework in diversified aspects, there still exist some rooted obstacles in the current situation.

Problems associated with different types of DR programs are different, however, some common ones for all programs can be briefly summarized as:

- **Lack of social acceptance**: customers, especially residential customers, are not well informed or educated to participate in DR programs. Specially for DLC, a certain number of residential users are not willing to be controlled by the local utility due to the privacy issue, though incentives are provided. Thus, it requires the government, ISOs, and the local utilities to strength the importance and benefits of DR from any related aspects.

- **Lack of incentive schemes**: incentives for most of the incentive-based DR programs are good enough. However, incentives for fast DR programs, like regulation services, is still not clear. During the service period, DR might adjust terminal power consumption downward, which results in a bill reduction. However, in some other cases, DR may need to adjust terminal power consumption upward. If only the bill reduction counted as incentives, it is hard to justify customers' financial benefits. Thus, an incentive scheme that is specifically designed for fast DR is urged.

- **Lack of uniform standards**: in the current situation, the types of communication protocols and response signals, even for the same type of program, vary according to different companies. This lack of uniform standards makes companies hard to collaborate, because of the duplication or totally different types of systems, inefficient information transfer of pricing and usage information, and the difference in response signals. In the US, the National Institute of Standards and Technology (NIST) has already noticed this problem and issued the Title XIII of the Energy Independence and Security Act (EISA) addressing the need for standards for communication and interoperability of the grid to enable the incorporation of DR and demand-side resources into grid operations. In 2009, FERC issued a Smart Grid Policy Statement that identified DR as one of four key functional priories for smart grid interoperability standards development. Recognizing the need for electricity providers to be able to communicate DR and distributed energy resource signals with each other and with customers, the Smart Grid Interoperability Panel (SGIP) sponsored several Priority Action Plans (PAPs) to develop common protocols for communicating.

- **Lack of efficient control approaches**: control approaches for TOU pricing programs are the ones decided by the customers. However, in DLC programs, control actions should be carried out by centralized controllers in ISOs or local utilities, or distributed controllers located with end-users. Take the centralized controlled balancing service for example, the power consumption of all end-users should be aggregated to match the supply curve. In order to control the power consumption of all participated loads, the centralized controller needs to collect the information from them, calculate the control actions, and dispatch the signals to them. Normally, the number of involved devices is huge, if the aggregation model is not appropriately designed, the control signal acquisition process may take a long time, thus not ready for real-time of fast response use. Hence, efficient aggregation models and control approaches are urged in this field.

1.2 Literature Review on DR

As previously discussed, DR is not a new concept and is developing rapidly in recent years. A rising number of researchers have actively conducted reviews and surveys discussing the history, basic concepts, benefits, classifications, and required infrastructure standards of DR [4, 14, 15, 22, 27–31]. Specifically, discussions on potential environmental benefits brought by DR can be found in [32,33]. Practicability of utilizing DR to deepen the penetration level of renewable energy is discussed in [15,34–36]. Analyses and discussions on issues of a DR-free electricity market and how DR can enhance the market functions can be found in [14,19,20,37,38]. The impact of DR on voltage profile is discussed in [39]. The US government carries out surveys annually to evaluate the achievements and offer outlooks of implementing DR programs [7–9,26]. Review and analysis of DR in industries are provided in [40], and in residential and commercial buildings can be found in [41]. Development trends of DR in different countries are discussed in [16, 17, 42–45]. Lawrence Berkeley National Laboratory releases a report summarizing the opportunities and challenges of using DR, especially DLC, for ancillary services [46]. It is also pointed out in [47, 48] that controllable loads like TCAs and PHEVs are ideal candidates for the provision of ancillary services through DR. In this thesis, two key problems, i.e., Aggregation Modeling and Control, are considered for two types of terminal loads, i.e., TCAs and PHEVs. In the following, a general literature review is provided for DR with TCAs and DR with PHEVs, respectively. More detailed literature review will be presented in each technical chapter.

1.2.1 DR with TCAs

Within the DR framework, the potential for the provision of ancillary services via aggregating and controlling TCAs is generally discussed in [47,49–54]. Typical TCAs include residential and commercial HVAC systems, A/Cs, heat pumps, EWHs, and refrigerators. Those appliances could properly adjust their power consumption without affecting end-users' comfort level. The conceptual grid construction of utilizing TCAs for ancillary services is shown in Figure 1.1. In the supply side, the base-

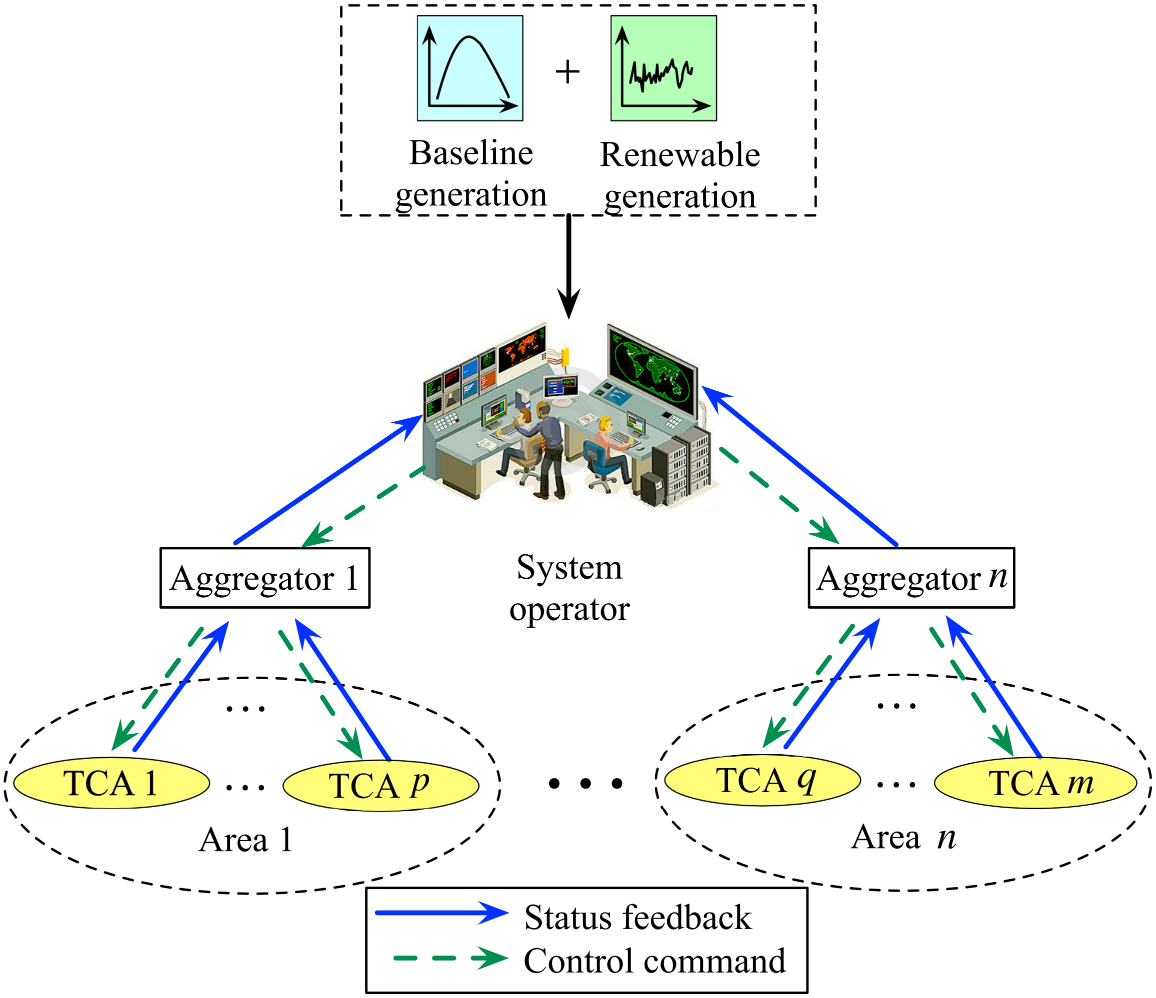

Figure 1.1: The conceptual scheme of a smart grid for controlling TCAs.

line generation is to fulfill the baseline demand of end-users. With the intermittent renewable energy generation or regulation signals added, the supplied power may fluctuate, causing an imbalance between the power supply and demand. In order to suppress the imbalance, instead of building new regulating generators, DR enables the end-users to provide this service from the demand side. In the technical part, load aggregators receive desired power trajectories from the ISO and directly control the participated end-users to adjust their aggregated power consumption. In the market part, aggregators receive incentives from the ISO for providing this service and offer participants incentives to gain the direct control. It is worth mentioning that a single

TCA is not qualified to complete this task for it can only affect the grid in a negligible scale. In contrast, by aggregating and controlling a large population of TCAs, ancillary services from the demand side can be achieved.

Two cruxes in this topic include 1) how to establish the aggregate TCA dynamics for the local aggregator in order to gain a clear view of the terminal loads, and 2) how to design an accurate and high-performance controller for the aggregator to fulfill grid service needs. Those two problems have attracted increasing attention in the literature. Some popular results are summarized below.

In 2004, Lu *et al.* [53] proposed a *state-queueing* model for TCAs to respond to the price signal. All loads are stacked in a priority queue according to their running status. Based on the state-queueing model, Kondoh *et al.* [54] discussed the potential of aggregated EWHs for providing the regulation service. An IF-THEN control algorithm is proposed to fulfill the minute-scale regulation service. Later in 2012, Ning Lu extended the results in [54] and discussed the potential of general HVAC loads' potential for providing load balancing service [50, 55]. In those two literature, a first-order state-space model of HVAC loads was proposed, based on which the state-queueing method in [53] was extended to respond to the grid control signal instead of the price signal. This implies the transformation from price-based DR to regulation-signal-based DR. Since the proposed control design was based on logic conditions, the solution in [50] could not guarantee the optimality. Later in 2013, Zhang *et al.* presented a delay-dependent control strategy based on the state-queueing model to coordinate the aggregated power consumption of A/Cs to provide load balancing service [56]. It was further extended by Lu *et al.* [57] in 2013 by designing a centralized controller to consider general TCAs for providing continuous regulation reserve. A dynamic parameter selection process based on exhaustive simulations of different regulation scenarios was proposed in [58]. This parameter selection could be made as a look-up table for the operators to choose from based on the magnitude of regulation signals. Other work employing the state-queueing model can be found in [59, 60]. Another similar idea to state-queueing is the *direct stacking.* Vrettos *et al.* [61] adopted the idea of stacking the dynamics of all TCAs in the aggregation model. The idea is also employed in [62]. This direct stacking could provide a clear view of the status of all connected end-users and can include a strict constraint on terminal temperature control.

The group led by Duncan Callaway in University of California, Berkeley, conducted research on the aggregation and control of TCAs for ancillary services from 2009. After summarizing the potential of using controllable electric loads for ancillary services [47], in 2009, new modeling and control methods based on coupled Fokker-Planck equations [63] for a population of TCAs to provide regulation and load following services were proposed in [64]. A minimum variance control law was developed to change the setpoints instead of controlling the switches. Later in 2011, Koch *et al.* [65] proposed a new modeling approach to describe the aggregate dynamics based on [64]. The novel part of this model is that, instead of stacking all TCAs' individual dynamics into one model, the authors developed a *population-based* model to describe the dynamics of the TCA population migration. Similar to but not the same as the approaches in [53], all TCAs are partitioned into several state bins according to their temperature information and running status. Hence, individual TCA dynamic evolutions are converted into TCA population migration probabilities. As a result, the centralized computational size is no longer associated with the TCA population size, instead, solely dependent on the number of state bins. However, in the derivation of the system transition model, the authors considered neither the time-varying character nor the probability distribution of the starting temperature. Based on the modeling and control methods in [65], Mathieu *et al.* [66] proposed a

Kalman filtering scheme in order to estimate both the unmeasurable states and joint parameters/states. This work was detailed and expanded in [67]. A moving horizon state estimator (MHSE) was further proposed to estimate the unavailable states [68]. Authors in [69] presented a non-uniform population-based model in which lengths of the state bins are not equal. It is stated in [69] that, the non-uniform fashion may increase the accuracy of the prediction model even with a less number of bins.

Another research group conducting research on this topic is led by Wei Zhang at Ohio State University. Different from the above literature, the individual TCA dynamics in their research is selected as a second-order one, in which building mass temperature is considered together with the indoor air temperature. In [51, 70], the authors validated the advantages of using both indoor air and building mass temperature in the TCA aggregation. In [51], Zhang *et al.* proposed a simple centralized inverse controller calculating for and broadcasting switching probabilities to all TCAs according to the proposed 2-D population flow mechanism. The compressor time delay was considered in the control strategy. One drawback of this strategy lies in the individual switching probability, which may cause a severe mismatch between the nominal control signal and the actually implemented one. Hence, a system model that can inherently describe population migration probabilities and a controller that broadcasts determinant switching actions are urged. The authors also verified the feasibility of implementing the proposed model and control strategy in regulation services, yet with violations in the end-users' comfort requirements. Guo *et al.* [62] extended the above results and proposed a decentralized control scheme to solve the problem of a large scale population. The proposed decentralized control strategy shows an acceptable performance in tracking reference trajectories and reducing the peak power consumption.

1.2.2 DR with PHEVs

Recently, there are intensive discussions on the potential of utilizing the charging process of a large population of PHEVs to mitigate the PHEV integration impact on grid and to provide ancillary services. In [48], the authors generally discussed on achieving controllability of PHEVs for load shifting, supply-demand balancing, and contingency reserves. Hota *et al.* [71] surveyed the cutting-edge approaches to the general issues of integrating PHEVs into the grid. In a smart grid with a large population of PHEVs connected, different components are connected via two networks, namely communication and electricity networks. According to the power flow topologies and directions, authors in [72] summarized the opportunities and challenges of several popular PHEV integration modes, including vehicle-to-home (V2H), vehicle-to-grid (V2G), and vehicle-to-vehicle (V2V). In V2H mode, PHEVs communicate with home appliances and energy management systems (EMSs) so they could supply power from their batteries to compensate for home electricity use; in V2G mode, PHEVs directly communicate with local aggregators or ISOs so as to adjust their charging processes or supply power to the grid; V2V mode is a relatively new concept that local PHEVs could construct their own communication and electricity links, thus energy from the battery in one PHEV can be used to charge another PHEV. In this thesis, only the V2G mode will be discussed for the smart grid infrastructure is already in place for this type of connection. Specifically in V2G mode, according to the directions of physical power flow, the charging schemes can be categorized into V2G-half, i.e., PHEVs can only draw power from the grid, and V2G-full, i.e., battery discharging to grid is allowed. Since most customers and automobile manufacturers have great concerns on the battery life when V2G discharging is allowed [73, 74], in this thesis, only the V2G-half mode is concerned.

Figure 1.2 shows the smart grid structure having PHEVs connected in V2G-half mode for ancillary services. Herein, each charging stall connects with a PHEV through

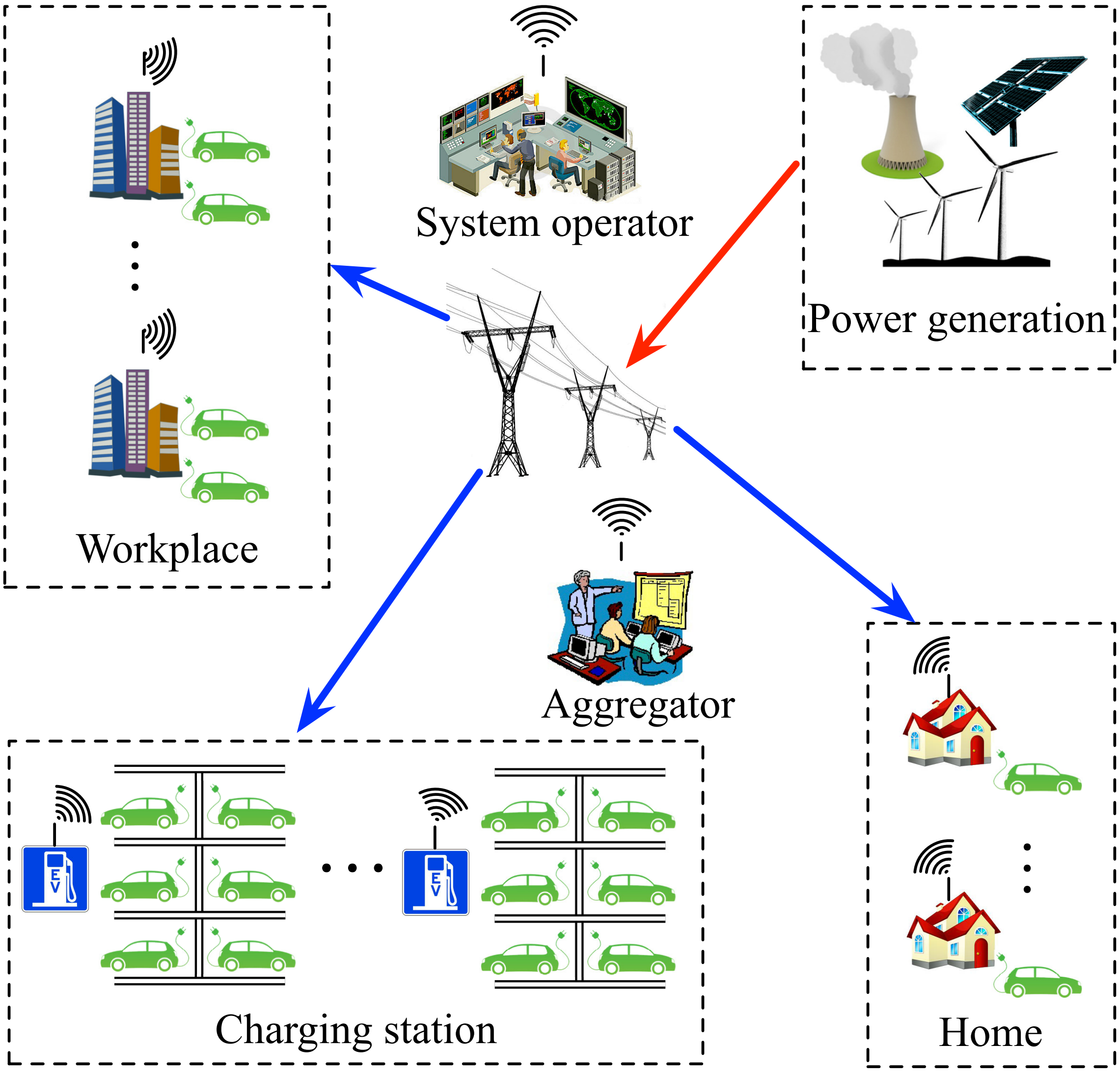

Figure 1.2: The conceptual scheme of a smart grid for controlling PHEVs' charging.

the charging cable to charge the battery, and through wired/wireless links to read the charging status; charging stalls in three representative locations, i.e., workplace, charging station, and home send the charging information of their connected PHEVs to the local aggregator via wired/wireless communication networks; local aggregators receive grid service signals from the system operator, and calculate and dispatch control signals to all charging stalls both via the communication network; once receiving control signals, charging stalls draw power from the physical power grid to charge PHEVs at designated rates.

As in the case of controlling TCAs for DR, development of aggregation models is a crux for the charging control of a large population of PHEVs. However, the study of this topic is still in a primal stage, and little work has been done due to the following difficulties:

- In V2G-half mode, in contrasted with controlling TCAs, battery SOCs cannot have an up-and-down profile. In other words, SOCs are non-decreasing. Thus, once fully charged, a PHEV in no longer available for grid services. This results in a loss of service capability, thus impairing the service quality.
- Individual charging dynamics are subject to large differences due to the diversified battery characteristics.
- In TCA aggregation and control, end-users' requirement is limited to a comfort temperature. However, in PHEV charging control, end-users' requirements are not limited to a specified battery SOC. More realistic and personalized requirements, such as driver's specified charging deadline and specified charging period, make the development of a comprehensive aggregation model and control strategy challenging.

Among the very limited literature, aggregation models in [75, 76] are developed based on the direct stacking approach. Thus the proposed centralized controller may encounter the issue of heavy computational load. Kundu and Hiskens [77] investigated an aggregation model, which is essentially an average battery charging model, based on the steady-state probability distributions of chargers in ON and OFF status. This model is formulated into a linear state-space model, based on which a feedback controller is designed to control the SOC deadband. In [78], the authors developed an aggregated SOC model based on the participation factor of each PHEV. Bashash and Fathy [79] proposed a collective charging scheme for homogeneous PHEVs. This scheme presents the migration dynamics of the PHEV population in different SOC levels. A sliding mode control scheme is developed based on this collective model.

1.3 Research Motivations and Contributions

Though there already exist numerous results on controlling electric loads for DR, many problems in aggregation modeling and control remain open. As mentioned in the preceding literature review, the aggregation model embedded in the local aggregator is the foundation for the service-signal-based DR programs. A well-developed aggregation model is expected to provide the local aggregator accurate information of terminal loads' running status, large capability for control, full consideration of end-users, and minimum requirement on grid infrastructure. Existing approaches only focus on a single target of those aspects, thus this topic deserves further research. This thesis studies aggregation models step-by-step further from the most comprehensive but relatively complex one to the quasi-comprehensive but relatively tractable one. The controller design would be dependent on the selection of aggregation models. However, based on the same model, a controller that requires less information, which reduces the communication network load, and less computational effort is urged.

Chapter 2 deals with the aggregation modeling and control of TCAs for secondary frequency control. In order to gain a global and comprehensive view of individual TCA dynamics, a direct dynamic stacking approach is adopted in developing the aggregation model. A centralized MPC scheme is firstly investigated to control the aggregated power consumption of VFD-equipped TCAs. To further consider a more practical case, where all TCAs are VFD-free, and to reduce the centralized computational load, a DMPC design is presented. An important physical constraint, i.e., TCA lockout effect, is firstly explicitly characterized by time-integrated interdependent logic conditions. In order to facilitate the predictive control scheme, a novel approach for converting those logic conditions into inequality constraints is proposed. This approach can also be employed to deal with similar types of constraints. Finally, illustrative examples are provided to show the effectiveness of the proposed stacking model and two predictive controllers.

Further investigating TCAs for fast DR, Chapter 3 switches to investigate primary frequency control. To save the computational effort of centralized aggregators, a 2-D population-based model is investigated. Through this model, individual second-order TCA dynamic evolutions are converted into TCA population migration probabilities, thus computational load is decoupled from the population size. This model is novel compared to the literature in terms of the inclusion of building mass temperature and a more general formula for computing migration probabilities. A centralized MPC scheme, in which the temperature constraints is realized as a relaxed constraint in the objective function, is studied. In the end of Chapter 3, an illustrative example and comprehensive analyses are provided to verify the feasibility of the proposed approaches.

Chapter 4 also deals with the modeling and control problems of aggregated TCAs. In addition to Chapter 3, it focuses on eliminating the mismatch between nominal control signals and the actually implemented ones. An improved population-based model, which has lockout effect inherently embedded, is proposed. Traditional population-based models are extended by adding additional state bins to represent different lockout depths. To compensate for the additional computational load introduced by the added state bins, a DMPC scheme is investigated. One step further to practical applications, an optimal control scheme is proposed in the case that predictions of regulation signals are not available. A novel concept, i.e., regulation capacity, is introduced into the objective function to preserve the future regulation capacity. Case studies are conducted for both of the DMPC and optimal control schemes.

To fill the gap in the research of controlling PHEVs for DR, aggregation and charging control of PHEVs are investigated in Chapter 5. Traditional aggregation models only utilize battery SOC as the charging indicator and ignore the drivers' charging requirements. In contrast to the literature, a new concept, namely charging requirement index, is proposed in Chapter 5 to comprehensively feature local charging status and charging requirements. A population-based model is investigated based on the proposed index. Population migration probabilities are derived as piece-wisely continuous functions of the control signal. These functions are further curve-fitted by polynomials for the sake of optimization. Monte Carlo simulations are conducted to verify and amend the proposed aggregation model. In the control part, a centralized MPC scheme is investigated to control the charging rates of individual PHEVs. This chapter also presents a case study to verify the efficacy of the proposed approaches for the overnight valley-filling service.

1.4 Organization of the Thesis

A visual organization of this thesis is shown in Figure 1.3. The thesis is organized as follows. Chapter 1 starts with reviewing the fundamentals and state-of-the-art of DR. It also presents the research background, motivations, and objectives of this PhD thesis.

Chapters 2-4 deal with the aggregation and control problems of TCAs. A direct stacking model is proposed in Chapter 2, based on which centralized MPC and DMPC

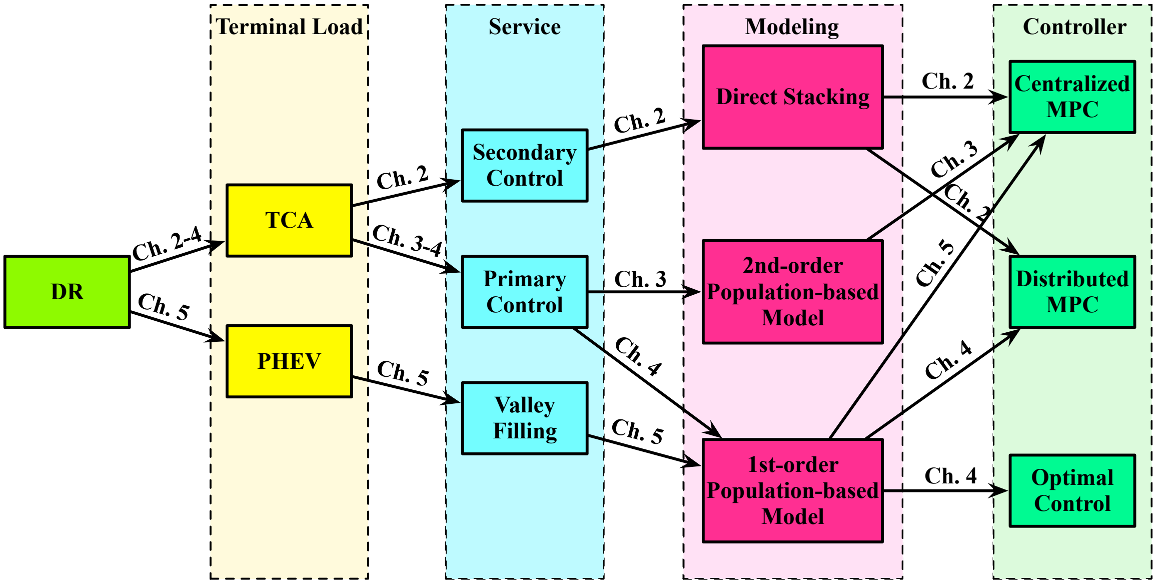

Figure 1.3: Organization of this thesis.

schemes are designed, for the purpose of secondary frequency control. Chapter 3 investigates a 2-D population-based model to reduce the centralized computational load. A centralized MPC scheme is studied for primary frequency control. One step further to the practical scenario, an improved population-based model, which effectively eliminates the control signal mismatch, is proposed in Chapter 4. A DMPC and an optimal control schemes are separately designed based on this model.

Chapter 5 is concerned with the aggregation and charging control of PHEVs. A novel index-induced population-based model is proposed. Monte Carlo simulations are conducted to verify and amend the proposed aggregation model. A centralized MPC scheme is investigated to control the charging rates of individual PHEVs.

Chapter 6 summarizes the work in this thesis, and presents some potential future research directions.

Chapter 2

Direct Aggregation and MPC for TCAs Providing Balancing Service

2.1 Introduction

2.1.1 Background and Literature Review

Renewable energy generation in the world has been expanding quickly over the last decade. For the 12 months period to May 2013, the electricity produced from wind power in the US was 153.6 TWh, which is 3.78% of all generated electrical energy [80]. The newly constructed wind power generation capacity in the US in the fourth quarter of 2012 reached 8380 MW, which brought the cumulative capacity to 60000 MW. Apart from the potential of substantial renewable energy generation, more stress has been put on the regulating generators to balance the power supply and demand. However, in most cases, regulating generators are not working at their preferred working point, which is not efficient [50]. In addition, the fast-changing regulation signal may drive the regulating generator frequently changing its working condition, putting too much stress on the mechanical system and will shorten the lifetime. It has been reviewed in Chapter 1 that DR is the most promising technique to achieve both the high renewable utilization efficiency and a reliable power grid.

TCA is one type of terminal load that can be controlled for modern DR programs. In [47,50], the authors elaborated the potential of the provision of load balancing service via controlling the aggregated power consumption of TCAs. Hao *et al.* [52] proposed a battery model showing that flexible loads such as TCAs are good candidates for ancillary services. They further developed a priority-stack-based control architecture to control TCAs to track the automatic generation control (AGC) signal. As stated in Chapter 1, one of the cruxes of controlling TCAs is on constructing the aggregate dynamics. In [50], all TCAs are distributed into a priority list according end-users' temperature information and running status. A centralized control scheme was developed based on this list, i.e., TCAs with temperature closer to the upper and lower limits have the priority to switch. In [81], the authors adopted a partial differential equation model and proposed a sliding mode controller to control the setpoints of TCAs in order to adapt the aggregated power consumption of A/Cs to intermittent wind power generation. Koch *et al.* [65] proposed a population-based model in which TCAs were allocated in different state bins according to the temperature information and running status. This population-based model provides a promising way to reduce the aggregator's computational load, however, the dynamic evolutions of TCAs cannot be fully captured unless the model is sufficiently accurate. In [82], the authors proposed an aggregation model based on formal abstraction, yet for homogeneous TCAs. Vrettos *et al.* [61] adopted the idea of stacking the dynamics of all TCAs to form an aggregation model. This direct stacking approach could provide a clear view of the status of all connected TCAs and can include a strict constraint on terminal temperature control. In this chapter, the stacking approach is employed to develop the aggregation model.

In the controller design, in order to obtain the optimal control strategy for heterogeneous TCAs, to guarantee end-users' comfort level, and to take numerous technical constraints, e.g., TCA lockout time, into consideration, an MPC scheme [83] will be established. Among all different control schemes, MPC shows its success in many industrial applications for numerous technical constraints can be included in the controller design [61, 84–89]. The essential idea of MPC is the receding horizon control scheme which can be simply described as 1) optimize the control objective function along a certain prediction horizon; 2) obtain an optimal control sequence; 3) only apply the first element in the optimal control sequence as the current control signal; 4) repeat the same procedure for the next time instant. According to communication topologies, there are mainly three types of MPC schemes, i.e., centralized MPC, decentralized MPC, and DMPC. In centralized MPC, all terminal appliances only communicate with a centralized controller which is in charge of computing and dispatching control signals. In decentralized MPC, since there exists no centralized controller nor a communication link among appliances, terminal appliances compute control signals for themselves. In contrast, DMPC makes use of the communication links. In DMPC scheme, by integrating neighbour appliances' running information into its own, each appliance computes its own control signal. In this chapter, in order to take full advantage of the communication network in smart grid, design of a decentralized MPC will not be considered. It is also worth mentioning that, since centralized MPC scheme has a global view of the entire system, it should outperforms the other two types. However, when the problem size increases, the centralized scheme may encounter the computational complexity issue, which urges the need of a DMPC scheme. Centralized and distributed MPC designs are two of the thrusts in this chapter.

The appliance-level control stays in controlling the running status of individual

TCAs. Most control strategies are designed for pure ON/OFF switching control by considering TCAs without varying frequency drives (VFDs). When TCAs are equipped with VFDs, their power consumption can be commanded to vary quickly and continuously, and can be controlled to achieve a better service quality. In recent years, VFDs have been installed in an increasing number of HVAC systems in North America. Most major control companies, e.g., ABB, Honeywell, and Johnson Control, are manufacturing VFDs for HVAC systems. A/Cs are more popular in Asia-Pacific – more than 70% market shares, in which around 30% are equipped with VFDs. Refrigerators with VFDs are getting more and more popular. Major refrigerator manufacturers, e.g., Samsung and LG, are getting larger market shares in the VFD-equipped refrigerators. In the contrast, VFDs are not quite popular in EWHs. All those installed VFDs can be employed for the purpose of achieving DR. Apart from the benefits, VFD-equipped TCAs are still exposed to the risk of losing lubrication, increasing vibration, or being worn out shortly if continuously working at low frequency. In order to avoid frequent switching actions and to reduce the chance of running in extremely low frequency, minimum ON/OFF (lockout) time together with the TCA minimum power level should be considered in the control design. As mentioned, but not studied in [50], the lockout time severely affects the balancing capacity. Furthermore, the lockout time constraints are normally pure logic conditions, which are not ready for use in an optimization problem. Hao *et al.* [52] adopted the priority stack approach to construct a non-violating switching order. This priority stack is quite effective when no prediction is needed, however being difficult to fit in the MPC scheme. In [90], the authors handled the lockout constraints by limiting the number of transitions. Ledva *et al.* [91] proposed a new control architecture which includes an MPC controller and an index generator. They guaranteed the minimum time between two subsequent switch-ON signals by considering the available number of switches without violating the switching constraints. In [92, 93], DMPC designs of multi-μCHPs for balancing power supply and demand are discussed. In those two works, the lockout time is incorporated into the MPC problem by using the method proposed in [94]. However, a "counter" is defined and required to be reset to 0 when an action happens and this reset is not inherently formulated in the system constraints. In addition, the approach discussed in [94] does not consider the cases where conditions and decision variables are interdependent, or the time values are involved. Motivated by the above observations, integrated MPC approaches, being capable of handling the time-integrated interdependent logic constraints, are practically demanded. This thrust is another focus of this chapter.

2.1.2 Research Objectives and Contributions

Motivated by the aforementioned points, objectives and contributions of this chapter can be summarized as follows.

- A direct stacking aggregation model for TCAs is constructed. This model allows the ISO to have a clear view of all terminal TCAs' dynamic evolutions.
- A centralized MPC scheme is built upon the direct stacking model. This scheme is designed for a population of VFD-equipped TCAs. It can also be extended to deal with more general cases, where an arbitrary fraction of TCAs is VFD-equipped.
- A DMPC scheme is developed for a population of VFD-free TCAs. The DMPC scheme could dramatically reduce the computational load compared to the centralized scheme.
- A novel approach for converting logic conditions into inequalities is proposed.

This approach can well handle the time-integrated interdependent logic conditions.

2.1.3 Chapter Organization

This chapter is organized as follows. Section 2.2 focuses on the centralized MPC design, covering individual TCA modeling, centralized MPC scheme development, logic constraints conversion, and case studies. DMPC scheme for controlling VFD-free TCAs is studied in Section 2.3. Section 2.4 summarizes this chapter.

2.2 Centralized MPC Design

2.2.1 Thermal Dynamic Model of a Single TCA Unit

The thermal dynamics of an individual TCA unit is the basis for developing the aggregation model and control scheme. In this chapter, by ignoring the impact of the building mass temperature, we adopt the popular first-order ETP model [95], which is suitable for heating for residential or small commercial buildings, to describe the dynamics of individual loads. In this model, indoor air temperature is affected by both the ambient temperature and the heating flux. Figure 2.1 shows the equivalent electric circuit of the model. The dynamics can be expressed as

$$\dot{T}_i(t) = \frac{1}{C}\left[\frac{1}{R}(T_o(t) - T_i(t)) + Q(t)\right], \tag{2.1}$$

where $T_i(t)$ and $T_o(t)$ are the indoor air temperature and ambient temperature at time t, respectively; C(J/°C) and R(°C/W) are the equivalent heat capacity and equivalent thermal resistance, respectively; and $Q(t)$ is the equivalent heat rate at time t. By considering a discrete time step Δt, the continuous-time ETP model for

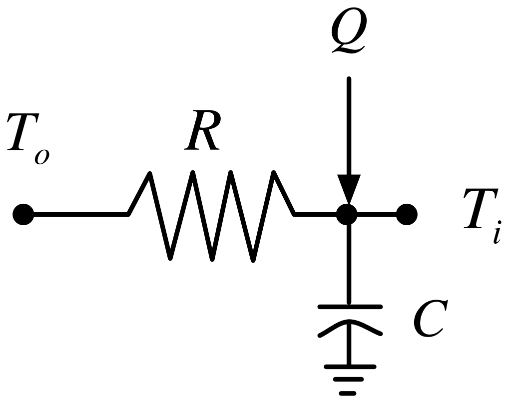

Figure 2.1: First-order ETP model.

the ith TCA can be discretized as [96]

$$x_i(k+1) = A_i x_i(k) + B_i u_i(k) + D_i \omega(k), \tag{2.2}$$

where $x_i(k)$, $u_i(k)$, and $\omega(k)$ denote the indoor air temperature, equivalent heating rate, and ambient temperature in the time interval $[k, k+1]$, respectively. In addition, $A_i = e^{-\Delta t/R_i C_i}$, $B_i = (1 - e^{-\Delta t/R_i C_i})R_i$, and $D_i = 1 - e^{-\Delta t/R_i C_i}$.

2.2.2 Centralized MPC Scheme for Balancing Signal Tracking (without considering lockout effect)

In this section, we shall adopt the stacking approach [61] to obtain an augmented system dynamics for a population of TCAs, and then develop the predictive controllers. Assume m TCAs being connected, the stacked system dynamics can be represented as

$$\hat{x}(k+1) = \hat{A}\hat{x}(k) + \hat{B}\hat{u}(k) + \hat{D}\hat{\omega}(k), \tag{2.3}$$

where $\hat{x}(k) = [x_1(k) \ \cdots \ x_m(k)]^\mathsf{T}$, $\hat{u}(k) = [u_1(k) \ \cdots \ u_m(k)]^\mathsf{T}$, $\hat{\omega}(k) = [\omega_1(k) \ \cdots \ \omega_m(k)]^\mathsf{T}$, and

$$\hat{A} = \begin{bmatrix} A_1 & & \\ & \ddots & \\ & & A_m \end{bmatrix}, \ \hat{B} = \begin{bmatrix} B_1 & & \\ & \ddots & \\ & & B_m \end{bmatrix}, \ \hat{D} = \begin{bmatrix} D_1 & & \\ & \ddots & \\ & & D_m \end{bmatrix}. \tag{2.4}$$

The state prediction vector in an MPC fashion is defined as

$$\hat{\mathbf{x}}(k) = \begin{bmatrix} \hat{x}(k+1|k) \\ \hat{x}(k+2|k) \\ \vdots \\ \hat{x}(k+N|k) \end{bmatrix} \in \mathbb{R}^{mN}, \tag{2.5}$$

where $\hat{x}(k+j|k)$ is the prediction of $\hat{x}(k+j)$ in the time interval $[k+j, k+j+1]$ with the knowledge in the time interval $[k, k+1]$ according to the system model in (2.3), and N is the prediction horizon. The control sequence, including the control signal from time k to time $k+N-1$, is defined as

$$\hat{\mathbf{u}}(k) = \begin{bmatrix} \hat{u}(k|k) \\ \hat{u}(k+1|k) \\ \vdots \\ \hat{u}(k+N-1|k) \end{bmatrix} \in \mathbb{R}^{mN}. \tag{2.6}$$

In this chapter, it is assumed that the ambient temperature can be accurately predicted. Tackling inaccurate forecasted ambient temperature will be addressed in the future work. The known external input vector can be defined as

$$\hat{\boldsymbol{\omega}}(k) = \begin{bmatrix} \hat{\omega}(k|k) \\ \vdots \\ \hat{\omega}(k+N-1|k) \end{bmatrix} \in \mathbb{R}^{mN}. \tag{2.7}$$

Then the system dynamics in (2.3) can be represented in an MPC form as

$$\hat{\mathbf{x}}(k) = \hat{\mathcal{M}}\hat{x}(k|k) + \hat{\mathcal{C}}\hat{\mathbf{u}}(k) + \hat{\mathcal{D}}\hat{\boldsymbol{\omega}}(k), \tag{2.8}$$

where

$$\begin{gathered} \hat{\mathcal{M}} = \begin{bmatrix} \hat{A} \\ \hat{A}^2 \\ \vdots \\ \hat{A}^N \end{bmatrix}, \hat{\mathcal{C}} = \begin{bmatrix} \hat{B} & \mathbf{0} & \cdots & \mathbf{0} \\ \hat{A}\hat{B} & \hat{B} & \cdots & \mathbf{0} \\ \vdots & & \ddots & \vdots \\ \hat{A}^{N-1}\hat{B} & \hat{A}^{N-2}\hat{B} & \cdots & \hat{B} \end{bmatrix}, \\ \hat{\mathcal{D}} = \begin{bmatrix} \hat{D} & \mathbf{0} & \cdots & \mathbf{0} \\ \hat{A}\hat{D} & \hat{D} & \cdots & \mathbf{0} \\ \vdots & & \ddots & \vdots \\ \hat{A}^{N-1}\hat{D} & \hat{A}^{N-2}\hat{D} & \cdots & \hat{D} \end{bmatrix}. \end{gathered} \tag{2.9}$$

It is worth mentioning that the design objectives are 1) to maintain the end-users' indoor air temperature within a comfortable range, and 2) to control the aggregated TCAs' power consumption to track the balancing signal. The aggregated power consumption can be represented as

$$P_{agg}(k) = \mathbf{1}_m^{\mathsf{T}}\hat{\mathbf{u}}(k), \tag{2.10}$$

where $\mathbf{1}_m = [1\ 1\ \cdots\ 1]^{\mathsf{T}} \in \mathbb{R}^m$. Let $\hat{x}_0 = [x_0\ x_0\ \cdots\ x_0]^{\mathsf{T}} \in \mathbb{R}^m$ and $\hat{u}_0(k)$ denote the indoor air temperature setpoint vector and the balancing signal in the time interval

$[k, k+1]$, respectively. Then in order to achieve the above-mentioned two objectives, the objective function can be written as

$$\mathcal{J}(k) = \mathcal{J}_1(k) + \mathcal{J}_2(k), \tag{2.11}$$

where

$$\mathcal{J}_1(k) = \sum_{j=0}^{N-1} \left[(\hat{x}(k+j+1|k) - \hat{x}_0)^\intercal \hat{Q} (\hat{x}(k+j+1|k) - \hat{x}_0) \right],$$
$$\mathcal{J}_2(k) = \sum_{j=0}^{N-1} \left[(P_{agg}(k+j|k) - \hat{u}_0(k+j))^\intercal \hat{R} (P_{agg}(k+j|k) - \hat{u}_0(k+j)) \right].$$

In (2.11), $\mathcal{J}_1(k)$ and $\mathcal{J}_2(k)$ are the indoor air temperature tracking penalty and balancing signal tracking penalty, respectively, in quadratic forms. $\hat{Q} \in \mathbb{R}^{m \times m}$ and $\hat{R} \in \mathbb{R}^1$ are the weights for $\mathcal{J}_1(k)$ and $\mathcal{J}_2(k)$, respectively.

Remark 2.1: $\hat{Q}$ and $\hat{R}$ are chosen to balance the trade-off between the two objectives. Specifically, relatively larger $\hat{Q}$ gives a better terminal comfort level but worse balancing signal tracking. In the case that $\hat{Q}$ is relatively larger, more effort is put on tracking the most comfortable indoor air temperature, which results in a loss of balancing capacity. These two parameters can be adjusted by the ISO or local aggregator to achieve different goals. ■

Remark 2.2: The indoor air temperature setpoints x_0 in $\hat{x}_0$ are set to be uniform for all connected TCAs in this chapter. However, it is possible that different TCAs have different setpoints, which can be readily achieved by changing x_0 for different TCAs accordingly. In this chapter, in order to make the later case study results clear, we use the uniform setpoints. ■

Neglecting the constant term, $\mathcal{J}_1(k)$ can be rewritten as

$$\begin{aligned}\mathcal{J}_1(k) &\approx \sum_{j=0}^{N-1}\left[\hat{x}(k+j+1|k)^{\mathsf{T}}\hat{Q}\hat{x}(k+j+1|k) - 2\hat{x}_0^{\mathsf{T}}\hat{Q}\hat{x}(k+j+1|k)\right] \\ &= \hat{\mathbf{x}}(k)^{\mathsf{T}}\hat{\mathcal{Q}}\hat{\mathbf{x}}(k) - 2\hat{\mathcal{P}}^{\mathsf{T}}\hat{\mathbf{x}}(k),\end{aligned} \tag{2.12}$$

where $\hat{\mathcal{Q}} = \mathrm{diag}\{\hat{Q}\}$ and $\hat{\mathcal{P}} = \begin{bmatrix}\hat{x}_0^{\mathsf{T}}\hat{Q} & \hat{x}_0^{\mathsf{T}}\hat{Q} & \cdots & \hat{x}_0^{\mathsf{T}}\hat{Q}\end{bmatrix}^{\mathsf{T}}$.

Substituting (2.8) into (2.12), we can obtain that

$$\mathcal{J}_1(k) \approx \hat{\mathbf{u}}(k)^{\mathsf{T}}\hat{\mathcal{C}}^{\mathsf{T}}\hat{\mathcal{Q}}\hat{\mathcal{C}}\hat{\mathbf{u}}(k) + 2\left[\left(\hat{\mathcal{M}}\hat{x}(k|k) + \hat{\mathcal{D}}\hat{\boldsymbol{\omega}}(k)\right)^{\mathsf{T}}\hat{\mathcal{Q}}\hat{\mathcal{C}} - \hat{\mathcal{P}}^{\mathsf{T}}\hat{\mathcal{C}}\right]\hat{\mathbf{u}}(k). \tag{2.13}$$

Similarly, we have $\mathcal{J}_2(k)$ rewritten as

$$\begin{aligned}\mathcal{J}_2(k) \approx &\sum_{i=0}^{N-1}\left[\hat{u}(k+i|k)^{\mathsf{T}}\mathbf{1}_m\hat{R}\mathbf{1}_m^{\mathsf{T}}\hat{u}(k+i|k) - 2\hat{u}_0(k+i)\hat{R}\mathbf{1}_m^{\mathsf{T}}\hat{u}(k+i|k)\right] \\ =&\hat{\mathbf{u}}(k)^{\mathsf{T}}\hat{\mathcal{R}}\hat{\mathbf{u}}(k) + 2\hat{q}^{\mathsf{T}}\hat{\mathbf{u}}(k),\end{aligned} \tag{2.14}$$

where

$$\hat{\mathcal{R}} = \begin{bmatrix}\mathbf{1}_m\hat{R}\mathbf{1}_m^{\mathsf{T}} & & & \\ & \mathbf{1}_m\hat{R}\mathbf{1}_m^{\mathsf{T}} & & \\ & & \ddots & \\ & & & \mathbf{1}_m\hat{R}\mathbf{1}_m^{\mathsf{T}}\end{bmatrix} \in \mathbb{R}^{mN\times mN},$$

$$\hat{q} = -\begin{bmatrix}\mathbf{1}_m\hat{R} & & & \\ & \mathbf{1}_m\hat{R} & & \\ & & \ddots & \\ & & & \mathbf{1}_m\hat{R}\end{bmatrix}\begin{bmatrix}\hat{u}_0(k) \\ \hat{u}_0(k+1) \\ \vdots \\ \hat{u}_0(k+N-1)\end{bmatrix}. \tag{2.15}$$

Thus, (2.11) can be equivalently represented as

$$\mathcal{J}(k) \approx \hat{\mathbf{u}}(k)^{\mathsf{T}} \left(\hat{\mathcal{C}}^{\mathsf{T}}\hat{\mathcal{Q}}\hat{\mathcal{C}} + \hat{\mathcal{R}}\right) \hat{\mathbf{u}}(k) + 2\left[\left(\hat{\mathcal{M}}\hat{x}(k|k) + \hat{\mathcal{D}}\hat{\boldsymbol{\omega}}(k)\right)^{\mathsf{T}} \hat{\mathcal{Q}}\hat{\mathcal{C}} - \hat{\mathcal{P}}^{\mathsf{T}}\hat{\mathcal{C}} + \hat{q}^{\mathsf{T}}\right] \hat{\mathbf{u}}(k). \tag{2.16}$$

The users' comfort level is constrained by the indoor air temperature deadband σ. As previously defined, the most comfortable indoor air temperature is x_0 which is the element in $\hat{x}_0$. Then the constraints to guarantee users' comfort can be represented as

$$\underline{x} \leq x_i(k+j|k) \leq \overline{x},\ \forall i = 1, \ldots, m,\ j = 1, \ldots, N, \tag{2.17}$$

where $\underline{x} = x_0 - \sigma$ and $\overline{x} = x_0 + \sigma$.

By substituting (2.8) into (2.17) , we have the state constraints represented as

$$\begin{aligned} \hat{\mathcal{C}}\hat{\mathbf{u}}(k) &\leq \overline{x}\mathbf{1}_{mN} - \hat{\mathcal{M}}\hat{x}(k|k) - \hat{\mathcal{D}}\hat{\boldsymbol{\omega}}(k), \\ -\hat{\mathcal{C}}\hat{\mathbf{u}}(k) &\leq -\underline{x}\mathbf{1}_{mN} + \hat{\mathcal{M}}\hat{x}(k|k) + \hat{\mathcal{D}}\hat{\boldsymbol{\omega}}(k), \end{aligned} \tag{2.18}$$

where $\mathbf{1}_{mN} = [1\ 1\ \cdots\ 1]^{\mathsf{T}} \in \mathbb{R}^{mN}$, and the control signal constraints are represented as

$$\begin{aligned} \hat{\mathbf{u}}(k) &\leq \overline{u}\mathbf{1}_{mN}, \\ -\hat{\mathbf{u}}(k) &\leq -\underline{u}\mathbf{1}_{mN}, \end{aligned} \tag{2.19}$$

where $\overline{u}$ and $\underline{u}$ are the upper and lower limits of the power of each TCA unit, respectively. In (2.19), it is assumed that all TCAs have the same power limits. If heterogeneous power limits are considered, $\overline{u}\mathbf{1}_{mN}$ and $\underline{u}\mathbf{1}_{mN}$ should be replaced by

$$\begin{aligned} \overline{\mathbf{u}} &= \left[\overline{\mathbf{u}}_m^{\mathsf{T}}\ \cdots\ \overline{\mathbf{u}}_m^{\mathsf{T}}\right]^{\mathsf{T}}, \\ \underline{\mathbf{u}} &= \left[\underline{\mathbf{u}}_m^{\mathsf{T}}\ \cdots\ \underline{\mathbf{u}}_m^{\mathsf{T}}\right]^{\mathsf{T}}, \end{aligned} \tag{2.20}$$

where

$$\begin{aligned} \overline{\mathbf{u}}_m &= [\overline{u}_1 \ \overline{u}_2 \ \cdots \ \overline{u}_m]^{\mathsf{T}}, \\ \underline{\mathbf{u}}_m &= [\underline{u}_1 \ \underline{u}_2 \ \cdots \ \underline{u}_m]^{\mathsf{T}}. \end{aligned} \tag{2.21}$$

Herein, $\overline{u}_i$ and $\underline{u}_i$ are the upper and lower limits of the ith TCA, respectively. In the rest of this chapter, without losing generality, we assume that all TCAs have the same power limits.

2.2.3 Centralized MPC Scheme Considering Lockout Effect

In Section 2.2.2, it is assumed that the power of a TCA unit can vary in the range of $[\underline{u}, \overline{u}]$. In real applications, in order to protect the appliance from continuously working at low frequencies, the minimum power consumption $\underline{u} > 0$ is set as a switching-OFF threshold. This threshold is ubiquitous in VFD-equipped devices. Considering this, the power value can be chosen from a discontinuous set $\{0\} \cup [\underline{u}, \overline{u}]$, which implies

$$u_i(k+j|k) \in \{0\} \cup [\underline{u}, \overline{u}], \forall j = 0, 1, \ldots, N-1. \tag{2.22}$$

This discontinuous set constraint indicates that VFD-equipped TCAs can be turned OFF in some certain circumstances. Let $r_i(k+j|k)$ denote the predicted ON/OFF status of the ith TCA in the time interval $[k+j, k+j+1]$ with the knowledge in the time interval $[k, k+1]$, Eqn. (2.22) can be represented as

$$\begin{aligned} & r_i(k+j|k)\underline{u} \leq u_i(k+j|k) \leq r_i(k+j|k)\overline{u}, \\ & \forall i = 1, \ldots, m, \ j = 0, \ldots, N-1, \end{aligned} \tag{2.23}$$

where $r_i(k+j|k) = 1$ if the TCA is ON and $r_i(k+j|k) = 0$ if it is OFF. Let T_{on} and T_{off} denote the minimum ON and OFF time, respectively, then a TCA unit must stay in the ON status for at least T_{on} from the time it is switched ON; and it must stay in

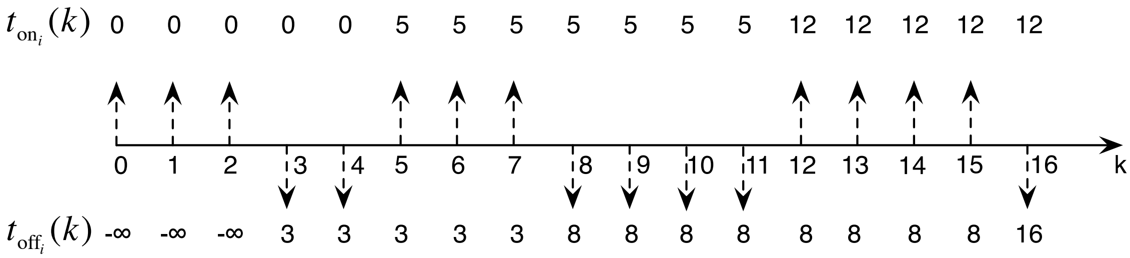

Figure 2.2: Illustration of $t_{\text{on}_i}(k)$ and $t_{\text{off}_i}(k)$.

the OFF status for at least T_{off} from the time it is switch OFF. To justify if the TCA unit can be switched ON/OFF at a certain time instant, additional variables should be introduced.

For the ith TCA in the time interval $[k, k+1]$, denote the nearest switching-ON time to be $t_{\text{on}_i}(k)$ and the nearest switching-OFF time to be $t_{\text{off}_i}(k)$. More precisely, $t_{\text{on}_i}(k)$ indicates the nearest time instant that the TCA was switched ON and being kept ON; $t_{\text{off}_i}(k)$ indicates the nearest time instant that the TCA was switched OFF and being kept OFF. These two variables can be illustrated in Figure 2.2. The up (down) dashed arrow denotes that the ith TCA unit is in ON (OFF) status. In this illustration, T_{on} and T_{off} are set to be 3 and 2, respectively. In the very beginning of this process, we can regard the nearest switching-OFF time as $-\infty$. The whole updating process for $t_{\text{on}_i}(k)$ and $t_{\text{off}_i}(k)$ can be illustrated as follows.

- At $k = 0$, this unit is switched ON, thus $t_{\text{on}_i}(0) = 0$. The nearest switching-OFF time does not change, i.e., $t_{\text{off}_i}(0) = -\infty$. The value of $t_{\text{on}_i}(k)$ will not change until the next switching-ON action.

- At $k = 3$, since the unit has already run for 3 time intervals which equal to T_{on}, it can be switched OFF. At this time, the controller decides to switch this TCA OFF. Thus, $t_{\text{off}_i}(3)$ is updated to 3 as the nearest switching-OFF time. Since no switching-ON action performed, $t_{\text{on}_i}(3)$ stays unchanged. The values of $t_{\text{off}_i}(k)$ will not change until the next switching-OFF action. Please note that the unit can also keep the ON status at $k = 3$. In this example, it is switched OFF.

- At $k = 5$, since the unit has already been OFF for 2 time intervals which equal to T_{off}, it can be switched ON. At this time, the controller decides to switch this TCA ON. Thus, $t_{\text{on}_i}(5)$ is updated to 5 as the nearest switching-ON time. Since no switching-OFF action performed, $t_{\text{off}_i}(5)$ stays unchanged. The values of $t_{\text{on}_i}(k)$ will not change until the next switching-ON action. Please note that the unit can also keep the OFF status at $k = 5$. In this example, it is switched ON.

- At $k = 8$, since the unit has already run for 3 time intervals which equal to T_{on}, it can be switched OFF. At this time, the controller decides to switch this TCA OFF. Thus, $t_{\text{off}_i}(8)$ is updated to 8 as the nearest switching-OFF time. Since no switching-ON action performed, $t_{\text{on}_i}(8)$ stays unchanged. The values of $t_{\text{off}_i}(k)$ will not change until the next switching-ON action. Please note that the unit keeps the OFF status though it can be switched-ON at $k = 11$.

- $\cdots$

As a result, without considering the prediction, the power consumption constraints of the ith TCA at time instant k can be represented as

$$r_i(k)\underline{u} \leq u_i(k) \leq r_i(k)\overline{u}, \tag{2.24}$$

$$r_i(k) = \begin{cases} 0, & k+1-T_{\text{off}} \leq t_{\text{off}_i}(k-1), \\ 1, & k+1-T_{\text{on}} \leq t_{\text{on}_i}(k-1), \\ \{0,1\}, & \text{else}, \end{cases} \tag{2.25}$$

$$t_{\text{on}_i}(k) = \begin{cases} k, & \Delta_i(k) = 1, \\ t_{\text{on}_i}(k-1), & \Delta_i(k) \in \{-1, 0\}, \end{cases} \tag{2.26}$$

$$t_{\text{off}_i}(k) = \begin{cases} k, & \Delta_i(k) = -1, \\ t_{\text{off}_i}(k-1), & \Delta_i(k) \in \{0, 1\}, \end{cases} \tag{2.27}$$

$$\forall i = 1, 2, \ldots, m,$$

where $\Delta_i(k) = r_i(k) - r_i(k-1)$. Consequently, constraints (2.24)–(2.27) together with (2.16) formulate the centralized MPC problem with lockout effect explicitly described.

2.2.4 Interdependent Logic Conditions to Inequality Constraints

It can be noticed from (2.24)–(2.27) that, decision variables $r_i(k)$, $t_{\text{on}_i}(k)$, $t_{\text{off}_i}(k)$, and their conditions are interdependent. For example, by dropping the time, the condition for r_i to choose values depends on the values of t_{on_i} and t_{off_i}; the values of t_{on_i} and t_{off_i} depend on Δ_i which is calculated by r_i. In addition, the time value k is involved in these conditions. As a result, the approach in [94] cannot be soundly employed to convert (2.24)–(2.27) into inequalities. In this section, we borrow the idea of introducing additional binary variables as in [94] to assist the conversion. Each binary variable will be endowed with a specific physical meaning.

From the definitions of $t_{\text{on}_i}(k)$ and $t_{\text{off}_i}(k)$, and the working flow of them, for the

ith TCA, at time instant $k+j$, the predicted nearest switching-ON time $t_{\mathrm{on}_i}(k+j|k)$ can only take the value from $\{t_{\mathrm{on}_i}(k+j-1|k), k+j\}$, which indicates

$$t_{\mathrm{on}_i}(k+j|k) = \psi_{i1}(j)t_{\mathrm{on}_i}(k+j-1|k) + \psi_{i0}(j)(k+j), \tag{2.28}$$

where $\psi_{i1}(j) = 1 - \psi_{i0}(j) \in \{0, 1\}$ denotes the nearest switching-ON time changing index. In the same way, we have

$$t_{\mathrm{off}_i}(k+j|k) = \phi_{i1}(j)t_{\mathrm{off}_i}(k+j-1|k) + \phi_{i0}(j)(k+j), \tag{2.29}$$

with $\phi_{i1}(j) = 1 - \phi_{i0}(j) \in \{0, 1\}$ denoting the nearest switching-OFF time changing index. Thus, it can be readily obtained that

$$\begin{aligned} t_{\mathrm{on}_i}(k|k) &= \psi_{i1}(0)t_{\mathrm{on}_i}(k-1) + \psi_{i0}(0)k, \\ t_{\mathrm{off}_i}(k|k) &= \phi_{i1}(0)t_{\mathrm{off}_i}(k-1) + \phi_{i0}(0)k. \end{aligned} \tag{2.30}$$

Based on (2.30) and by recursion, we have

$$\begin{aligned} & t_{\mathrm{on}_i}(k+j|k) \\ =& \psi_{i1}(j)\dots\psi_{i1}(0)t_{\mathrm{on}_i}(k-1) \\ & + \psi_{i1}(j)\dots\psi_{i1}(1)\psi_{i0}(0)k \\ & + \psi_{i1}(j)\dots\psi_{i1}(2)\psi_{i0}(1)(k+1) \\ & \vdots \\ & + \psi_{i1}(j)\psi_{i0}(j-1)(k+j-1) \\ & + \psi_{i0}(j)(k+j) \\ =& \left(\prod_{\imath=0}^{j}\psi_{i1}(\imath)\right)t_{\mathrm{on}_i}(k-1) + \sum_{\jmath=0}^{j}\left(\prod_{\imath=\jmath}^{j}\psi_{i1}(\imath)\right)(k+\jmath), \end{aligned} \tag{2.31}$$

and

$$\begin{aligned}
& t_{\mathrm{off}_i}(k+j|k) \\
=& \phi_{i1}(j)\dots\phi_{i1}(0)t_{\mathrm{off}_i}(k-1) \\
& + \phi_{i1}(j)\dots\phi_{i1}(1)\phi_{i0}(0)k \\
& + \phi_{i1}(j)\dots\phi_{i1}(2)\phi_{i0}(1)(k+1) \\
& \vdots \\
& + \phi_{i1}(j)\phi_{i0}(j-1)(k+j-1) \\
& + \phi_{i0}(j)(k+j). \\
=& \left(\prod_{\imath=0}^{j}\phi_{i1}(\imath)\right)t_{\mathrm{off}_i}(k-1) + \sum_{\jmath=0}^{j}\left(\prod_{\imath=\jmath}^{j}\phi_{i1}(\imath)\right)(k+\jmath).
\end{aligned} \tag{2.32}$$

Define matrices $\mathbf{\Psi}_i(k) \in \mathbb{R}^{N\times N+1}$ and $\mathbf{\Phi}_i(k) \in \mathbb{R}^{N\times N+1}$ as

$$\mathbf{\Psi}_i(k) = \begin{bmatrix}
\psi_{i1}(0) & \psi_{i0}(0) & & & & \\
\psi_{i1}(1)\psi_{i1}(0) & \psi_{i1}(1)\psi_{i0}(0) & \psi_{i0}(1) & & & \\
\psi_{i1}(2)\psi_{i1}(1)\psi_{i1}(0) & \psi_{i1}(2)\psi_{i1}(1)\psi_{i0}(0) & \psi_{i1}(2)\psi_{i0}(1) & \psi_{i0}(2) & & \\
\vdots & \vdots & \vdots & \vdots & \ddots & \\
\psi_{i1}(N-1)\cdots\psi_{i1}(0) & \psi_{i1}(N-1)\cdots\psi_{i0}(0) & \cdots & \cdots & \cdots & \psi_{i0}(N-1)
\end{bmatrix}, \tag{2.33}$$

$$\mathbf{\Phi}_i(k) = \begin{bmatrix}
\phi_{i1}(0) & \phi_{i0}(0) & & & & \\
\phi_{i1}(1)\phi_{i1}(0) & \phi_{i1}(1)\phi_{i0}(0) & \phi_{i0}(1) & & & \\
\phi_{i1}(2)\phi_{i1}(1)\phi_{i1}(0) & \phi_{i1}(2)\phi_{i1}(1)\phi_{i0}(0) & \phi_{i1}(2)\phi_{i0}(1) & \phi_{i0}(2) & & \\
\vdots & \vdots & \vdots & \vdots & \ddots & \\
\phi_{i1}(N-1)\cdots\phi_{i1}(0) & \phi_{i1}(N-1)\cdots\phi_{i0}(0) & \cdots & \cdots & \cdots & \phi_{i0}(N-1)
\end{bmatrix}, \tag{2.34}$$

and vectors $\Psi_i(k)$ and $\Phi_i(k)$ as

$$\Psi_i(k) = \begin{bmatrix} t_{\text{on}_i}(k-1) \\ k \\ k+1 \\ \vdots \\ k+N-1 \end{bmatrix} \in \mathbb{R}^{N+1}, \tag{2.35}$$

$$\Phi_i(k) = \begin{bmatrix} t_{\text{off}_i}(k-1) \\ k \\ k+1 \\ \vdots \\ k+N-1 \end{bmatrix} \in \mathbb{R}^{N+1}. \tag{2.36}$$

With the above defined matrices and vectors, it can be verified that $t_{\text{on}_i}(k+j|k)$ and $t_{\text{off}_i}(k+j|k)$ can be found to be the jth elements of $\mathbf{\Psi}_i(k) \times \Psi_i(k)$ and $\mathbf{\Phi}_i(k) \times \Phi_i(k)$, respectively.

By doing so, $t_{\text{on}_i}(k+j|k)$ ($t_{\text{off}_i}(k+j|k)$) does not rely on $t_{\text{on}_i}(k+j-1|k)$ ($t_{\text{off}_i}(k+j-1|k)$) but only depends on $\psi_i(\ell)$ ($\phi_i(\ell)$) and the known $t_{\text{on}_i}(k-1)$ ($t_{\text{off}_i}(k-1)$), where $\ell = 0, 1, \ldots, j$. This is equivalent to decoupling the dependent decision variables. Consequently, $t_{\text{on}_i}(k+j|k)$ and $t_{\text{off}_i}(k+j|k)$ in the optimizer can be replaced by $\psi_{i1}(j)$ and $\phi_{i1}(j)$, resulting in a new optimizer as

$$\hat{\mathbf{X}}(k) = \left[\hat{\mathbf{u}}(k)^{\mathsf{T}}\ \hat{\mathbf{r}}(k)^{\mathsf{T}}\ \hat{\boldsymbol{\psi}}(k)^{\mathsf{T}}\ \hat{\boldsymbol{\phi}}(k)^{\mathsf{T}}\right]^{\mathsf{T}}, \tag{2.33}$$

where

$$\hat{\mathbf{r}}(k) = \begin{bmatrix} \hat{r}(k|k) \\ \hat{r}(k+1|k) \\ \vdots \\ \hat{r}(k+N-1|k) \end{bmatrix}, \hat{r}(k+j|k) = \begin{bmatrix} r_1(k+j|k) \\ r_2(k+j|k) \\ \vdots \\ r_m(k+j|k) \end{bmatrix}, \tag{2.34}$$

$$\hat{\boldsymbol{\psi}}(k) = \begin{bmatrix} \hat{\psi}(k|k) \\ \hat{\psi}(k+1|k) \\ \vdots \\ \hat{\psi}(k+N-1|k) \end{bmatrix}, \hat{\psi}(k+j|k) = \begin{bmatrix} \psi_{11}(j) \\ \psi_{21}(j) \\ \vdots \\ \psi_{m1}(j) \end{bmatrix}, \tag{2.35}$$

$$\hat{\boldsymbol{\phi}}(k) = \begin{bmatrix} \hat{\phi}(k|k) \\ \hat{\phi}(k+1|k) \\ \vdots \\ \hat{\phi}(k+N-1|k) \end{bmatrix}, \hat{\phi}(k+j|k) = \begin{bmatrix} \phi_{11}(j) \\ \phi_{21}(j) \\ \vdots \\ \phi_{m1}(j) \end{bmatrix}, \tag{2.36}$$

and $\hat{\mathbf{u}}(k)$ is defined in (2.6).

To realize the minimum OFF time constraint, the nearest switching-ON time value should be at least T_{off} later than the nearest switching-OFF time value, which implies

$$t_{\text{on}_i}(k+j|k) - t_{\text{off}_i}(k+j|k) \geq T_{\text{off}}, \text{ if } r_i(k+j|k) = 1. \tag{2.37}$$

Similarly, we have

$$t_{\text{off}_i}(k+j|k) - t_{\text{on}_i}(k+j|k) \geq T_{\text{on}}, \text{ if } r_i(k+j|k) = 0, \tag{2.38}$$

which implies that the nearest switching-OFF time should be at least T_{off} later than the nearest switching-ON time.

To eliminate IF-THEN conditions, we combine (2.37) and (2.38) as

$$\begin{aligned} &(1-2r_i(k+j|k))(t_{\text{on}_i}(k+j|k)-t_{\text{off}_i}(k+j|k)) \\ \leq &(1-r_i(k+j|k))T_{\text{on}}-r_i(k+j|k)T_{\text{off}}, \end{aligned} \tag{2.39}$$

where $t_{\text{on}_i}(k+j|k)$ and $t_{\text{off}_i}(k+j|k)$ can be represented by (2.31) and (2.32), respectively.

In the next step, we will study the relationship among $\psi_{i1}(j)$, $\phi_{i1}(j)$, $r_i(k+j|k)$, and $r_i(k+j-1|k)$. It is worth mentioning that, the physical meanings of $\psi_{i1}(j)$ and $\phi_{i1}(j)$ are the switching actions of $t_{\text{on}_i}(k+j|k)$ and $t_{\text{off}_i}(k+j|k)$, respectively. If $\psi_{i1}(j)=1$ ($\phi_{i1}(j)=1$), $t_{\text{on}_i}(k+j|k)$ ($t_{\text{off}_i}(k+j|k)$) keeps the value of $t_{\text{on}_i}(k+j-1|k)$ ($t_{\text{off}_i}(k+j-1|k)$); otherwise, the value changes to $k+j$. Based on this, we can deduce a truth table as shown in TABLE 2.1 and the conclusions

$$\begin{aligned} &\psi_{i1}(j)+r_i(k+j-1|k)-r_i(k+j|k)<0, \text{ if } \psi_{i1}(j)=0, \\ &\psi_{i1}(j)+r_i(k+j-1|k)-r_i(k+j|k)>0, \text{ if } \psi_{i1}(j)=1, \end{aligned} \tag{2.40}$$

and

$$\begin{aligned} &\phi_{i1}(j)-r_i(k+j-1|k)-r_i(k+j|k)<0, \text{ if } \phi_{i1}(j)=0, \\ &\phi_{i1}(j)-r_i(k+j-1|k)-r_i(k+j|k)>0, \text{ if } \phi_{i1}(j)=1. \end{aligned} \tag{2.41}$$

Table 2.1: Truth table of $r_i(k+j|k)$, $r_i(k+j-1|k)$, $\psi_{i1}(j)$, and $\phi_{i1}(j)$.

$r_i(k+j-1\|k)$	$r_i(k+j\|k)$	$\psi_{i1}(j)$	$\phi_{i1}(j)$
1	1	1	1
1	0	1	0
0	1	0	1
0	0	1	1

Define an infinitesimal ϵ, (2.40) and (2.41) can be represented without IF-THEN conditions as

$$\begin{aligned} &\psi_{i0}(j)[\psi_{i1}(j) + r_i(k+j-1|k) - r_i(k+j|k) + \epsilon] \\ &-\psi_{i1}(j)[\psi_{i1}(j) + r_i(k+j-1|k) - r_i(k+j|k) - \epsilon] \leq 0, \end{aligned} \tag{2.42}$$

and

$$\begin{aligned} &\phi_{i0}(j)[\phi_{i1}(j) - r_i(k+j-1|k) + r_i(k+j|k) + \epsilon] \\ &-\phi_{i1}(j)[\phi_{i1}(j) - r_i(k+j-1|k) + r_i(k+j|k) - \epsilon] \leq 0. \end{aligned} \tag{2.43}$$

By integrating the above results, the objective function for the centralized MPC problem in (2.16) can be rewritten as

$$\begin{aligned} \mathcal{J}(k) \approx &\hat{\mathbf{X}}(k)^{\mathsf{T}} \hat{\mathbf{P}}_{\mathbf{u}}^{\mathsf{T}} \left(\hat{\mathcal{C}}^{\mathsf{T}} \hat{\mathcal{Q}} \hat{\mathcal{C}} + \hat{\mathcal{R}} \right) \hat{\mathbf{P}}_{\mathbf{u}} \hat{\mathbf{X}}(k) \\ &+ 2 \left[\left(\hat{\mathcal{M}} \hat{x}(k|k) + \hat{\mathcal{D}} \hat{\boldsymbol{\omega}}(k) \right)^{\mathsf{T}} \hat{\mathcal{Q}} \hat{\mathcal{C}} - \hat{\mathcal{P}}^{\mathsf{T}} \hat{\mathcal{C}} + \hat{q}^{\mathsf{T}} \right] \hat{\mathbf{P}}_{\mathbf{u}} \hat{\mathbf{X}}(k), \end{aligned} \tag{2.44}$$

where $\hat{\mathbf{P}}_{\mathbf{u}} = \begin{bmatrix} \mathbf{I}_{mN} & \mathbf{0}_{mN} & \mathbf{0}_{mN} & \mathbf{0}_{mN} \end{bmatrix}$.

The linear inequality constraints for end-users' comfort can be represented as

$$\begin{aligned} \hat{\mathcal{C}} \hat{\mathbf{P}}_{\mathbf{u}} \hat{\mathbf{X}}(k) &\leq \overline{x} \mathbf{1}_{mN} - \hat{\mathcal{M}} \hat{x}(k|k) - \hat{\mathcal{D}} \hat{\boldsymbol{\omega}}(k), \\ -\hat{\mathcal{C}} \hat{\mathbf{P}}_{\mathbf{u}} \hat{\mathbf{X}}(k) &\leq -\underline{x} \mathbf{1}_{mN} + \hat{\mathcal{M}} \hat{x}(k|k) + \hat{\mathcal{D}} \hat{\boldsymbol{\omega}}(k), \end{aligned} \tag{2.45}$$

and the linear inequality constraints for the power consumption of TCAs can be represented as

$$\begin{aligned} \hat{\mathbf{P}}_{\mathbf{u}} \hat{\mathbf{X}}(k) &\leq \overline{u} \hat{\mathbf{P}}_{\mathbf{r}} \hat{\mathbf{X}}(k), \\ -\hat{\mathbf{P}}_{\mathbf{u}} \hat{\mathbf{X}}(k) &\leq -\underline{u} \hat{\mathbf{P}}_{\mathbf{r}} \hat{\mathbf{X}}(k), \end{aligned} \tag{2.46}$$

where $\hat{\mathbf{P}}_{\mathbf{r}} = \begin{bmatrix} \mathbf{0}_{mN} & \mathbf{I}_{mN} & \mathbf{0}_{mN} & \mathbf{0}_{mN} \end{bmatrix}$.

The nonlinear inequality constraints, guaranteeing the lockout effect, are represented by (2.39), (2.42), and (2.43). In addition, we have

$$\begin{aligned} u_i(k+j|k) &\in \mathbb{R}, \\ r_i(k+j|k) &\in \{0,1\}, \\ \psi_{i1}(j) &\in \{0,1\}, \\ \phi_{i1}(j) &\in \{0,1\}, \end{aligned} \tag{2.47}$$

$\forall i = 1, 2, \ldots, m,\ j = 0, 1, \ldots, N-1.$

In summary, the optimal control sequence for all TCAs from time instant k to time instant $k+N-1$ can be obtained by solving

$$\begin{aligned} &\min_{\hat{\mathbf{X}}(k)} \ \mathcal{J}(k), \\ &\ \text{s.t. } (2.39), (2.42), (2.43), (2.45) - (2.47). \end{aligned} \tag{2.48}$$

The formulated problem is a mixed-integer nonlinear programming (MINLP) problem, which shall be solved by the Branch-and-Bound algorithm.

Remark 2.3: In this chapter, instead of suppressing the effect caused by plant disturbances, a centralized MPC scheme is proposed to deal with the TCA lockout effect on the control performance. It aims to avoid unnecessary switchings of terminal TCAs at the current time instant, thus preserving the tracking capability along a fixed future horizon. Without this predictive control scheme, many TCAs would be locked due to unnecessary switchings, which severely impairs the future trajectory tracking. For example, at time k, the controller makes a switching decision without any prediction of the future lockout information. This decision will probably switch a large number of TCAs and steer them into the locked status. Then at time $k+1$, if the desired trajectory has a severe change, those locked TCAs cannot be switched back to provide the desired power and more TCAs would be switched and locked for the purpose of the current trajectory tracking. More severely, without any prediction of the future temperature evolutions, these newly locked TCAs may violate the temperature constraints during the lockout period. Thus, even though there is no disturbance/noise included in the system plant (2.3), it is still necessary to adopt an MPC scheme. ■

2.2.5 Case Study

In this section, the feasibility and balancing performance of the proposed centralized MPC will be investigated through the case study. Several parametric studies will also be conducted to demonstrate how the service quality is affected by different temperature deadband widths, lockout time lengths, and ambient temperature profiles.

2.2.5.1 Parameter Selection

The average equivalent heat capacity C and average equivalent thermal resistance R are selected to be 3599.3 J/°C and 0.0047 °C/W, respectively [50]; the time step is $\Delta t = 1$ min; the deadbands for the indoor air temperature are set to be ±2°C and ±0.5°C for parametric studies; the power limits of each TCA in ON status are 6 kW and 700 W, respectively; the minimum ON/OFF time are both selected to be 2 minutes or 5 minutes. R, C, and rated power are randomized to achieve heterogeneity. The number of TCAs selected to test the proposed approach is 1000. The prediction horizon is set to be $N = 4$ min and $N = 5$ min. Weighting matrices $\hat{Q}$ and $\hat{R}$ are chosen to be $10^5\mathbf{I}_m$ and $\mathbf{I}_1$. It is worth mentioning that, there exists an additional constraint on the prediction horizon, which can be represented as

$$N \geq \max\{T_{\text{on}}, T_{\text{off}}\}. \tag{2.49}$$

This additional constraint is set to guarantee all possible switching actions are captured within the prediction horizon. The ambient temperature is taken from the meteorological station located in Victoria International Airport, BC, Canada. Four typical realistic temperature profiles are shown in Figure 2.3.

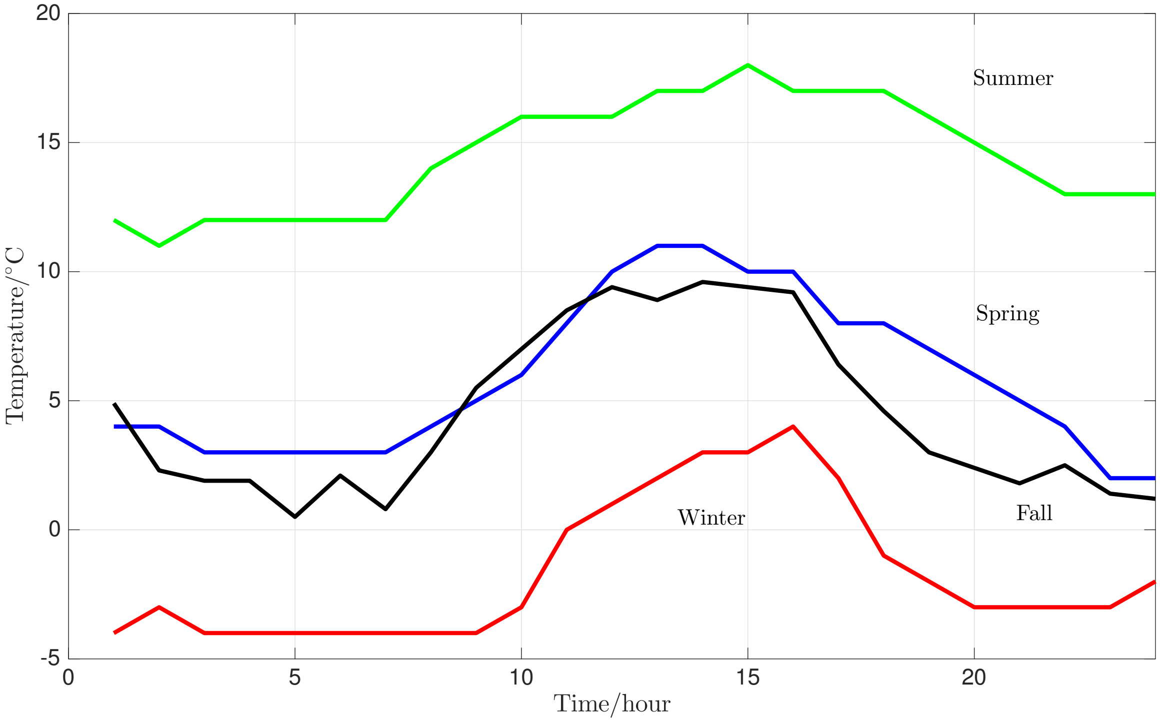

Figure 2.3: Ambient temperature profiles with different averages.

2.2.5.2 Balancing Signal Construction

The balancing signal or desired power trajectory is dependent on the baseline power consumption P_B of all connected TCAs. In the signal construction procedure, each TCA needs to provide its own baseline power consumption to the aggregator. The aggregator then provides the aggregated information to the ISO where the balancing signal is generated. Baseline power consumption of each TCA for the next day is estimated by letting it run in a setpoint tracking mode using the day-ahead ambient temperature forecast. This means that the baseline power consumption is only used for keeping the indoor air temperature within the preset deadband. Since the system model is in minute scale, the baseline power consumption is averaged to the hour scale to follow the day-ahead.

Normally, the balancing signal consists of two parts, i.e., the area control error (ACE) signal P_{ACE} and load following signal P_{FL} [50]. The load following signal is the low-frequency one, which is used for compensating for the difference between the adjusted day-ahead schedule and hour-ahead schedule; ACE signal varies relatively fast to compensate for the difference between the hour-ahead schedule and load following signal, and the actual generation. In real applications, both of the two signals are used as the balancing signal. Those two types of balancing signals are constructed as

$$\begin{aligned} P_c^{FL} &= P_B + P_{FL}, \\ P_c^{ACE} &= P_B + P_{ACE}. \end{aligned} \tag{2.50}$$

Figure 2.4 shows an example of P_B, P_c^{FL} and P_c^{ACE} with 1000 TCAs using the winter weather profile, where realistic data is normalized to ±2.5 MW. This example will be used in the latter case study.

2.2.5.3 Response to Load Following Signal

In this section, we shall test how 1000 TCAs respond to the load following control signal under the circumstances of different deadband widths, lockout time lengths, and weather profiles. With the winter ambient temperature profile as shown in Figure 2.3, three sets of test results, i.e., (±2°C, $T_{\text{on}} = 2$ min, $T_{\text{off}} = 2$ min), (±2°C, $T_{\text{on}} = 5$ min, $T_{\text{off}} = 5$ min), and (±0.5°C, $T_{\text{on}} = 2$ min, $T_{\text{off}} = 2$ min) are shown in Figure 2.5 and Figure 2.6. The corresponding control signals can be seen in Figure 2.7. It is worth mentioning that, no matter in which parameter setup, the optimization problem is

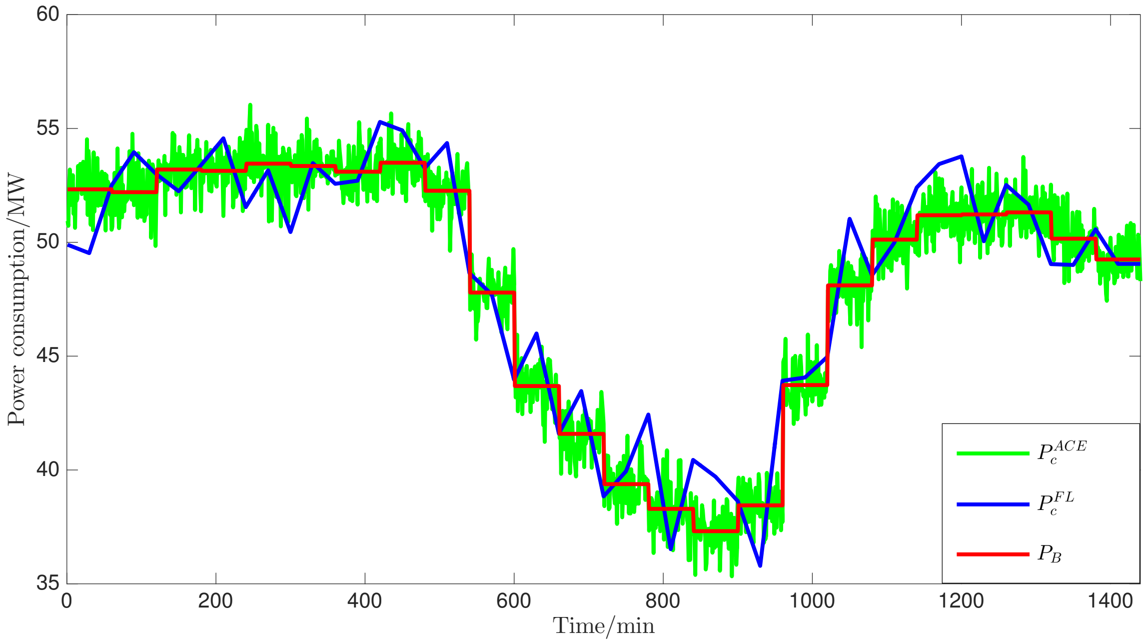

Figure 2.4: Construction of balancing signals (1000 TCAs, winter weather profile).

always feasible during the control process. In other words, the requirements on TCA minimum ON/OFF time can be guaranteed. From the test results we can observe that:

- The indoor air temperature of all connected users varies within the preset comfort range. It is obvious that the temperature cannot be perfectly stabilized at the setpoint, however, staying within the acceptable range meets the contract with the customers.

- By setting ±2°C deadband, $T_{\text{on}} = 2$ min, and $T_{\text{off}} = 2$ min, the aggregated power consumption P_{agg} can track the load following control signal P_c^{FL} very well. To evaluate the tracking performance, we adopt the normed relative error

$$\epsilon = \|P_{agg} - P_c^{FL}\| / \|P_c^{FL}\|. \tag{2.51}$$

  Over a one-day service, the tracking error $\epsilon = 0.026\%$.

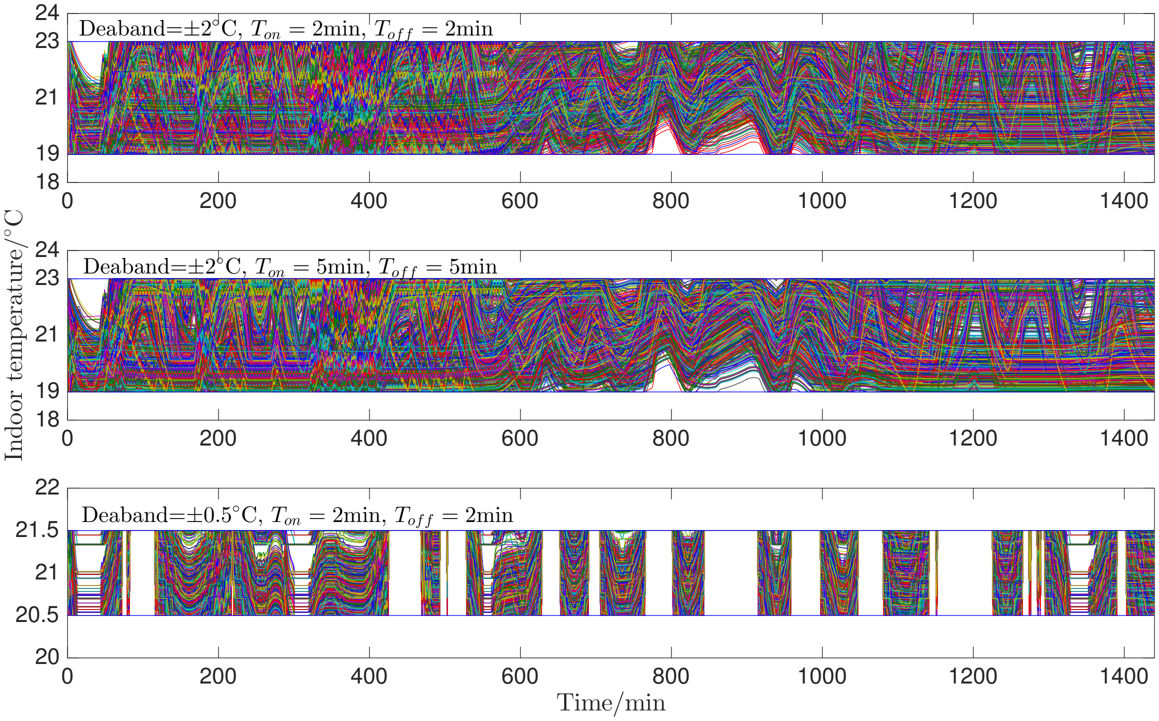

Figure 2.5: Indoor air temperature evolution (winter) responding to load following control signal.

- The tracking performance is slightly compromised if the lockout time is enlarged from 2 min to 5 min. The tracking error ϵ is 0.23% which is nearly 10 times than the 2-min lockout case. The reason for having this relatively larger error is that, during the device lockout period, the aggregated balancing capacity is impaired due to the loss of controllable TCAs.

- With the lockout time maintained at 2 min, if the contracted comfort requirement is tightened from ±2°C to ±0.5°C, the tracking performance will be severely affected. In this case, tracking error ϵ is 0.49%, which is almost 20 times than the one of ±2°C deadband case. This large error is a direct result of the narrowed power adjusting range due to the narrowed temperature range.

- From the third plots of Figure 2.5 and Figure 2.7, it can be readily observed

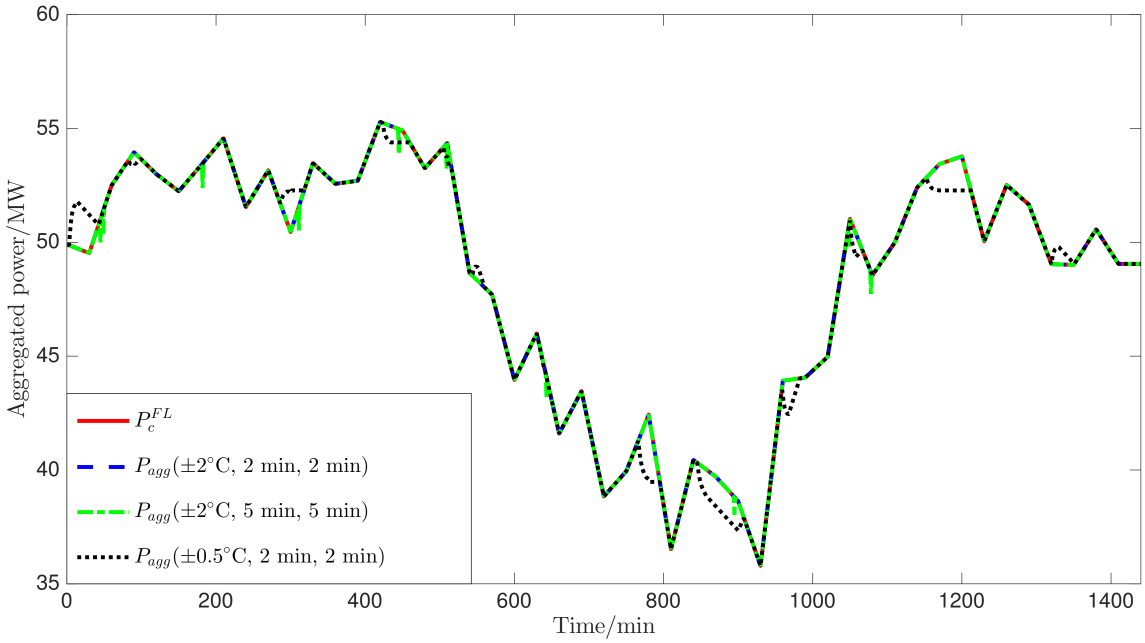

Figure 2.6: Load following signal tracking (winter).

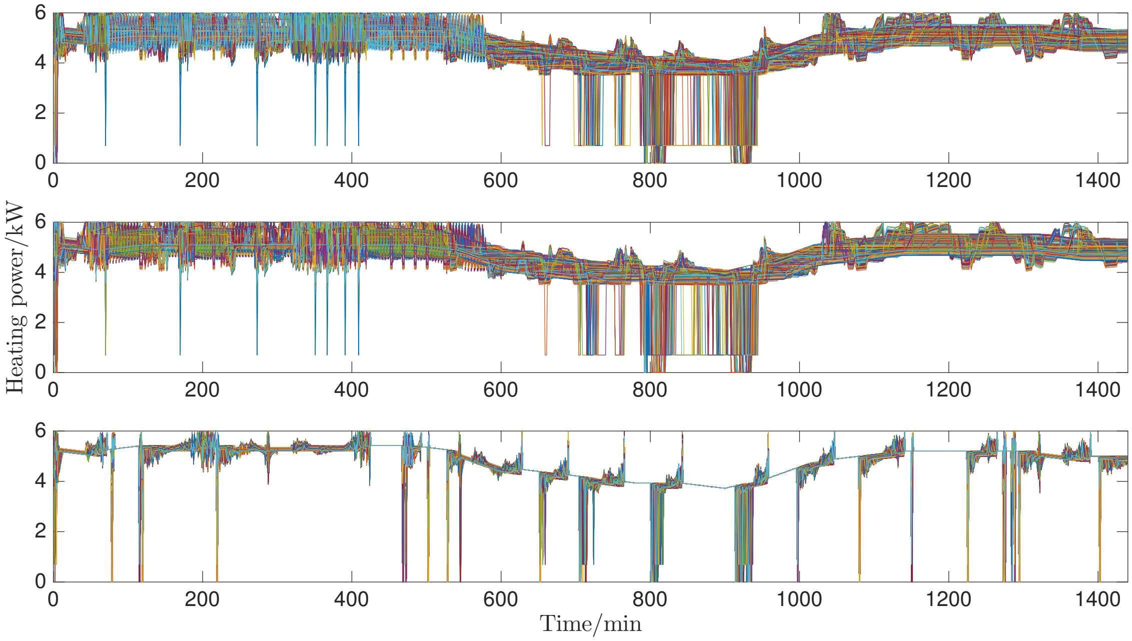

Figure 2.7: Control signals sent to TCAs in the load following tracking scenario.

that temperature evolution and control signals of all TCAs tend to achieve a synchronization due to the narrowed temperature deadband.

- When the temperature deadband width is narrowed down to ±0.5°C, from the third plot of Figure 2.5, we can observe that, in some cases, temperature of the contracted users stays at the upper limit. Comparing the corresponding parts in Figure 2.5 and Figure 2.6, e.g., between the 800th and 1000th minute, we can readily identify the big tracking gap at the time when indoor air temperature is at the upper limit. This tracking gap is a direct result of the gap between the relatively higher balancing signal and the lower aggregated balancing capacity determined by the narrow temperature deadband. In the case of tracking a long-lasting high-value balancing signal, all TCAs try to raise their heating power (or even push to the highest power) in order to chase that signal. In the meantime, the indoor air temperature keeps rising. After reaching the upper temperature limit, the optimal choice for the controller is to adjust the heating power to a value which is lower than the highest one but can keep the temperature at the upper limit. This choice will minimize the gap between the aggregated power consumption and the tracking signal, and will ensure that the indoor air temperature stays within the comfort range.

The balancing capacity is also affected by the average ambient temperature. When using a higher-average temperature profile, intuitively, the balancing performance will be weakened since in some cases, in order to keep a certain comfort level, a TCA unit is forced to turn OFF and then during the lockout period the aggregated balancing capacity is impaired. Figure 2.8 and Figure 2.9 show the indoor air temperature and the balancing performance of 1000 TCAs when using the spring ambient temperature as shown in Figure 2.3. To compare with the winter case, the deadband and minimum ON/OFF time are set to be ±2°C and 2 min, respectively. In addition, the balancing signal is scaled for the spring temperature profile. It can be revealed from Figure 2.8 and Figure 2.9 that:

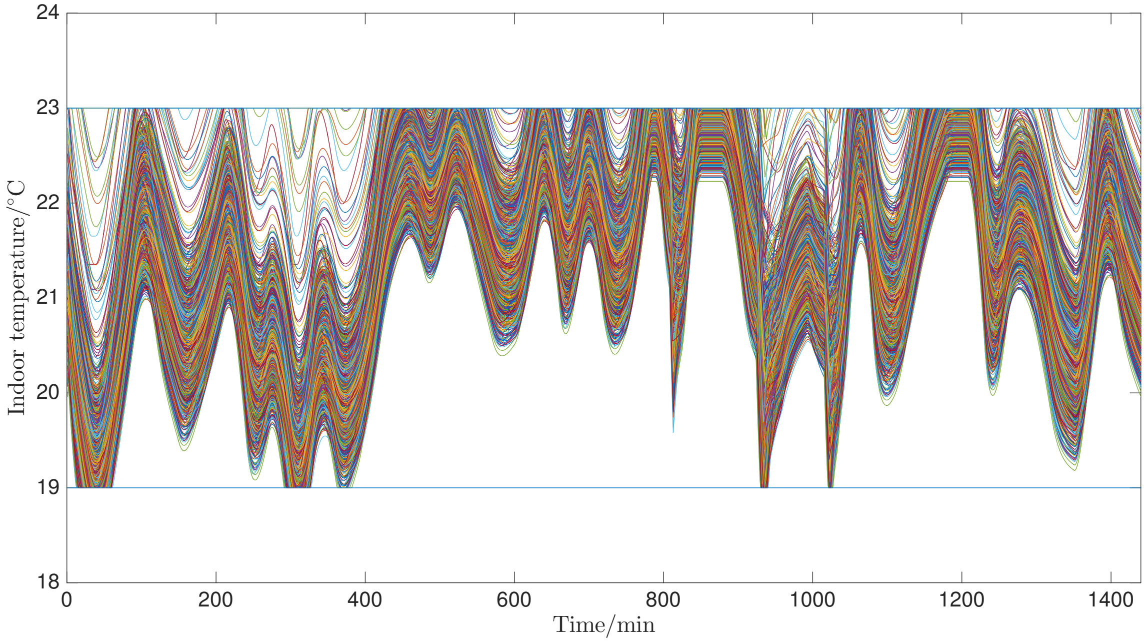

Figure 2.8: Indoor air temperature evolution (spring) responding to load following signal.

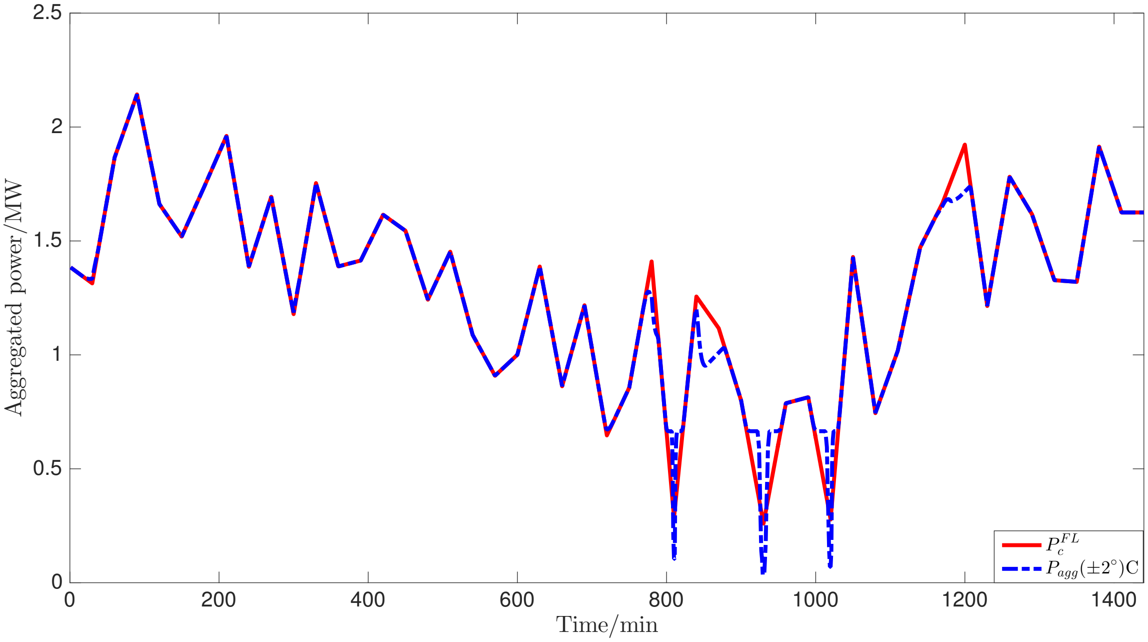

Figure 2.9: Load following signal tracking (spring).

- The aggregated power consumption can track the balancing signal with small errors when the ambient temperature is relatively low.
- When the ambient temperature reaches the peak (around the 1000th minute), some or all of the TCAs have to be turned OFF and be kept for at least $T_{\text{off}} = 2$ min to keep the indoor air temperature within the preset deadband and to protect the unit. Though the deadband is as wide as ±2°C, this turning OFF action still has a severe impact on the balancing capacity. The tracking error ϵ for this case is 1.35%. Though the load following signal has been scaled for this higher-average ambient temperature, the impact of the high temperature can still be reflected from the large tracking error. With this higher-average temperature, TCAs have less flexibility to adjust their heating power. Thus, we can observe a slightly synchronized indoor air temperature evolution profile.
- If the ambient temperature keeps rising, the service quality will be even worse. In this case, cooling TCAs should cooperate with heating TCAs to accomplish the tracking task. Furthermore, indoor humidity may also be taken into account to improve users' comfort level. By involving humidifiers and dehumidifiers in this program, the balancing capacity can be enhanced. Aggregating and controlling a collection of air conditioners, humidifiers, and dehumidifiers will be discussed in the future work.

2.2.5.4 Response to ACE signal

In this section, we shall test how 1000 TCAs respond to the fast changing ACE signal under the circumstances of different temperature deadband widths and lockout time lengths. With the winter ambient temperature profile as shown in Figure 2.3, three sets of test results, i.e., (±2°C, $T_{\text{on}} = 2$ min, $T_{\text{off}} = 2$ min), (±2°C, $T_{\text{on}} = 5$ min, $T_{\text{off}} = 5$ min), and (±0.5°C, $T_{\text{on}} = 2$ min, $T_{\text{off}} = 2$ min) are shown in Figure 2.10 and

Figure 2.11. The corresponding control signals can be found in Figure 2.12. It is worth

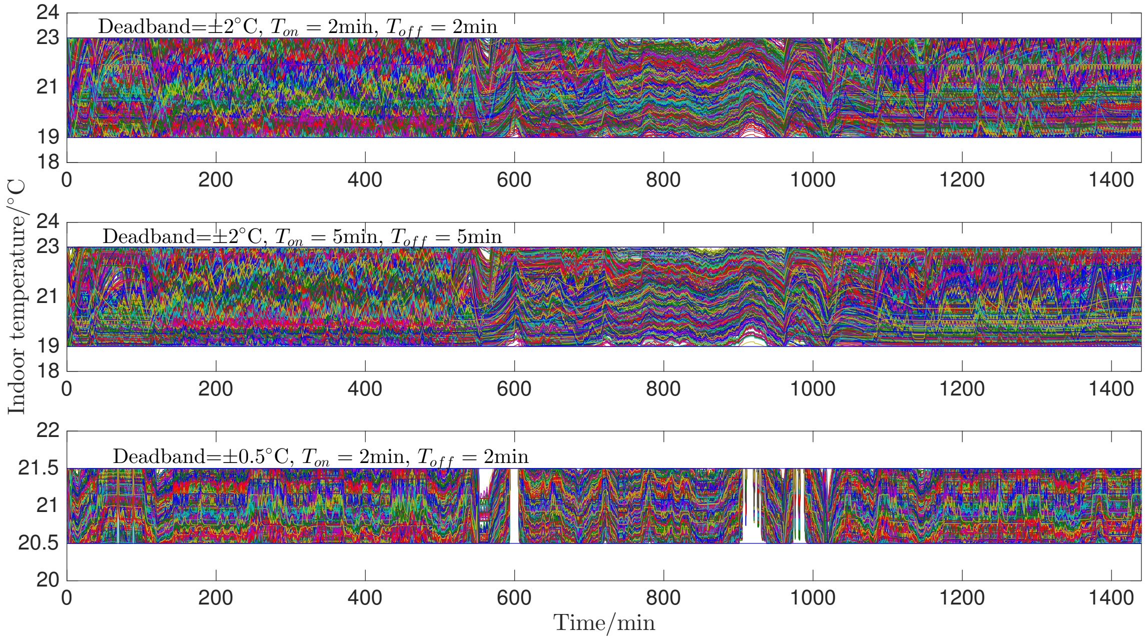

Figure 2.10: Indoor air temperature evolution (winter) responding to ACE signal.

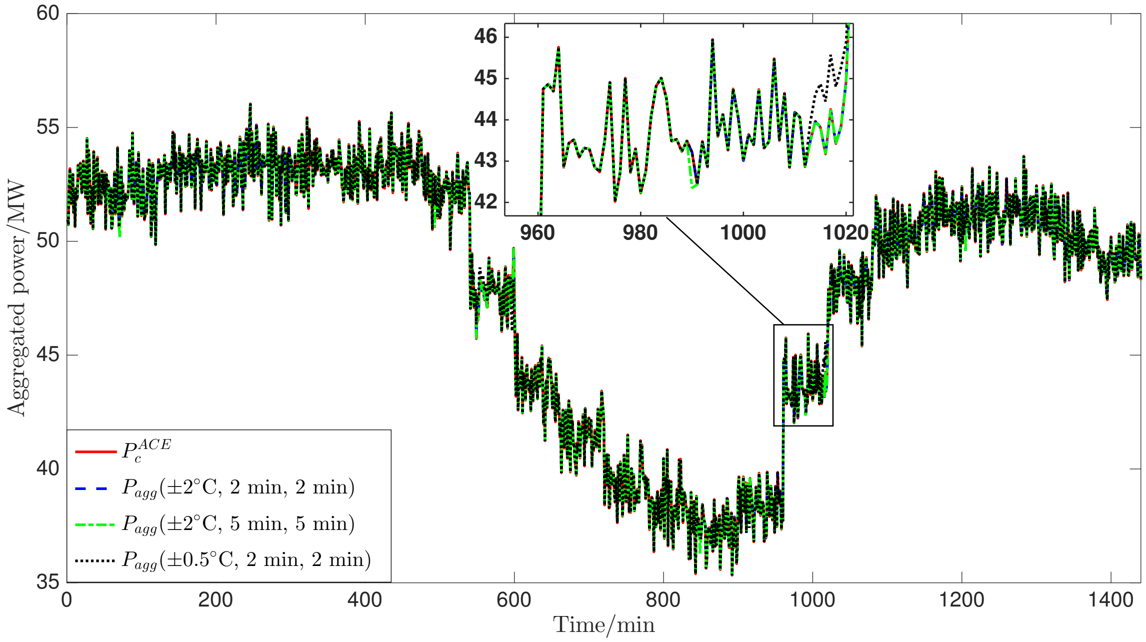

Figure 2.11: ACE signal tracking (winter).

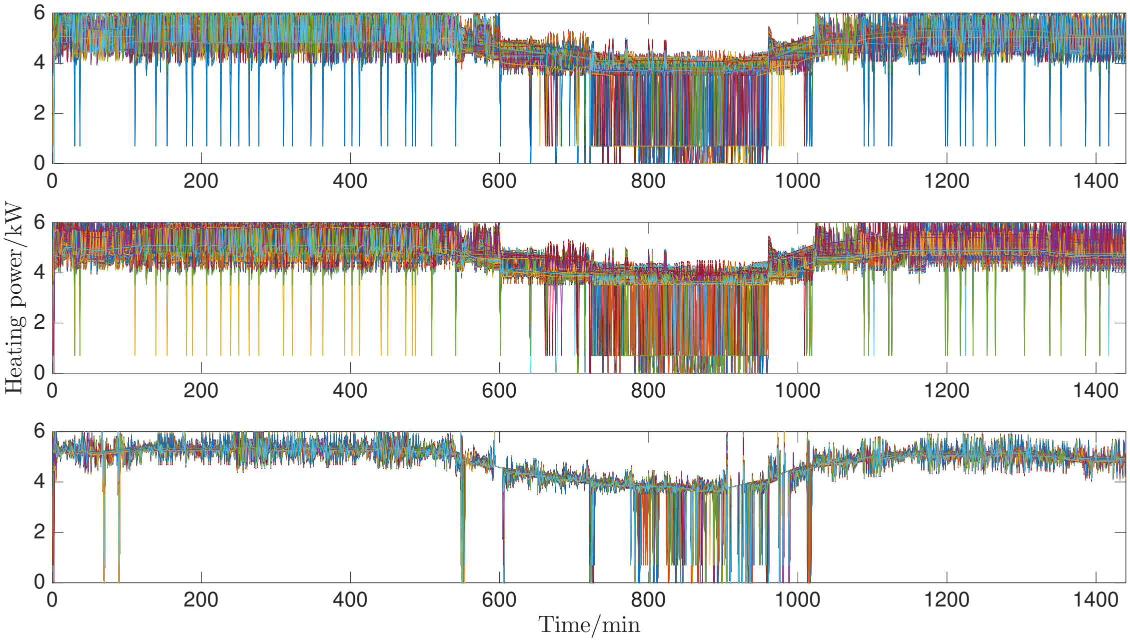

Figure 2.12: Control signals sent to TCAs in the ACE tracking scenario.

mentioning that, no matter in which parameter setup, the optimization problem is always feasible during the control process. In other words, the requirements on TCA minimum ON/OFF time can be guaranteed. It can be summarized from the test results that:

- The indoor air temperature of all end-users is well restricted within the preset comfort range. Compared with the load following signal tracking case, the temperature profiles are less synchronized.

- With a wider temperature deadband, the aggregated power consumption P_{agg} can track the balancing signal P_c^{ACE} better; if the deadband is narrowed, the tracking performance is compromised. To have a clear view of the fast ACE signal tracking performance, we included a zoom-in window between the 960th and the 1020th min in Figure 2.11. With a wider comfort range ±2°C and shorter lockout time 2 min, the tracking error ϵ is 0.04%. When the lockout time is enlarged to 5 min, the tracking error ϵ is increased to 0.16%. In addition, similar as the load following case, a narrow comfort range ±0.5°C results in a tracking error as large as 0.26%.

- Comparing the third plots in Figure 2.7 and Figure 2.12: with the same narrow temperature deadbands, control signals responding to the ACE signal are less synchronized than the ones responding to the load following control signal. Furthermore, in the ACE tracking scenario, the possibility for all end-users staying at the temperature upper limit is quite low.

Note that, with a higher-average ambient temperature profile, the ACE signal tracking performance is not satisfying because of the same reason for the load following signal tracking. The tests in Section 2.2.5.3 and Section 2.2.5.4 were conducted on a PC with Intel Core 2 1.06 GHz without parallel computing. The time elapsed for obtaining the optimal control sequence is around 0.8 second. We also conducted a simulation for 3000 TCAs. The first several steps were slightly slow, which took around 3 seconds to converge. After that, we properly chose the initial guess as $[\hat{u}^*(k{+}1|k)^\mathsf{T}\ \cdots\ \hat{u}^*(k{+}N{-}1|k)^\mathsf{T}\ \hat{u}_\mathrm{g}(k{+}N|k)^\mathsf{T}\ \hat{r}^*(k{+}1|k)^\mathsf{T}\ \cdots\ \hat{r}^*(k{+}N{-}1|k)^\mathsf{T}\ \hat{r}_\mathrm{g}(k{+}N|k)^\mathsf{T}\ \hat{\psi}^*(k+1|k)^\mathsf{T}\ \cdots\ \hat{\psi}^*(k+N-1|k)^\mathsf{T}\ \hat{\psi}_\mathrm{g}(k+N|k)^\mathsf{T}\ \hat{\phi}^*(k+1|k)^\mathsf{T}\ \cdots\ \hat{\phi}^*(k+N-1|k)^\mathsf{T}\ \hat{\phi}_\mathrm{g}(k+N|k)^\mathsf{T}]^\mathsf{T}$, where $\hat{u}^*(k+j|k)$, $\hat{r}^*(k+j|k)$, $\hat{\psi}^*(k+j|k)$, and $\hat{\phi}^*(k+j|k)$, $j = 1, \ldots, N-1$, are the optimal control sequence calculated at time instant k, and $\hat{u}_\mathrm{g}(k+N|k)$, $\hat{r}_\mathrm{g}(k+N|k)$, $\hat{\psi}_\mathrm{g}(k+N|k)$, and $\hat{\phi}_\mathrm{g}(k+N|k)$ are chosen for keeping the running status at time $k+N-1$. By doing so, the optimal control sequence could be obtained within around 1.7 seconds. It is known that the time consumption of mixed integer programming is non-trivial, however, if the MATLAB code is converted to C/C++ code, the running efficiency would be much improved. In addition, since the time scale of the service is minute, it is acceptable to obtain the control signal in seconds. Finally, since aggregators are distributed in different areas to guarantee the communication and control quality, each single aggregator will not be in charge of a too-large population of TCAs. Thus, the computational scalability issue for a too-large population of TCAs does not exist.

Remark 2.4: The proposed control method is for controlling VFD-equipped TCAs. However, the VFDs would introduce non-trivial capital costs. It is quite possible that not all TCAs are equipped with VFDs. In this case, (2.22) becomes

$$u_i(k+j|k) \in \mathbb{U}_i, \tag{2.52}$$

where $\mathbb{U}_i$ is either $\{0\} \cup [\underline{u}_i, \overline{u}_i]$ or $\{0, \overline{u}_i\}$. In a more special case that no TCA is equipped with VFDs, the proposed control scheme can be specialized to a pure ON/OFF control. In this case, (2.22) becomes

$$u_i(k+j|k) \in \{0, \bar{u}_i\}. \tag{2.53}$$

Then the optimization problem becomes an integer nonlinear programming (INLP) problem. In both of the above cases, the set $\{0, \overline{u}_i\}$ can be easily constructed by setting $\underline{u}_i = \overline{u}_i$. The scenario where all TCAs are VFD-free will be discussed in Section 2.3 via a DMPC scheme. ■

Remark 2.5: Though the proposed control scheme provides a promising performance, it is designed by assuming that a fast bidirectional communication between TCAs and the controller has already been in place. This assumption might make the proposed control uneconomical to implement. Without upgrading the current communication network, it is possible to design advanced control techniques which include state estimation to decrease the metering and transmission rate, or to adopt internet to reduce the communication cost. In addition, at this point, we do believe that the fast two-way digital communication network would be a standard in the future smart grid. ■

Remark 2.6: The control strategy in this chapter is designed with an assumption that no disturbance exists. Firstly, we assume that all participated end-users are contracted to give their control to the centralized controller. Thus, during the control process, no user would quit the program or take over the control from the centralized controller. However, in reality, it is possible that, in some circumstances, some users may suspend their TCAs, which results in a loss of balancing capacity. Secondly, we assume that no disturbance exists in the individual TCA dynamics. This type of disturbance is mainly caused by human activities, e.g., party, window opening, etc. Compared to the first type of disturbance, the second one has less impact on the tracking but more on temperature control. In the future work, both of the two disturbances shall be considered in a robust/stochastic control design. ■

2.3 DMPC Design

Remark 2.4 indicates that, in practical applications, it is possible that all connected TCAs are VFD-free. Thus, in this section, it is necessary to specify the proposed approaches for the VFD-free case. In addition, to solve the possible heavy computational load issue, a DMPC scheme will be established for the aggregator.

2.3.1 DMPC Scheme

Still using the dynamic model in (2.2) for the ith TCA, the predicted state vector is defined as

$$\mathbf{x}_i(k) = \begin{bmatrix} x_i(k+1|k) \\ \vdots \\ x_i(k+N|k) \end{bmatrix} \in \mathbb{R}^N, \tag{2.54}$$

where $x_i(k+j|k)$ is the predicted state of the ith TCA at time $k+j$ with the knowledge of the state at time k, and N is the prediction horizon. The control sequence containing the control signals from time k to $k+N-1$ is defined as

$$\mathbf{u}_i(k) = \begin{bmatrix} u_i(k|k) \\ \vdots \\ u_i(k+N-1|k) \end{bmatrix} \in \mathbb{R}^N. \tag{2.55}$$

In this section, it is assumed that the ambient temperature information can be exactly predicted. Using forecasted ambient temperature will be discussed in the future work. The known external input vector can be defined as

$$\boldsymbol{\omega}_i(k) = \begin{bmatrix} \omega_i(k|k) \\ \vdots \\ \omega_i(k+N-1|k) \end{bmatrix} \in \mathbb{R}^N. \tag{2.56}$$

Then the system dynamics of the ith TCA in a predictive form is represented as

$$\mathbf{x}_i(k) = \mathcal{M}_i x_i(k|k) + \mathcal{C}_i \mathbf{u}_i(k) + \mathcal{D}_i \boldsymbol{\omega}_i(k), \tag{2.57}$$

where

$$\mathcal{M}_i = \begin{bmatrix} A_i \\ A_i^2 \\ \vdots \\ A_i^N \end{bmatrix}, \mathcal{C}_i = \begin{bmatrix} B_i & 0 & \cdots & 0 \\ A_iB_i & B_i & \cdots & 0 \\ \vdots & & \ddots & \vdots \\ A_i^{N-1}B_i & A_i^{N-2}B_i & \cdots & B_i \end{bmatrix},$$

$$\mathcal{D}_i = \begin{bmatrix} D_i & 0 & \cdots & 0 \\ A_iD_i & D_i & \cdots & 0 \\ \vdots & & \ddots & \vdots \\ A_i^{N-1}D_i & A_i^{N-2}D_i & \cdots & D_i \end{bmatrix}.$$

2.3.2 Distributed Objective Function

The control objective is same as the one in Section 2.2, namely 1) to maintain the indoor air temperature of each end-user within the specified comfortable deadband and, 2) the aggregated power consumption of all TCAs should track the balancing signal provided by the ISO. Let x_0 denote the most comfortable temperature, then the first objective can be represented as

$$\mathcal{J}_{i1}(k) = \sum_{j=1}^{N} \left[(x_i(k+j|k) - x_0)^\mathsf{T} Q (x_i(k+j|k) - x_0)\right], \tag{2.58}$$

where $Q \in \mathbb{R}^{1\times 1}$ is the weighting matrix. With the constant term neglected, $\mathcal{J}_{i1}(k)$ can be rewritten as

$$\begin{aligned} \mathcal{J}_{i1}(k) &\approx \sum_{j=1}^{N} [x_i(k+j|k)^\mathsf{T} Q x_i(k+j|k) - 2x_0^\mathsf{T} Q x_i(k+j|k)] \\ &= \mathbf{x}_i(k)^\mathsf{T} \mathcal{Q} \mathbf{x}_i(k) - 2\mathcal{P}^\mathsf{T} \mathbf{x}_i(k), \end{aligned} \tag{2.59}$$

where

$$\mathcal{Q} = \text{diag}\{Q\} \in \mathbb{R}^{N\times N}, \mathcal{P} = \left[x_0^\mathsf{T} Q \; x_0^\mathsf{T} Q \; \cdots \; x_0^\mathsf{T} Q\right]^\mathsf{T}. \tag{2.60}$$

Substituting (2.57) into (2.59), we can obtain that

$$\mathcal{J}_{i1}(k) \approx \mathbf{u}_i(k)^\mathsf{T}\mathcal{C}_i^\mathsf{T}\mathcal{Q}\mathcal{C}_i\mathbf{u}_i(k) + 2\left[\left(\mathcal{M}_i x_i(k|k) + \mathcal{D}_i\boldsymbol{\omega}_i(k)\right)^\mathsf{T}\mathcal{Q}\mathcal{C}_i - \mathcal{P}^\mathsf{T}\mathcal{C}_i\right]\mathbf{u}_i(k). \quad (2.61)$$

For the second objective, if using a centralized controller, the controller needs to gather and process the information of all TCAs. The computational complexity will increase dramatically if the aggregator takes charges of too many TCAs. To realize a tractable control, in this section, we propose a DMPC scheme by adopting an alternating searching method. In this scheme, every end-user only needs to solve its local optimization problem using neighbour TCAs' information iteratively. The detailed procedure will be discussed in Section 2.3.5. Specifically, for the ℓth iteration at time k, $\mathcal{J}_{i1}(k)$ is modified to

$$\mathcal{J}_{i1}^{\ell}(k) \approx \mathbf{u}_i^{\ell}(k)^\mathsf{T}\mathcal{C}_i^\mathsf{T}\mathcal{Q}\mathcal{C}_i\mathbf{u}_i^{\ell}(k) + 2\left[\left(\mathcal{M}_i x_i(k|k) + \mathcal{D}_i\boldsymbol{\omega}_i(k)\right)^\mathsf{T}\mathcal{Q}\mathcal{C}_i - \mathcal{P}^\mathsf{T}\mathcal{C}_i\right]\mathbf{u}_i^{\ell}(k). \quad (2.62)$$

The second objective for the ith TCA in the ℓth iteration at time k can be represented as

$$\mathcal{J}_{2i}^{\ell}(k) = \sum_{j=0}^{N}\left[\left(u_i^{\ell}(k+j|k) - u_{i0}^{\ell}(k+j)\right)^\mathsf{T} R\left(u_i^{\ell}(k+j|k) - u_{i0}^{\ell}(k+j)\right)\right], \quad (2.63)$$

where $R \in \mathbb{R}^{1\times 1}$ is the weighting matrix. Herein, we have

$$u_{i0}^{\ell}(k+j) = u_0(k+j) - \sum_{\imath>i}^{m} u_{\imath}^{\ell-1*}(k+j) - \sum_{\imath<i}^{i-1} u_{\imath}^{\ell*}(k+j) \quad (2.64)$$

as the local tracking objective for the ith TCA in the ℓth iteration at time $k+j$. $u_{\imath}^{\ell*}(k+j)$ is the local optimal power consumption at time $k+j$ in the ℓth iteration. This indicates that, in a specific iteration at each time instant, TCA i only needs to contribute its own effort to the global balancing service. With the constant term neglected, we have

$$\begin{aligned}\mathcal{J}_{2i}^{\ell}(k) &\approx \sum_{j=0}^{N-1}\left[u_i^{\ell}(k+j|k)^{\mathsf{T}}Ru_i^{\ell}(k+j|k) - 2u_{i0}^{\ell}(k+j)Ru_i^{\ell}(k+j|k)\right]\\ &= \mathbf{u}_i^{\ell}(k)^{\mathsf{T}}\mathcal{R}\mathbf{u}_i^{\ell}(k) + 2q_i^{\ell\mathsf{T}}\mathbf{u}_i^{\ell}(k),\end{aligned} \tag{2.65}$$

where

$$\begin{aligned}&\mathcal{R} = \mathrm{diag}\{R\} \in \mathbb{R}^{N\times N}\\ &q_i^{\ell} = -\mathcal{R}\left[u_{i0}^{\ell}(k)^{\mathsf{T}} \ \cdots \ u_{i0}^{\ell}(k+N-1)^{\mathsf{T}}\right]^{\mathsf{T}}.\end{aligned} \tag{2.66}$$

Thus, the overall objective function for the ith TCA in the ℓth iteration at time k is expressed as

$$\begin{aligned}\mathcal{J}_i^{\ell}(k) &= \mathcal{J}_{1i}^{\ell}(k) + \mathcal{J}_{2i}^{\ell}(k)\\ &= \mathbf{u}_i^{\ell}(k)^{\mathsf{T}}\left(\mathcal{C}_i^{\mathsf{T}}\mathcal{Q}\mathcal{C}_i + \mathcal{R}\right)\mathbf{u}_i^{\ell}(k) + 2\left[\left(\mathcal{M}_i x_i(k|k) + \mathcal{D}_i\boldsymbol{\omega}(k)\right)^{\mathsf{T}}\mathcal{Q}\mathcal{C}_i - \mathcal{P}^{\mathsf{T}}\mathcal{C}_i + q_i^{\ell\mathsf{T}}\right]\mathbf{u}_i^{\ell}(k).\end{aligned} \tag{2.67}$$

2.3.3 State and Input Constraints

To keep the end-users' comfort in a certain level, the indoor air temperature at any time must be within a specific range. Still let σ denote the deadband width, then the state constraint of the DMPC problem can be written as

$$\underline{x} \le x_i^{\ell}(k+j|k) \le \overline{x}, \forall j = 1, \ldots, N, \tag{2.68}$$

where $\underline{x} = x_0 - \sigma$ and $\overline{x} = x_0 + \sigma$ are the lower and upper bounds of the comfortable air temperature, respectively. Substituting (2.57) into (2.68), we have

$$\begin{aligned} \mathcal{C}_i \mathbf{u}_i^\ell(k) &\leq \overline{x}\mathbf{1}_N - \mathcal{M}_i x_i(k|k) - \mathcal{D}_i \boldsymbol{\omega}(k) \\ -\mathcal{C}_i \mathbf{u}_i^\ell(k) &\leq -\underline{x}\mathbf{1}_N + \mathcal{M}_i x_i(k|k) + \mathcal{D}_i \boldsymbol{\omega}(k), \end{aligned} \tag{2.69}$$

where $\mathbf{1}_N = [1\ 1\ \ldots\ 1]^\mathsf{T} \in \mathbb{R}^N$.

In this section, since the TCAs are VFD-free, thus only having ON and OFF status. Let $\overline{u}_i$ be the rated power for the ith TCA, then the input constraint for the DMPC problem is represented as

$$u_i^\ell(k+j|k) \in \{0, \overline{u}_i\}, \forall i = 1, \ldots, m,\ j = 0, \ldots, N-1. \tag{2.70}$$

2.3.4 Lockout Effect Constraints

In certain circumstances, in order to maintain the indoor air temperature or to track the load balancing signal, one TCA might be turned ON and OFF frequently. This frequent working status changing puts much pressure on the appliance. Similar as Section 2.2, to protect the appliance and to have a good maintenance, the minimum ON time T_{on} and minimum OFF time T_{off} should also be set. For the ith TCA in the time interval $[k, k+1]$ at the ℓth iteration, denote $r_i^\ell(k) = 1(0)$ the ON(OFF) status, and denote the nearest switching-ON(-OFF) time to be $t_{\text{on}_i}^\ell(k)(t_{\text{off}_i}^\ell(k))$. Similar as in Section 2.2.3, without considering the prediction, the power consumption of the ith

TCA in the ℓth iteration at time instant k can be represented as

$$u_i^\ell(k) = r_i^\ell(k)\overline{u}_i, \tag{2.71}$$

$$r_i^\ell(k) = \begin{cases} 0, & k+1-T_{\text{off}} \leq t_{\text{off}_i}^\ell(k-1), \\ 1, & k+1-T_{\text{on}} \leq t_{\text{on}_i}^\ell(k-1), \\ \{0,1\}, & \text{else}. \end{cases} \tag{2.72}$$

$$t_{\text{on}_i}^\ell(k) = \begin{cases} k, & \Delta_i^\ell(k) = 1, \\ t_{\text{on}_i}^\ell(k-1), & \Delta_i^\ell(k) \in \{-1,0\}, \end{cases} \tag{2.73}$$

$$t_{\text{off}_i}^\ell(k) = \begin{cases} k, & \Delta_i^\ell(k) = -1, \\ t_{\text{off}_i}^\ell(k-1), & \Delta_i^\ell(k) \in \{0,1\}, \end{cases} \tag{2.74}$$

where $\Delta_i^\ell(k) = r_i^\ell(k) - r_i^\ell(k-1)$. Consequently, constraints (2.71)–(2.74) together with (2.67) formulate the DMPC problem with lockout time considered. In addition, $r_i^\ell(k)$, $t_{\text{on}_i}^\ell(k)$, and $t_{\text{off}_i}^\ell(k)$ are the decision variables.

The methodology for dealing with the above time-integrated interdependent logic constraints can exactly follow the similar lines as in Section 2.2.4. Herein, since the alternating searching method is adopted, all variables must be endorsed with the iteration number ℓ. To avoid redundancy, the converted inequality constraints are directly given here as follows.

$$\begin{aligned} &(1-2r_i^\ell(k+j|k))(t_{\text{on}_i}^\ell(k+j|k) - t_{\text{off}_i}^\ell(k+j|k)) \\ \leq &(1-r_i^\ell(k+j|k))T_{\text{on}} - r_i^\ell(k+j|k)T_{\text{off}}, \\ &r_i^\ell(k+j|k) \in \{0,1\}, \end{aligned} \tag{2.75}$$

$$\begin{aligned}&\psi_{i0}^{\ell}(j)[\psi_{i1}^{\ell}(j) + r_i^{\ell}(k+j-1|k) - r_i^{\ell}(k+j|k) + \epsilon]\\ -&\psi_{i1}^{\ell}(j)[\psi_{i1}^{\ell}(j) + r_i^{\ell}(k+j-1|k) - r_i^{\ell}(k+j|k) - \epsilon] \leq 0,\end{aligned} \tag{2.76}$$

and

$$\begin{aligned}&\phi_{i0}^{\ell}(j)[\phi_{i1}^{\ell}(j) - r_i^{\ell}(k+j-1|k) + r_i^{\ell}(k+j|k) + \epsilon]\\ -&\phi_{i1}^{\ell}(j)[\phi_{i1}^{\ell}(j) - r_i^{\ell}(k+j-1|k) + r_i^{\ell}(k+j|k) - \epsilon] \leq 0.\end{aligned} \tag{2.77}$$

In the above inequalities, definitions and derivations of $\psi_{i0}^{\ell}(j)$, $\psi_{i1}^{\ell}(j)$, $\phi_{i0}^{\ell}(j)$, and $\phi_{i0}^{\ell}(j)$ are similar as in Section 2.2.4 except for the iteration number ℓ. The formulated problem for each TCA is an integer nonlinear programming (INLP) problem. Branch-and-Bounded algorithm is used in this section to solve this type of problem.

2.3.5 Control Scheme Description

Since all TCAs need to cooperate to fulfill the coupling input constraints, each TCA must know this constraint together with the information of its neighbours before it can determine its own optimal action. Since the alternating searching technique allows the local optimization to use fixed global information and the convergency is guaranteed, the DMPC scheme will be established based on it. Compared to the centralized MPC, the problem size of the proposed distributed MPC is dramatically reduced from O^{3mN} to O^{3N}. When the number of TCAs increases, the advantage of this distributed controller is more apparent. The convergence is accelerated by replacing $u_i^{\ell-1*}(k+j)$ immediately by $u_i^{\ell*}(k+j)$ for the optimization of the next TCA as shown in (2.78). If the initial values are appropriately chosen, the result can converge in few iterations. The control procedure for the ℓth iteration at time k is

- **Step 1**

  Each TCA unit $(i = 1, \ldots, m)$ initializes its optimizer $\mathbf{u}_i^{\ell}(k)$ for the ℓth iteration, obtains the balancing signal $u_0(k+j)$, $j = 1, \ldots, N$ from the ISO or aggregator, and receives information from neighbour TCAs.

- **Step 2**

  Each TCA unit ($i = 1, \ldots, m$) carries out one iteration for its own subproblem

  $$\begin{aligned} &\min\ (2.67) \\ &\text{s.t. } (2.69),\ (2.75),\ (2.76) \text{ and } (2.77), \end{aligned}$$

  to obtain $\mathbf{u}_i^{\ell*}(k)$, where

  $$u_{i0}^{\ell}(k+j) = u_0(k+j) - \sum_{\imath>i}^{m} u_\imath^{\ell-1*}(k+j) - \sum_{\imath<i}^{i-1} u_\imath^{\ell*}(k+j). \tag{2.78}$$

- **Step 3**

  Compare the error of the results of two consecutive iterations. If the error is smaller than the specified tolerance δ, apply $\overline{u}_i r_i^{\ell*}(k|k)$ to the corresponding TCA and wait for the signal to continue to time $k+1$; if not, $\ell = \ell + 1$ and **GOTO Step 2**.

2.3.6 Case Study

2.3.6.1 Case Study Setup

In this section, the ETP model parameters are the same as those in Section 2.2.5; the deadbands for the indoor air temperature are set to be ±2°C, ±1.5°C, and ±1°C for comparisons; the average rated power of each TCA unit is 6 kW; the minimum ON/OFF time are selected to be 2 minutes, and 1 minute, respectively. To have a clear view of the temperature evolution, only 20 TCAs are included in this case study. The prediction horizon is set to be $N = 4$ min by following the additional prediction horizon constraint (2.49). The ambient temperature is still taken from the meteorological station located in Victoria International Airport, BC, Canada. In addition, the balancing signal construction can be referred to Section 2.2.5.2.

2.3.6.2 Response to Load Following Control Signal

The indoor air temperature evolution of 20 agents (±2°C deadband) and the ambient temperature in a day are shown in Figure 2.13. It can be readily observed that the indoor air temperature of all end-users is well maintained within the preset deadband.

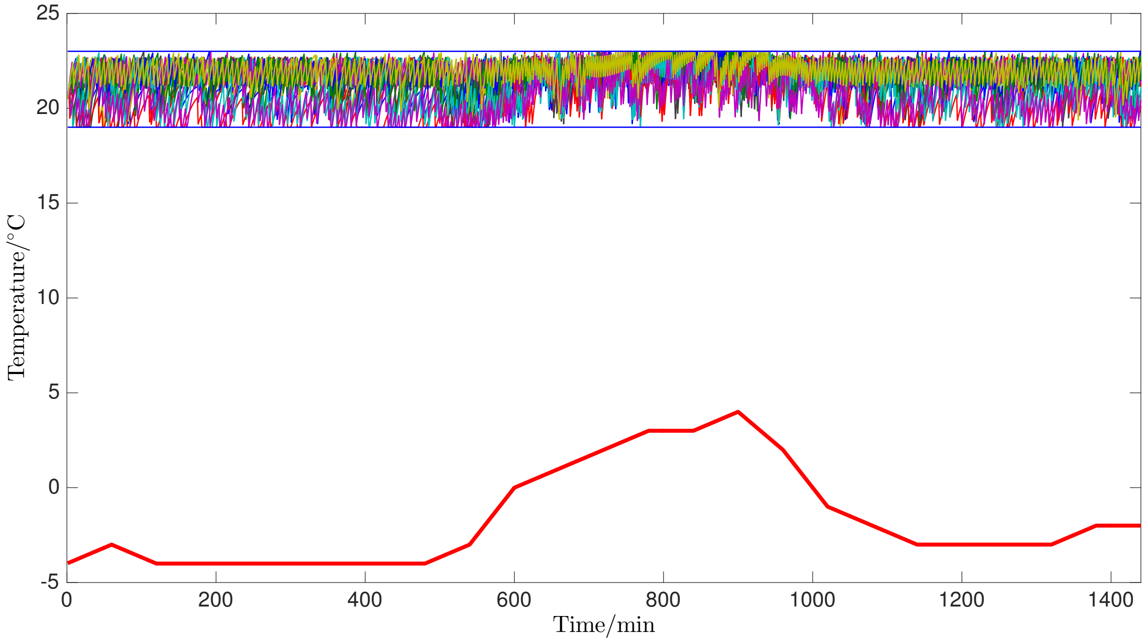

Figure 2.13: indoor air temperature of 20 agents (±2°C) and outdoor temperature.

To clearly show the control signal tracking performance, we only randomly pick up a 100-minute window since the plotted lines will overlap if the entire length is shown. The baseline power consumption, load following signal, and the aggregated power consumption of 20 TCAs from the 77th minute to the 176th minute are shown in Figure 2.14. Herein, narrower deadband cases, i.e., ±1.5°C and ±1°C, are included to investigate the impact of the deadband width on the tracking performance. It can be noticed that, the aggregated power consumption $P_{agg}(\pm 2°\text{C})$ can track the

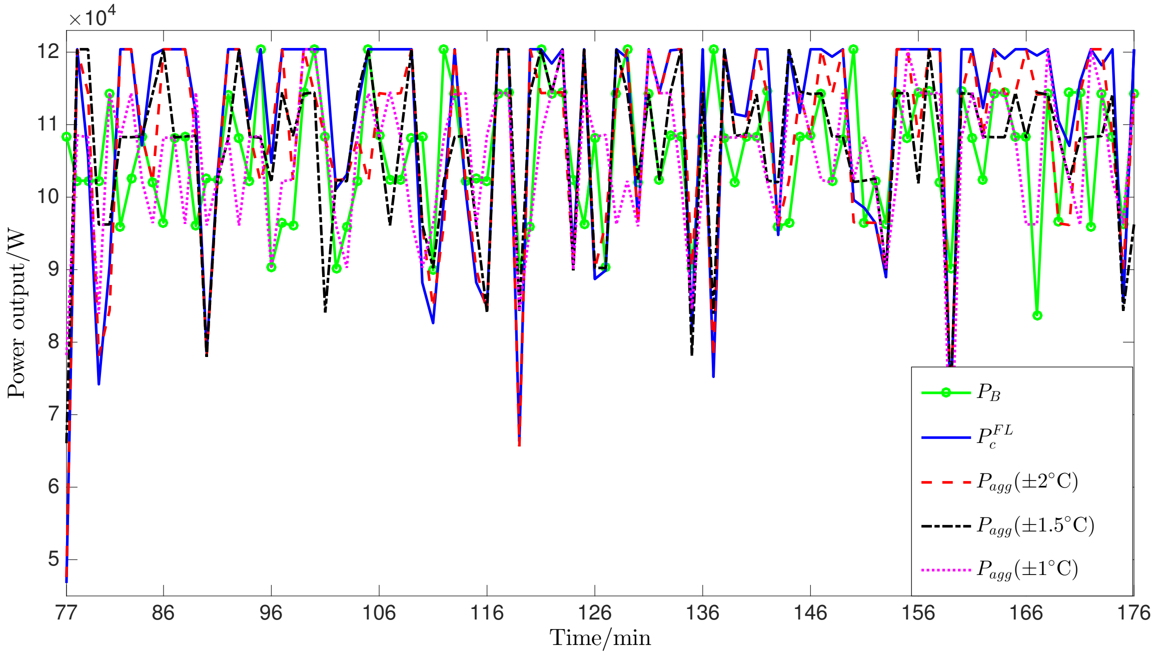

Figure 2.14: Load balancing signal tracking performance.

load following signal not perfectly but pretty well, and only small deviations exist between P_{agg} and P_c^{FL}. If using a centralized controller, this deviation could be further reduced, however, the computing time would be increased. We can also see from the comparison that deviations become larger as the deadband being narrowed. The relative errors in the 100-minute interval are 4.2%, 7.9%, and 12% for ±2°C, ±1.5°C, and ±1°C cases, respectively. In a whole-day interval, the relative errors are 9.3%, 11.5%, and 14.9%, respectively. In this case study, within 1440 minutes, only 29 cases (2%) need 4-5 iterations to converge. Each iteration only costs around 0.04 seconds, revealing the high efficiency of the proposed DMPC controller. Time elapsed for a centralized MPC controller to obtain the optimal solutions of all TCAs at one time instant is around 0.3 second.

2.4 Conclusions

Aggregation modeling and control of a population of TCAs for DR are considered in this chapter. A direct stacking model is constructed to allow the local aggregator to have a global and accurate view of the running status of terminal TCAs. The proposed model is effective for TCAs of which an arbitrary fraction is VFD-equipped. A centralized MPC scheme is firstly investigated for the secondary frequency control. Furthermore, a DMPC scheme is studied to reduce the computational load of the centralized controller. In both of the two predictive control schemes, terminal lockout constraints are firstly formulated as time-integrated interdependent logic conditions. A novel approach of converting logic conditions into inequalities is proposed to facilitate the optimization problem. Finally, illustrative examples show that, by adopting the proposed aggregation model and control approaches, end-users' indoor air temperature can be well maintained and the secondary frequency control performance is acceptable.

Chapter 3

Population-Based Aggregation Model and MPC for a Large Population of TCAs

3.1 Introduction

3.1.1 Background and Literature Review

In Chapter 2, it was noted that aggregating and controlling TCAs for DR have attracted increasing attention in the literature. The stacking approach adopted in Chapter 2 is one of the options to aggregate TCAs' dynamics. However, this approach may encounter the problem of heavy computational load when dealing with an extremely large number of TCAs, especially for primary frequency control. Recently, some researchers presented their results on population-based models, yet in different perspectives. In [65], the authors proposed a population-based model for the aggregation of TCAs based on a first-order ETP model. Instead of considering the dynamics of all TCAs, this population-based model partitions TCAs into several equal-length state bins and controls the population migration among different bins. By doing so, the number of TCAs is no longer a threat for the computational load. Authors in [65] also proposed an MPC scheme for the desired trajectory tracking. Based on the first-order ETP dynamics, Sanandaji *et al.* [69] proposed a non-uniform population-based model in which lengths of the state bins are not equal. It is validated in [69] that, the non-uniform state bin may increase the accuracy of the prediction model even with a less number of state bins. However, all of the above existing results adopted the first-order TCA dynamics in which the building mass temperature was ignored. In practical applications, the ETP model would be more accurate if the building mass temperature could be included. In [51], the authors verified the accuracy of the second-order ETP dynamics and proposed a 2-D transition model based on that. They classified the heterogeneous ETP parameter vectors into some clusters, inside which the homogeneous aggregation model was computed. In [51], the control signals broadcasted to all TCAs are switching probabilities, and the local controller of each TCA needs to decide the switching action according to the probability. This will cause a mismatch between the nominal control signal and the actually implemented one. In contrast, in this chapter, all stochastic characters are incorporated into the system model/evolution. Hence, once the control signal is obtained, every TCA has a determined switching action. In addition, in order to take numerous technical constraints into consideration, an MPC scheme [83], which is suitable for solving optimal control problems with state and input constraints, shall be proposed in this chapter to discuss the provision of primary frequency control.

3.1.2 Research Objectives and Contributions

Motivated by the aforementioned points, the main objectives and contributions of this chapter can be summarized as:

- A 2-D population-based model is proposed based on the second-order ETP dynamics to describe the aggregate behavior of a large population of heterogeneous TCAs. The heterogeneity is achieved by considering the TCA parameter distributions in the system transition matrix. Compared to the literature, using probability distributions to derive a 2-D population-based model is new.

- The time-variant character of the system transition matrix is considered in this chapter. A look-up table option is offered to further reduce the computational load.

- An MPC scheme is proposed to obtain the optimal control actions. Besides, in order to implement the control actions with practical situations considered, a detailed implementation procedure is presented to achieve a higher service quality.

- A systematic solution is provided to reduce the possibilities of indoor air temperature limits violation.

3.1.3 Chapter Organization

This chapter is organized as follows. In Section 3.2, the second-order TCA dynamics will be firstly provided; following this, a 2-D population-based model is proposed to aggregate TCAs; detailed derivations of the migration probabilities are provided. The MPC scheme and the post-processing procedure is investigated in Section 3.3. In Section 3.4, feasibility and efficacy of the proposed modeling and control approach are verified by the simulation results. Some discussions on the results are also provided. Section 3.5 concludes this chapter.

3.2 Problem Formulation

3.2.1 Second-Order TCA Dynamics

In this chapter, a second-order ETP model [97,98] is adopted to describe the individual heating TCA dynamics. In differential equations, it can be expressed as

$$\begin{aligned} \dot{T}_i(t) &= \frac{1}{C_a}\left[\frac{1}{R_m}(T_m(t)-T_i(t))+\frac{1}{R_a}(T_a(t)-T_i(t))+Q_a\right], \\ \dot{T}_m(t) &= \frac{1}{C_m}\left[\frac{1}{R_m}(T_i(t)-T_m(t))+Q_m\right], \end{aligned} \tag{3.1}$$

where $T_i(t)$, $T_m(t)$, and $T_a(t)$ are the indoor air temperature, building mass temperature, and ambient temperature (°C), respectively; R_a and R_m are the equivalent thermal resistance for air and mass (°C/W), respectively; C_a and C_m are the equivalent heat capacity (J/°C) for air and building mass temperature, respectively; Q_a and Q_m are the heat flux to the air and mass, respectively. Herein, Q_a comes from three main sources, i.e., internal load, solar, and HVAC systems. Without losing generality, the internal load and solar can be regarded as constant within a narrow time span and thus be omitted, which means that only the heating from the HVAC system is considered. In addition, for the simplicity of presentation, Q_m can be regarded as a constant within a narrow time span and be omitted without affecting the system performance.

The system dynamics in (3.1) can be discretized as

$$\begin{aligned} T_i(k+1) &= aT_i(k)+(1-a)\frac{R_a}{R_a+R_m}T_m(k)+(1-a)\frac{R_m}{R_a+R_m}\left(T_a(k)+R_aQ_a(k)\right), \\ T_m(k+1) &= bT_m(k)+(1-b)T_i(k), \end{aligned} \tag{3.2}$$

where

$$a = e^{-\frac{R_a+R_m}{R_a R_m C_a}\Delta t},$$

$$b = e^{-\frac{1}{R_m C_m}\Delta t}.$$

Herein, Δt is the discrete time step. By omitting the internal load and solar, for an individual TCA, $Q_a(k)$ is the appliance rated power P in ON status and is zero in OFF status.

3.2.2 2-D Population-Based Model

The conventional way to model and control the aggregated power consumption is to gather the full information of all TCAs and design a centralized control protocol for all of them. This type of method can guarantee the optimal control performance; however, the control efficiency is low, especially when the number of TCAs is extremely large. In [65], the authors introduced a population-based model, in which the 1-D state bin is used. With the state bin, TCAs are distributed into several state bins according to their status. In this chapter, the 1-D population-based model will be modified to a 2-D fashion based on (3.2). The accuracy and performance comparisons between first-order and second-order dynamics are presented in [51] and will not be addressed here. The constructed 2-D population migration is shown in Figure 3.1.

In this model, according to different temperature ranges and TCA running status, indoor air temperature T_i and building mass temperature T_m are partitioned by N_i and N_m state bins, respectively. Thereinto, $N_i/2$ of states in T_i are in ON status and the other $N_i/2$ states are in OFF status. Similarly, $N_m/2$ of states in T_m are in ON status and the other $N_m/2$ are in OFF status. Each state bin represents a specific indoor air temperature range, a specific building mass temperature range, and a specific ON/OFF status. The order of the state bins for TCAs in OFF status is

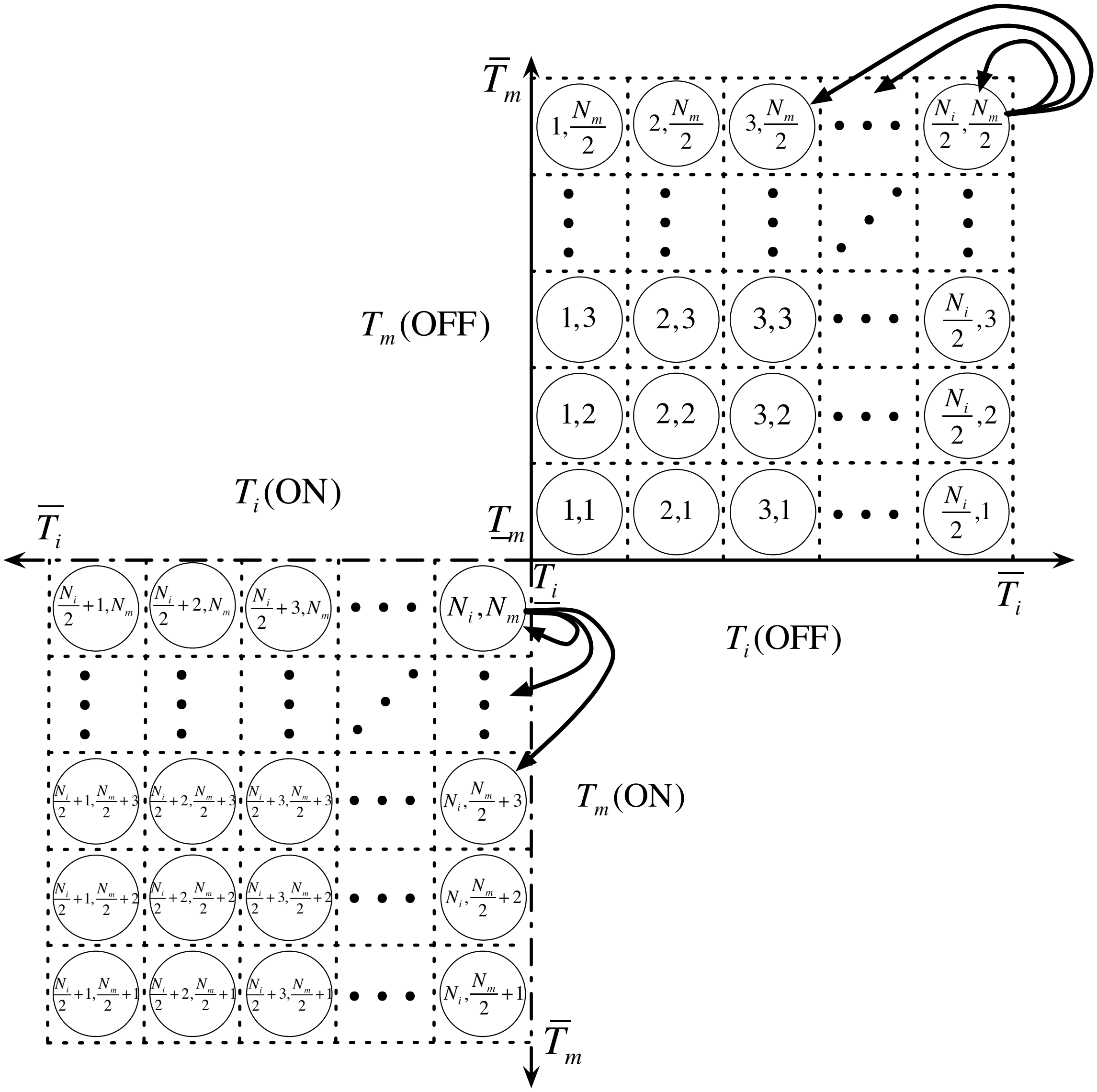

Figure 3.1: The 2-D population-based model.

from $\underline{T}_i$ to $\overline{T}_i$ and from $\underline{T}_m$ to $\overline{T}_m$, where $\underline{T}_i$ and $\overline{T}_i$ are lower and upper bounds of T_i; $\underline{T}_m$ and $\overline{T}_m$ are lower and upper bounds of T_m. When the TCA is in ON status, the order of the states is in an opposite way. The population of TCAs will be distributed into those state bins according to their status. Arrows in Figure 3.1 depict part of the population migration among different bins. Compared to the 1-D state bin, in this 2-D state bin, one T_i bin is further partitioned by $N_m/2$ bins, providing more flexibility for the controller design.

3.2.3 Aggregate Dynamics

The 2-D population-based model can be described as a discrete linear time-varying (LTV) system

$$\begin{aligned} x(k+1) &= A(k)x(k) + B(k)u(k), \\ y(k) &= Cx(k) + Du(k), \end{aligned} \tag{3.3}$$

where $A(k)$, $B(k)$, and $C(k)$ are the system matrix, input matrix, output matrix, and input-to-output matrix, respectively. Definition of the control input $u(k)$ shall be introduced later in Section 3.2.5. Herein, the system state $x(k)$ contains all $N_i N_m/2$ state bins, which can be represented as $x(k) = \left[x_{\text{off}}(k)^\mathsf{T} \; x_{\text{on}}(k)^\mathsf{T}\right]^\mathsf{T}$, where

$$x_{\text{off}}(k) = \begin{bmatrix} x_{1,1}(k) \\ \vdots \\ x_{1,\frac{N_m}{2}}(k) \\ x_{2,1}(k) \\ \vdots \\ x_{2,\frac{N_m}{2}}(k) \\ \vdots \\ x_{\frac{N_i}{2},\frac{N_m}{2}}(k) \end{bmatrix}, \; x_{\text{on}}(k) = \begin{bmatrix} x_{\frac{N_i}{2}+1,\frac{N_m}{2}+1}(k) \\ \vdots \\ x_{\frac{N_i}{2}+1,N_m}(k) \\ x_{\frac{N_i}{2}+2,\frac{N_m}{2}+1}(k) \\ \vdots \\ x_{\frac{N_i}{2}+2,N_m}(k) \\ \vdots \\ x_{N_i,N_m}(k) \end{bmatrix}.$$

Each element $x_{\imath,\jmath}(k)$ stores the number of TCAs in the corresponding state bin $(\imath, \jmath)$ as in Figure 3.1. Or in another way, if normalized by the total number of TCAs, each element $x_{\imath,\jmath}(k)$ stores the portion of TCAs in the corresponding state bin. In the infinite system limit, normalized $x_{\imath,\jmath}(k)$ can be regarded as the probability mass. In the rest of this chapter, we shall use the normalized fashion.

The system evolution depends on the system matrix $A(k)$. Each entry $A_{(p,q),(\imath,\jmath)}(k)$ depicts the portion or probability for the TCAs in bin $(\imath,\jmath)$ jumping to bin (p,q) during the kth time interval. Herein, population migration happens after the control action. For example, in $A_{(p,q),(\imath,\jmath)}(k)$, the starting state $(\imath,\jmath)$ is the one after the switching action, i.e., switching ON/OFF. Once switched, TCAs will migrate from the current state bin to the one with the same temperature but opposite ON/OFF status, i.e., $(\imath,\jmath) \to (N_i - \imath + 1, N_m - \jmath + 1)$. The TCA can either stay in the original state bin or migrate to other bins. However, since the starting state is the one after the control action, TCAs in OFF(ON) bins can only migrate among OFF(ON) bins. With the normalized description, the sum of all system states is 1, and consequently, the column sum of $A(k)$ must be 1 to ensure every TCA has a destination.

3.2.4 Derivations of System Matrix $A(k)$

In this Section, starting from the simplest case to the most complicated case, we will show the analytical derivations of $A(k)$. Herein, it is assumed that all TCAs have the same R_a and R_m, and their rated power are the same. All TCAs only differ at C_a and C_m, resulting in different a and b in (3.2). These assumptions are quite reasonable because on the one hand, it is rational to assume all houses are the same while with different TCAs; on the other hand, though all TCAs have the same temperature gain, the heterogeneity can be reserved by the probability distribution of the heat capacity. Since migration probabilities of T_i and T_m are independent, $A_{(p,q),(\imath,\jmath)}(k)$ can be expressed as

$$A_{(p,q),(\imath,\jmath)}(k) = \Pr_{(p,\star),(\imath,\jmath)}(k) \times \Pr_{(\star,q),(\imath,\jmath)}(k), \tag{3.4}$$

where $\underset{(p,\star),(\imath,\jmath)}{\Pr}(k)$ and $\underset{(\star,q),(\imath,\jmath)}{\Pr}(k)$ are the probabilities for TCAs in $(\imath,\jmath)$ migrating to $(p,\star)$ and TCAs in $(\imath,\jmath)$ migrating to $(\star,q)$, respectively. $\underset{(p,\star),(\imath,\jmath)}{\Pr}(k)$ and $\underset{(\star,q),(\imath,\jmath)}{\Pr}(k)$ will be illustrated separately.

3.2.4.1 $\underset{(p,\star),(\imath,\jmath)}{\Pr}(k)$ (Point, Point)-to-Point

We first investigate how to determine the parameter a when both of the starting and ending states are at specific points. Let $\zeta_i(k)$, $\zeta_i(k+1)$, $\zeta_m(k)$, and $\zeta_0(k)$ denote the starting indoor air temperature, ending indoor air temperature, starting building mass temperature, and ambient temperature, respectively. In addition, let $m_1 = \frac{R_a}{R_a+R_m}$ and $m_2 = \frac{R_m}{R_a+R_m}$. From (3.2) we have

$$\zeta_i(k+1) = a\zeta_i(k) + (1-a)(m_1\zeta_m(k) + m_2\zeta_0(k) + g(k)), \tag{3.5}$$

where

$$g(k) = \begin{cases} 0, & \text{OFF}, \\ m_2 R_a P, & \text{ON}. \end{cases}$$

With the full temperature information, the parameter a can be calculated as

$$a = \frac{\zeta_i(k+1) - m_1\zeta_m(k) - m_2\zeta_0(k) - g(k)}{\zeta_i(k) - m_1\zeta_m(k) - m_2\zeta_0(k) - g(k)}, \tag{3.6}$$

where $g(k)$ is determined by the status of the TCA after the control action. This indicates that any TCA with the parameter a calculated in (3.5) can migrate from $(\zeta_i(k), \zeta_m(k))$ to $(\zeta_i(k+1), \star)$ after one time step. The term denoted by $\star$ will be discussed later.

3.2.4.2 $\Pr\limits_{(p,\star),(\imath,\jmath)}(k)$ (Point, Point)-to-Range

Different from the last scenario, the ending indoor air temperature falls into a range: $\underline{\zeta}_i(k+1) \le \zeta_i(k+1) \le \overline{\zeta}_i(k+1)$, where $\underline{\zeta}_i(\star)$ and $\overline{\zeta}_i(\star)$ are the lower and upper bounds of a specific indoor air temperature state bin. Thus (3.6) becomes

$$\underline{a} \le a \le \overline{a}. \tag{3.7}$$

On the one hand,

$$\begin{aligned} \underline{a} &= \frac{\underline{\zeta}_i(k+1) - m_1\zeta_m(k) - m_2\zeta_0(k)}{\zeta_i(k) - m_1\zeta_m(k) - m_2\zeta_0(k)}, \\ \overline{a} &= \frac{\overline{\zeta}_i(k+1) - m_1\zeta_m(k) - m_2\zeta_0(k)}{\zeta_i(k) - m_1\zeta_m(k) - m_2\zeta_0(k)}, \end{aligned} \tag{3.8}$$

when the TCA is OFF. On the other hand,

$$\begin{aligned} \underline{a} &= \frac{\overline{\zeta}_i(k+1) - m_1\zeta_m(k) - m_2\zeta_0(k) - g(k)}{\zeta_i(k) - m_1\zeta_m(k) - m_2\zeta_0(k) - g(k)}, \\ \overline{a} &= \frac{\underline{\zeta}_i(k+1) - m_1\zeta_m(k) - m_2\zeta_0(k) - g(k)}{\zeta_i(k) - m_1\zeta_m(k) - m_2\zeta_0(k) - g(k)}, \end{aligned} \tag{3.9}$$

when the TCA is ON. The reason for swapping $\overline{\zeta}_i$ and $\underline{\zeta}_i$ in the numerators of $\underline{a}$ and $\overline{a}$ is because of the negative sign caused by $-g(k)$. Thus, the probability for a TCA migrating from $(\zeta_i(k), \zeta_m(k))$ to $([\underline{\zeta}_i(k+1), \overline{\zeta}_i(k+1)], \star)$ is

$$\Pr_{(p,\star),(\imath,\jmath)}(k) = \int\limits_{\underline{a}}^{\overline{a}} p(a)\mathrm{d}a, \tag{3.10}$$

where $p(a)$ is the probability density function of the distribution of a. Since all the TCAs only differ at C_a and C_m, the distribution of a is directly dependent on the distribution of C_a. As long as the distribution of C_a is determined, the probability density function $p(a)$ can be determined. In this chapter, we assume that a follows a uniform distribution according to a particular distribution of C_a. Other distributions may be discussed in the future work. Any calculated a outside the distribution $[a_l, a_u]$ is regarded as invalid, where a_l and a_u are the lower and upper bounds of the uniform distribution of a.

3.2.4.3 $\Pr\limits_{(p,\star),(\imath,\jmath)}(k)$ (Range, Point)-to-Range

In addition to the previous scenario, the starting indoor air temperature also varies within a range, denoted by $[\underline{\zeta}_i(k), \overline{\zeta}_i(k)]$. With a fixed $\zeta_i(k)$, the lower and upper bounds of the parameter a can be calculated by (3.8) or (3.9). However, the probability in (3.10) is evaluated as

$$\Pr_{(p,\star),(\imath,\jmath)}(k) = \int\limits_{\underline{\zeta}_i(k)}^{\overline{\zeta}_i(k)} p(\zeta_i(k)) \int\limits_{\underline{a}}^{\overline{a}} p(a)\mathrm{d}a\mathrm{d}\zeta_i(k), \tag{3.11}$$

where $p(\zeta_i(k))$ is the probability density function of the starting indoor air temperature. In [65], TCAs are assumed to be uniformly distributed in $[\underline{\zeta}_i(k), \overline{\zeta}_i(k)]$. However, there is no evidence showing which distribution is appropriate. The general form (3.11) is proposed in this chapter for any appropriate distribution. Thus, the probability for a TCA migrating from $([\underline{\zeta}_i(k), \overline{\zeta}_i(k)], \zeta_m(k))$ to $([\underline{\zeta}_i(k+1), \overline{\zeta}_i(k+1)], \star)$ can be calculated as in (3.11).

3.2.4.4 $\Pr\limits_{(p,\star),(\imath,\jmath)}(k)$ (Range, Range)-to-Range

In addition to the previous scenario, the starting building mass temperature also varies within a range, i.e., $\zeta_m(k) \in [\underline{\zeta}_m(k), \overline{\zeta}_m(k)]$, where $\underline{\zeta}_m(\star)$ and $\overline{\zeta}_m(\star)$ are the lower and upper bounds of a specific building mass temperature state bin. With $\zeta_i(k)$ and $\zeta_m(k)$ fixed, the lower and upper bounds of a can be obtained from (3.8) or (3.9).

However, the probability in (3.11) is evaluated as

$$\Pr_{(p,\star),(\imath,\jmath)}(k) = \int\limits_{\underline{\zeta}_m(k)}^{\overline{\zeta}_m(k)} p(\zeta_m(k)) \int\limits_{\underline{\zeta}_i(k)}^{\overline{\zeta}_i(k)} p(\zeta_i(k)) \int\limits_{\underline{a}}^{\overline{a}} p(a)\mathrm{d}a\mathrm{d}\zeta_i(k)\mathrm{d}\zeta_m(k), \tag{3.12}$$

where $p(\zeta_m(k))$ is the probability density function of the starting building mass temperature. Thus, the probability for a TCA migrating from $([\underline{\zeta}_i(k), \overline{\zeta}_i(k)], [\underline{\zeta}_m(k), \overline{\zeta}_m(k)])$ to $([\underline{\zeta}_i(k+1), \overline{\zeta}_i(k+1)], \star)$ can be calculated as in (3.12).

3.2.4.5 $\Pr_{(\star,q),(\imath,\jmath)}(k)$ (Range, Range)-to-Range

It can be noticed from (3.2) that the dynamics of T_i and T_m are similar, which results in a similar way of calculating the migration probabilities regarding parameter b. However, determining the integral upper and lower bounds is not straightforward. First we take the (point, point)-to-point case as an example to show the difficulty. Let $\zeta_i(k)$, $\zeta_m(k)$, and $\zeta_m(k+1)$ denote the starting indoor air temperature, starting building mass temperature, and ending building mass temperature, respectively. Then, according to (3.2), b can be calculated as

$$b = \frac{\zeta_m(k+1) - \zeta_i(k)}{\zeta_m(k) - \zeta_i(k)}. \tag{3.13}$$

This indicates that any TCA with b in (3.13) and starting temperature $\zeta_i(k)$ and $\zeta_m(k)$ will jump to $\zeta_m(k+1)$ after one time step. It is worth emphasizing that the distribution of b only depends on the distribution of C_m. Same as parameter a, the parameter b is also assumed to be uniformly distributed in $[b_l, b_u]$ according to a particular distribution of C_m, where b_l and b_u are the lower and upper bounds of the distribution of b. Any calculated b outside this range is invalid, which results in an impossible probability. Now, in the case of (range, range)-to-range, different from the calculation of parameter a, signs of numerator and denominator in (3.13) become uncertain even with two temperature fixed, because T_i and T_m are close to each other. Fortunately, the function in (3.13) is monotonous with any one temperature fixed, thus, the upper and lower bounds of b can be determined as

$$\begin{aligned} \bar{b} &= \max\left\{b_l, \min\left\{b_u, \max\left\{\overline{\theta}_m, 0, \underline{\theta}_m\right\}\right\}\right\}, \\ \underline{b} &= \min\left\{b_u, \max\left\{b_l, \min\left\{\max\left\{\overline{\theta}_m, 0\right\}, \max\left\{\underline{\theta}_m, 0\right\}\right\}\right\}\right\}, \end{aligned} \tag{3.14}$$

where

$$\begin{aligned} \overline{\theta}_m &= \frac{\overline{\zeta}_m(k+1) - \zeta_i(k)}{\zeta_m(k) - \zeta_i(k)}, \\ \underline{\theta}_m &= \frac{\underline{\zeta}_m(k+1) - \zeta_i(k)}{\zeta_m(k) - \zeta_i(k)}. \end{aligned} \tag{3.15}$$

Hence, the probability for TCAs migrating from $([\underline{\zeta}_i(k), \overline{\zeta}_i(k)], [\underline{\zeta}_m(k), \overline{\zeta}_m(k)])$ to $(\star, [\underline{\zeta}_m(k+1), \overline{\zeta}_m(k+1)])$ is calculated as

$$\Pr_{(\star,q),(\imath,\jmath)}(k) = \int\limits_{\underline{\zeta}_m(k)}^{\overline{\zeta}_m(k)} p(\zeta_m(k)) \int\limits_{\underline{\zeta}_i(k)}^{\overline{\zeta}_i(k)} p(\zeta_i(k)) \int\limits_{\underline{b}}^{\bar{b}} p(b) \mathrm{d}b \mathrm{d}\zeta_i(k) \mathrm{d}\zeta_m(k), \tag{3.16}$$

where $p(b)$ is the probability density function of parameter b. Consequently, the probability for TCAs migrating from $([\underline{\zeta}_i(k), \overline{\zeta}_i(k)], [\underline{\zeta}_m(k), \overline{\zeta}_m(k)])$ to $([\underline{\zeta}_i(k+1), \overline{\zeta}_i(k+1)], [\underline{\zeta}_m(k+1), \overline{\zeta}_m(k+1)])$ can be computed by (3.4).

From the above derivations, it can be observed that elements in $A(k)$ depend on the ambient temperature. This is to say, though the ambient temperature can be treated as a constant within a narrow time span, we still have different $A(k)$ in different time intervals. In [65], the system matrix is chosen as a constant which cannot fully characterize the practical situation. Further, the hidden Markov transition matrix estimation method used in [65] cannot be directly adopted for the time-varying $A(k)$ because of the online computational load. Compared to the estimation method, the proposed analytical derivation of $A(k)$ can be immediately completed and ready for following processes. In addition, within a small range of ambient temperature, the transition matrix can be regarded as a constant. Thus, the ambient temperature can be partitioned into several small pieces and it is possible to make a lookup table to include all transition matrices according to different ambient temperature ranges. By doing so, the offline calculated transition matrices can be directly used in the online optimization without any online calculation.

3.2.5 Other System Matrices and The Control Signal

The input matrix $B(k)$ in (3.3) is also time-varying, which is represented as

$$B(k) = A(k)B, \tag{3.17}$$

where

$$B = \begin{bmatrix} -\mathbf{I}_{N_iN_m/4} \\ \mathbf{E}_{N_iN_m/4} \end{bmatrix}, \tag{3.18}$$

where $\mathbf{I}_{N_iN_m/4}$ and $\mathbf{E}_{N_iN_m/4}$ are the identity and reverse identity matrices with the dimension of $N_iN_m/4$. By defining $B(k)$ as in (3.17), we can guarantee that all TCA population migrations happen after the control actions. In addition, this B matrix can guarantee the sum 1 of the system state $x(k)$.

The control signal is defined as $u(k) \in \mathbb{R}^{\frac{N_iN_m}{4}}$, in which each element represents the absolute percentage of TCAs in a certain (T_i, T_m) that needs to be switched. Each switched TCA will be added to the opposite ON/OFF status state bin with (T_i, T_m) unchanged. Since the order of the elements in $x(k)$ is from OFF to ON, thus, positive elements in $u(k)$ represent the switching-ON actions while negative elements represent the switching-OFF actions.

Since the design objective is to provide ancillary services, i.e., to use the aggregated power consumption of TCAs to track the desired trajectory, the output matrix C is a simple aggregation vector which is defined as

$$C = Pm[\underbrace{0\ 0\ \cdots\ 0}_{N_i N_m/4}\ \underbrace{1\ 1\ \cdots\ 1}_{N_i N_m/4}] \in \mathbb{R}^{\frac{N_i N_m}{2}}, \tag{3.19}$$

where m is the total number of TCAs. The input-to-output matrix is defined as

$$D = CB. \tag{3.20}$$

3.3 Controller Design

In this Section, a centralized MPC scheme for theoretically controlling the switching portions is investigated. Once obtaining the control signal, it is necessary to determine which TCA needs to be switched or stay in the current status.

3.3.1 Centralized MPC Scheme

3.3.1.1 System Dynamics

The system state is defined in Section 3.2.3. Let N denote the prediction horizon, then the state prediction vector is defined as

$$\mathcal{X}(k) = \begin{bmatrix} x(k|k) \\ x(k+1|k) \\ \vdots \\ x(k+N-1|k) \end{bmatrix} \in \mathbb{R}^{\frac{N_i N_m N}{2}}, \tag{3.21}$$

where $x(k+\ell|k)$ is the predicted state at time $k+\ell$ with the knowledge of the state at time k. The control sequence, containing control signals from time k to time $k+N-1$, is defined as

$$\mathcal{U}(k) = \begin{bmatrix} u(k|k) \\ u(k+1|k) \\ \vdots \\ u(k+N-1|k) \end{bmatrix} \in \mathbb{R}^{\frac{N_i N_m N}{4}}. \tag{3.22}$$

Then the system dynamics in (3.3) can be represented in an MPC fashion as

$$\mathcal{X}(k) = \mathcal{M}(k)x(k|k) + \mathcal{C}(k)\mathcal{U}(k), \tag{3.23}$$

where

$$\begin{aligned} \mathcal{M}(k) &= \begin{bmatrix} \mathbf{I} \\ A(k) \\ A(k+1)A(k) \\ \vdots \\ A(k+N-2)\cdots A(k) \end{bmatrix}, \\ \mathcal{C}(k) &= \begin{bmatrix} \mathbf{0} & & & & \\ B(k) & \mathbf{0} & & & \\ A(k+1)B(k) & B(k+1) & \mathbf{0} & & \\ \vdots & \vdots & \ddots & \ddots & \\ A(k+N-2)\cdots A(k+1)B(k) & \cdots & \cdots & B(k+N-2) & \mathbf{0} \end{bmatrix}. \end{aligned} \tag{3.24}$$

Herein, $A(k+1)$, $\ldots$, $A(k+N-2)$ can be calculated by using the forecasted ambient temperature. In this chapter, it is assumed that the ambient temperature can be accurately forecasted. Control design considering the forecasting error will be studied in the future work.

3.3.1.2 Objective Function

The main control objective is to use the aggregated TCAs' power consumption to track the desired trajectory. Thus, the objective function aims to minimize the normed error between the aggregated power consumption and the desired trajectory along the prediction horizon. As a result, the objective function at time instant k can be expressed as

$$\begin{aligned}\mathcal{J}_m(k) &= \sqrt{\sum_{\ell=0}^{N-1} \left[(y(k+\ell|k) - z(k+\ell))^\mathsf{T}(y(k+\ell|k) - z(k+\ell))\right]} \\ &= \|\mathcal{C}\mathcal{X}(k) + \mathcal{D}\mathcal{U}(k) - \mathcal{Z}(k)\|,\end{aligned} \tag{3.25}$$

where $z(k+\ell)$ is the value of the desired trajectory at time $k+\ell$, $\mathcal{Z}(k) = [z(k) \ \cdots \ z(k+N-1)]^\mathsf{T}$, and

$$\mathcal{C} = \operatorname{diag}\{C\} = \begin{bmatrix} C & & \\ & \ddots & \\ & & C \end{bmatrix}, \mathcal{D} = \operatorname{diag}\{D\} = \begin{bmatrix} D & & \\ & \ddots & \\ & & D \end{bmatrix}.$$

By substituting (3.23) into (3.25), we have

$$\mathcal{J}_m(k) = \|\,(\mathcal{C}\mathcal{C}(k) + \mathcal{D})\,\mathcal{U}(k) - (\mathcal{Z}(k) - \mathcal{C}\mathcal{M}(k)x(k|k))\,\|. \tag{3.26}$$

3.3.1.3 Constraints

One of the advantages of the MPC scheme is that it can incorporate both state and input constraints into the control design. Since the system states represent the percentages in certain state bins, these percentages must be between 0 and 1. Thus, we have the state constraint expressed as

$$\mathbf{0} \leq \mathcal{M}(k)x(k|k) + \mathcal{C}(k)\mathcal{U}(k) \leq \mathbf{1}, \tag{3.27}$$

where $\mathbf{0}$ and $\mathbf{1}$ represent for all-0 and all-1 vectors with appropriate dimensions, respectively. Further, since the constraint on the sum of $x(k+\ell|k)$ equaling 1 can be automatically satisfied by using the well-defined $A(k)$ and $B(k)$, there is no need to include this constraint in the optimization.

The constraint for the control signal is on the property of the portion. Each element $u(k+\ell|k)$ in $\mathcal{U}(k)$ represents switching a portion of the TCAs ON or OFF in a certain temperature combination. Both positive and negative values can $u(k+\ell|k)$ go, however, none of the elements can exceed the range of $[-1, 1]$, i.e.,

$$-\mathbf{1} \leq \mathcal{U}(k) \leq \mathbf{1}. \tag{3.28}$$

To this end, Eqn. (3.27) is used to constrain the system states after the evolution, while (3.28) is to constrain each control signal. However, the combination of (3.27) and (3.28) is still too weak to constrain the system states after the control action yet before the evolution. In other words, we have to guarantee that, after the control action, the predicted state bin percentage is within the range of $[0, 1]$. Hence we have

$$\mathbf{0} \leq x(k+\ell|k) + B(k+\ell)u(k+\ell|k) \leq \mathbf{1},\ \forall \ell = 0, \cdots, N-1. \tag{3.29}$$

By implementing constraint (3.29), the controller will never attempt to switch a number of TCAs more than the available population in each bin. Since (3.29) is tighter than (3.28), (3.28) can be discarded.

To summarize, the optimal control sequence from time k to $k+N-1$ can be obtained by solving the following convex optimization problem

$$\begin{aligned} &\min_{\mathcal{U}(k)} \ \mathcal{J}_m(k), \\ &\text{s.t. (3.27) and (3.29).} \end{aligned} \tag{3.30}$$

In each step, we only choose the first element $u^*(k|k)$ in the optimal $\mathcal{U}^*(k)$ as the current control signal.

3.3.2 Control Signal Implementation

Once obtaining the optimal control signal $u^*(k|k)$, the controller has to decide which TCA needs to follow the signal. This is of significant importance since not all of the TCAs in a certain state bin need to change their running status. The steps to execute the control signals can be detailed as follows.

STEP 1 Obtain the optimal control signal $u^*(k|k)$.

STEP 2 Each TCA provides its state bin location and the switching availability which is based on the lockout time.

STEP 3 Regardless of the control signal, TCAs that are outside the indoor air temperature bounds and not locked are forced to switch. The number of this type of switchings falls into the lowest(highest) $N_m/2$ bins according to their building mass temperature. TCAs that are outside the indoor air temperature bounds but locked need to be immediately switched after the lockout effect.

STEP 4 By Considering the lockout time, designate a certain number of TCAs to switch according to the control signal.

Remark 3.1: Since, in the proposed MPC scheme, the temperature of each end-user is not directly controlled, it is possible for end-users to exceed the temperature bounds.

This is one of the drawbacks of the proposed control protocol. The significance of **STEP 3** is to steer the indoor air temperature back to the comfortable range as soon as possible. In the later simulations, we can also notice these flaws. However, this problem can be easily solved by slightly shrinking the width of the required comfortable range. ■

Remark 3.2: In **STEP 4**, it is possible to have three cases. First, the number of forced switched TCAs plus the number of normally switched TCAs (ones within the comfort range) is equal to the calculated number of switchings. Second, the number of forced switched TCAs already exceeds the calculated number of switchings. Third, the number of forced switched TCAs plus the number of normally switched TCAs is less than the calculated number of switchings (this happens because of the lockout effect). Except for the first case, the other two cases will definitely result in the deviation between the aggregated power output and the desired trajectory. The second case can be resolved by including another objective function to push TCAs to the center of the temperature ranges. However, we will encounter a trade-off between the control signal matching and the tracking performance. This will be discussed in Section 3.4. The third case can be neutralized by giving the TCAs that are already out of and far away from the lockout time the priority to change their status. ■

3.4 Case Study

3.4.1 Parameter Selection

The winter ambient temperature in this simulation is collected from the meteorological station located in Victoria, B.C., Canada. The number of TCAs is chosen as 1000. R_a and R_m are selected to be 0.047°C/W and 0.02°C/W, respectively. C_a follows a specific distribution within $[5000, 8000]\mathrm{J}/^{\circ}\mathrm{C}$ with the probability density function

$$p(C_a) = \begin{cases} \frac{1}{a_u - a_l} e^{-\frac{R_a + R_m}{R_a R_m C_a}\Delta t} \frac{R_a + R_m}{R_a R_m C_a^2}\Delta t, & 5000 \leq C_a \leq 8000, \\ 0, & \text{else;} \end{cases} \tag{3.31}$$

C_m follows a specific distribution within $[5800, 9000]\mathrm{J}/^{\circ}\mathrm{C}$ with the probability density function

$$p(C_m) = \begin{cases} \frac{1}{b_u - b_l} e^{-\frac{1}{R_m C_m}\Delta t} \frac{1}{R_m C_m^2}\Delta t, & 5800 \leq C_a \leq 9000, \\ 0, & \text{else.} \end{cases} \tag{3.32}$$

Consequently, a and b are uniformly distributed. The rated power for all TCAs is 7 kW. N_i and N_m are both selected to be 20. The deadbands for both of the air and building mass temperature are $21 \pm 2^{\circ}\mathrm{C}$. In addition, the probability density functions $p(\zeta_i(k))$ and $p(\zeta_m(k))$ are assumed to follow the uniform distribution.

3.4.2 Desired Trajectory Construction

The ancillary service we choose to show in this chapter is primary frequency control, which is to use the aggregated power consumption to compensate for the fluctuation in the power supply. The desired trajectory P_d of a group of TCAs is dependent on the baseline power consumption P_B. The TCA group needs to provide its P_B to the grid so that the deviations from P_B can be utilized to provide the regulation service. The baseline power consumption for the next day is constructed by letting all TCAs run in a temperature setpoint tracking mode using the day-ahead ambient temperature forecast. This means that the baseline power consumption is only used to drive the indoor air temperature to track the most comfortable temperature. In the population-based model, it is to restrain all the TCAs in the center of the bins.

The test regulation signal is taken from the PJM website [99]. The magnitude of the test signal is adjusted for 1000 TCAs to have a 0.5 MW regulation capacity.

3.4.3 System Performance and Analyses

The indoor air temperature of 1000 TCAs is initialized to be normally distributed in $[21.4, 21.8]$°C, and the building mass temperature is set at 21°C, which is in the center of the state bins. By adopting the proposed control protocol, the indoor air temperature and building mass temperature together with the ambient temperature of 1000 TCAs within a day can be shown in Figure 3.2. During the one-day service, indoor air temperature of all TCAs evolves within the preset deadband, i.e., 19°C to 23°C. The building mass temperature also varies within $[19, 23]$°C, but relatively slowly because of the high heat capacity.

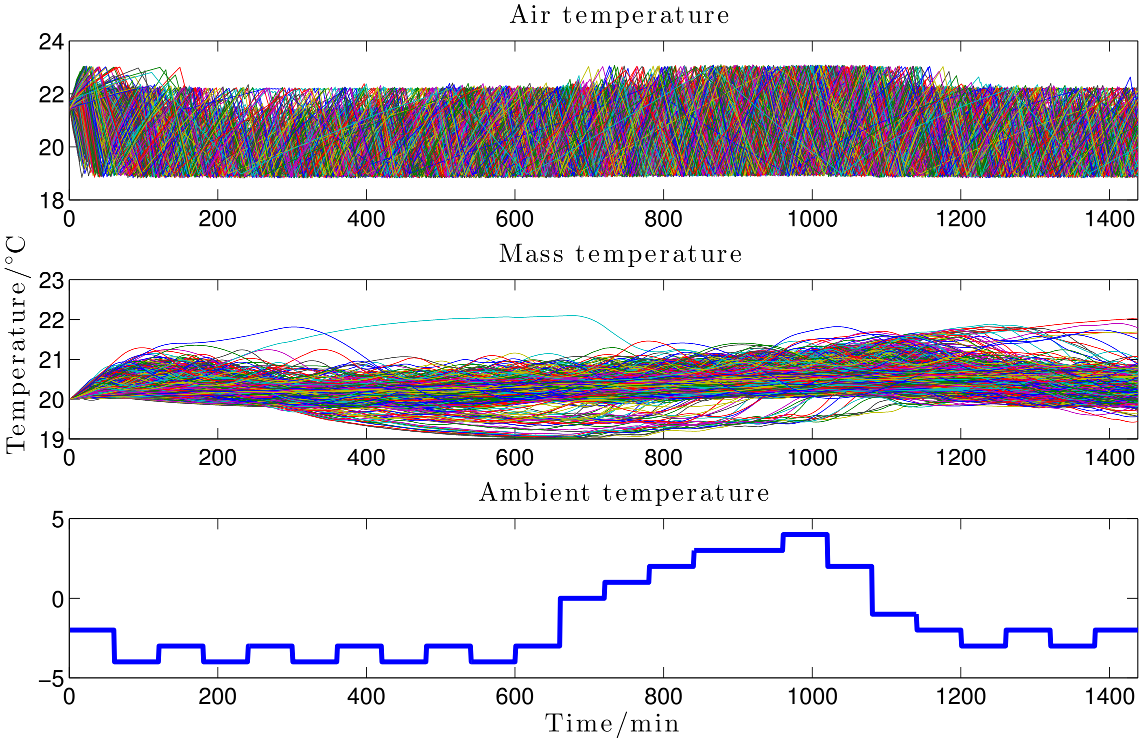

Figure 3.2: Indoor air temperature, building mass temperature, and ambient temperature.

The desired trajectory P_d of 1000 TCAs can be found in Figure 3.3. By utilizing the proposed control protocol, the tracking performance can be clearly observed from Figure 3.3. The error between two trajectories can be seen in Figure 3.4, in which

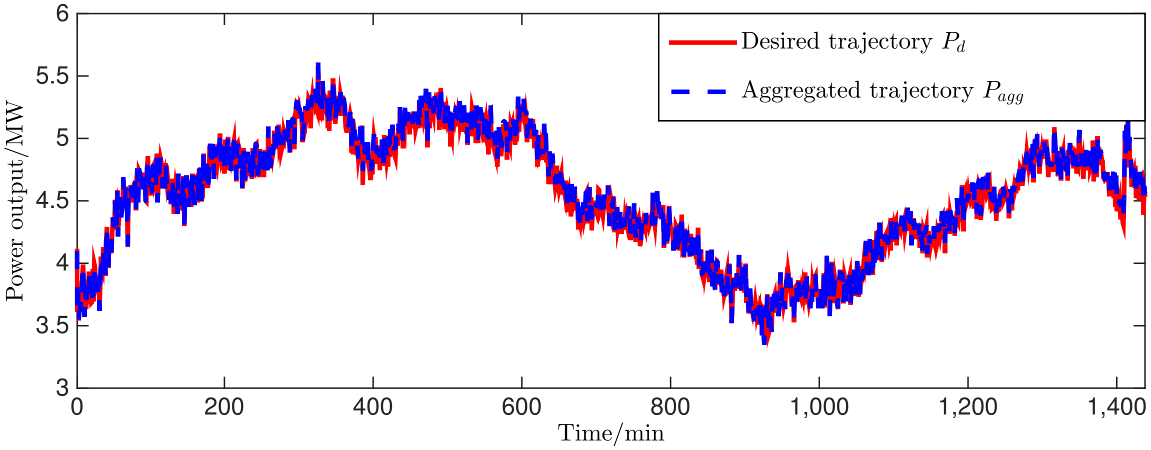

Figure 3.3: Comparison of the desired trajectory and the aggregated power consumption under the proposed control protocol.

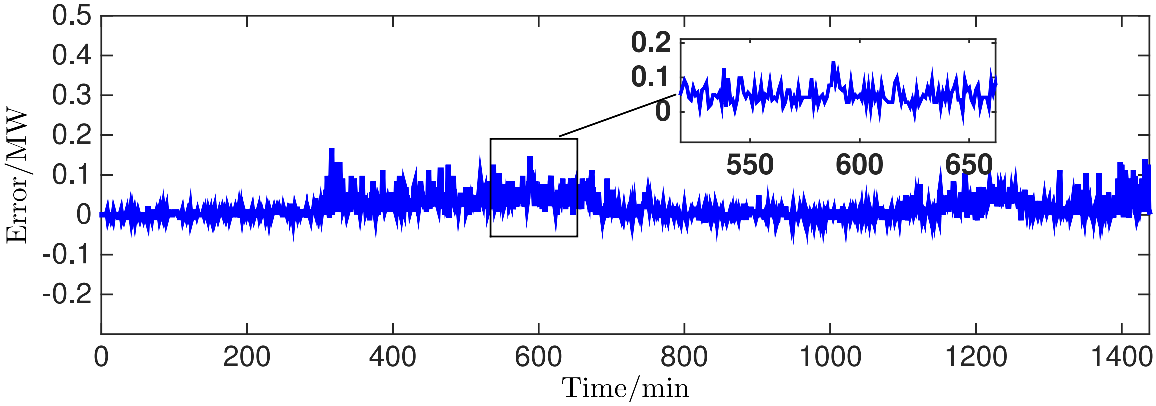

Figure 3.4: The desired trajectory tracking error.

the maximum error is less than 0.15 MW. If we include the normed error

$$\epsilon = \frac{\|P_d - P_{agg}\|}{\|P_d\|}, \tag{3.33}$$

then ϵ for these 1000 TCAs within one day is only 0.73%. From Figure 3.4, we can tell that most of the errors occur when the ambient temperature is relatively low, and the aggregated power consumption is slightly higher than the desired trajectory. This is because when the ambient temperature is lower, the TCAs will more likely go below the T_i lower bound, and consequently, unlocked TCAs among them are forced to switch ON according to **STEP 3**.

As mentioned in the control signal implementation steps, the actual switching actions are usually different from the calculated optimal switching actions. The comparisons between the calculated one and the actual one can be seen in Figure 3.5. The upper plot shows the total number of switched TCAs, including switching ON and OFF. It can be readily observed that, though the cases in **Remark 3.2** exist, the actual total number of switchings can match the calculated one very well. In addition, as shown in the lower plot, most errors between them are less than 10, which is acceptable.

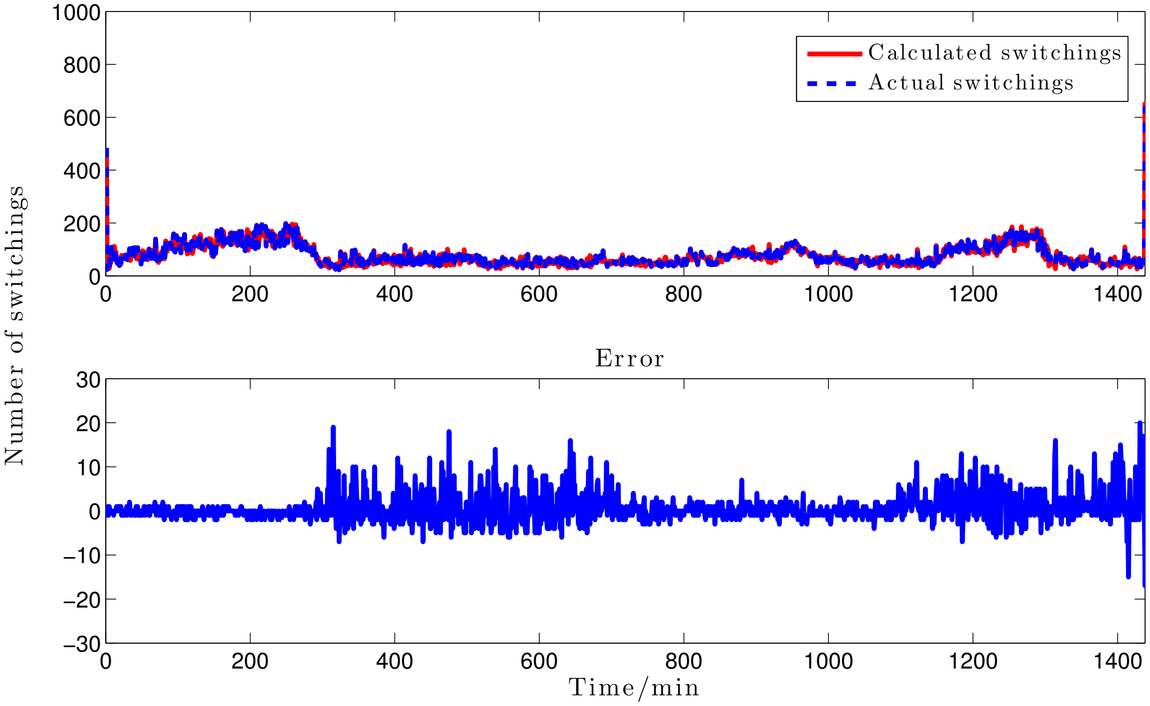

Figure 3.5: Comparisons between the actual and calculated switchings.

The above figures and numerical results sufficiently verify the feasibility of the proposed control approach. Comprehensive simulation studies under different parameter setups have also been conducted to compare the control performance in different cases. The simulation figures are omitted in this chapter, but some observations and analyses are summarize as below:

- For the test regulation signals with different magnitudes but the same frequency, the number of TCAs will definitely affect the tracking performance [50], because the adjusting room shrinks as the number of TCAs drops. A simulation with 100 TCAs was conducted to compare with the 1000 TCAs case. The magnitude of the test regulation signal is adjusted accordingly for the 100 TCAs, while with the same varying frequency. The normed error for the 100 TCAs case is around 1.8%, which is almost three times than the 1000 TCA case. Thus, in order to achieve a better service quality, larger participation is preferred.

- The prediction horizon N plays an important role in obtaining the control signal. Theoretically, the longer N is, the better control signal will be. However, as N is enlarged, the problem size becomes even larger. The problem size of the optimization problem in (3.30) in this simulation is $N_i N_m N/2 = 500$ and the time elapsed for one round optimization is around 0.56 second. As N increases to 60, the normed error is reduced to 0.728%, but the time elapsed increases to 4.16 seconds. If N is decreased to 3, the normed error increases to 1.3%, but the time elapsed decreases to 0.2 second. For $N = 60$ case, the performance is slightly improved, but it takes too long to achieve the primary frequency control; for the $N = 3$ case, the primary frequency control can be guaranteed however the error is not acceptable. In practical applications, it is not necessary to have a slightly decreased norm error while sacrificing the real-time control. Thus, with an acceptable error, which is below 1%, the prediction horizon can be properly decreased.

- The number of state bins also affects the service performance. Note that the prediction horizon affects the control performance, whereas the number of state bins affects the modeling accuracy. With less state bins, the temperature span for each state bin becomes larger, resulting in an inaccurate classification; with more state bins, the temperature span for each state bin becomes too narrow to involve reasonable number of TCAs and the calculation of probabilities in $A(k)$ may cause computational error. In addition, same as the prediction horizon, larger number of state bins will increase the problem size. In one of the conducted simulations, the number of state bins versus tracking normed error is a U-shape curve whose minimum value is at around $10 - 20$. After 20, the normed error increases exponentially.

- If we prefer a full autonomous system than forcing the out-of-boundary TCAs to switch their status, it is possible to add another objective function to $\mathcal{J}_m(k)$ in (3.26) to push all TCAs to the center of the state bins as much as possible. This objective function $\mathcal{J}_s(k)$ can be constructed as

$$\mathcal{J}_s(k) = \| \mathcal{Q}\mathcal{X}(k)\|, \tag{3.34}$$

where $\mathcal{Q}$ is the weighting matrix having two functions: 1) to balance $\mathcal{J}_s(k)$ and $\mathcal{J}_m(k)$; 2) to steer TCAs to the center of the state bins. The structure of $\mathcal{Q}$ can be

$$\mathcal{Q} = \mathrm{diag}\{Q\} \in \mathbb{R}^{\frac{N_i N_m N}{2} \times \frac{N_i N_m N}{2}}, \tag{3.35}$$

where

$$Q = \begin{bmatrix} \underbrace{\mathrm{diag}\{q\}}_{\frac{N_m}{2}\times\frac{N_m}{2}} & & \\ & \underbrace{\mathrm{diag}\{0.1q\}}_{\left(\frac{N_i}{2}-2\right)\frac{N_m}{2}\times\left(\frac{N_i}{2}-2\right)\frac{N_m}{2}} & \\ & & \underbrace{\mathrm{diag}\{q\}}_{\frac{N_m}{2}\times\frac{N_m}{2}} \end{bmatrix}, \tag{3.36}$$

in which q is a scalar to achieve the first function. Thus, the optimization problem in (3.30) becomes

$$\begin{aligned} &\min_{\mathcal{U}(k)} \ \mathcal{J}_m(k) + \mathcal{J}_s(k), \\ &\text{ s.t. (3.27) and (3.29).} \end{aligned} \tag{3.37}$$

However, $\mathcal{J}_s(k)$ is such a strong constraint for the control performance since some of TCAs will lose their flexibility to contribute to the tracking service. The normed tracking error with $\mathcal{J}_s(k)$ involved is around 3.3%, where q is set to be 1. Hence, we would rather sacrifice a little bit comfort than compromise the tracking performance. Alternatively, it is possible to choose the method mentioned in **STEP 3** to achieve a certain comfort level.

3.5 Conclusion

In this chapter, a 2-D population-based model is proposed to describe the dynamics of aggregated 2nd-order TCAs. Both indoor air temperature and building mass temperature are considered in this model. Individual TCA dynamic evolutions are converted into population migration probabilities. Detailed analytical derivations of the time-varying population migration probability matrix are provided. A centralized MPC design based on the proposed aggregation model is investigated. In addition, considering practical situations, an implementation procedure of the control signal is studied. In the case study, it is shown that, with fine-tuned controller parameters, the aggregated power consumption of TCAs can track the desired trajectory with small deviations and the comfort level of end-users can be well maintained.

Chapter 4

Lockout-Induced Population-Based Aggregation Model and Control of Aggregated Heterogeneous TCAs

4.1 Introduction

4.1.1 Background and Literature Review

In Section 3.1, popular results on population-based models have been well surveyed. The case studies also show a promising DR service performance. However, similar as the results in the literature, some key and realistic issues have not been fully studied. One of them is on considering the TCA lockout time which is set by the manufacturer to avoid short cycling. In [69], the lockout time was considered when implementing the control signals, which will definitely cause a mismatch between the nominal calculated and actually implemented control signals. In [51,100], the authors only considered the minimum OFF time. In that design, control signals broadcasted to all TCAs are switching probabilities, and the local controller of each TCA needs to determine the switching action according to this probability. In Chapter 3, an improved 2-D population-based model in which control signals broadcasted to TCAs are deterministic, is proposed; however, the lockout effect is considered during the control implementation. Hence, it is urged to study a probabilistic population-based model which has lockout time explicitly formulated and can handle deterministic control signals.

Apart from the modeling, different control approaches and implementation methods were designed for different models. In [65], a centralized MPC scheme is proposed, however the regulation flexibility associated with the state distribution and lockout time are not studied. Authors in [51] adopted an inverse controller for the proposed 2-D population-based model. Hao *et al.* [52] designed a centralized priority stack controller for the proposed battery model. The controller possesses the characteristic of feedback, and it is also robust against disturbances. As mentioned in previous chapters, among all different types of control schemes, MPC shows its success in many industrial applications for numerous technical constraints can be included in the controller design. Particularly, DMPC possesses the merit of low computational load, which is a key feature for the fast regulation service [101–103]. Thus, in this chapter, a DMPC scheme shall be firstly investigated for aggregating a large population of TCAs to provide primary frequency control. One step further to the practicability, since the regulation signal is usually hard to predict, predictive controllers which require predictions may not be implementable in practical applications. Thus in the second technical part, in order to achieve an optimal control performance by considering the prediction issue, we shall develop an optimal controller which possesses a similar feature as MPC but requires no information of future regulation signals.

4.1.2 Research Objectives and Contributions

Motivated by the aforementioned points, the objectives and contributions of this chapter can be summarized as follows.

- The conventional population-based model is improved by including more state bins containing the uncontrollable locked TCAs. Time-varying system matrices are analytically derived.
- The switching probability is inherently described in the population-based model. Thus, instead of receiving a switching probability, each TCA follows a deterministic control signal.
- A DMPC scheme is developed for the improved population-based model. The developed control algorithm can dramatically reduce the computational load and guarantee the real-time control for primary frequency control.
- A flexibility penalty is proposed and added to the DMPC objective function. This penalty can effectively guarantee the match between the nominal and actual control signals, thus ensuring the service quality.
- An optimal control scheme is proposed to avoid the usage of the predictions of the regulation signals in the case that predictions are not available.
- In the optimal controller, a novel term, namely regulation capacity, is proposed and incorporated into the objective function. By introducing this term, the optimal control scheme can have a comparable control performance as the predictive control scheme, however, without any requirements on the reference signal predictions and is of high computational efficiency.

4.1.3 Chapter Organization

This chapter is organized as follows. Section 4.2 details the problem formulation and derivations of the lockout-induced population-based aggregation model. DMPC scheme is investigated in Section 4.3. Section 4.4 deals with the optimal controller design. This chapter is concluded in Section 4.5.

4.2 Aggregation Model Development

4.2.1 Lockout-Induced Population-Based Model

In the chapter, we continue to use the 1st-order ETP model as in (2.1). To make the derivations clear, the dynamics are recapped as

$$T_i(k+1) = aT_i(k) + (1-a)\left(T_o(k) + RQ(k)\right), \tag{4.1}$$

where

$$a = e^{-\frac{1}{RC}\Delta t}. \tag{4.2}$$

In conventional population-based models, all connected TCAs are partitioned into groups according to their temperature information and running status only, thus the lockout time can only be considered when implementing the control signal. As illustrated in Figure 4.1, in this chapter, in order to consider the locked TCAs inherently in the control design, TCAs are further partitioned into groups according to their lockout depths.

In this model, it is assumed and modelled that all evolutions happen after the control(switching) actions, which implies that only the control actions can switch the ON/OFF status, otherwise, TCAs in OFF(ON) bins cannot automatically migrate to

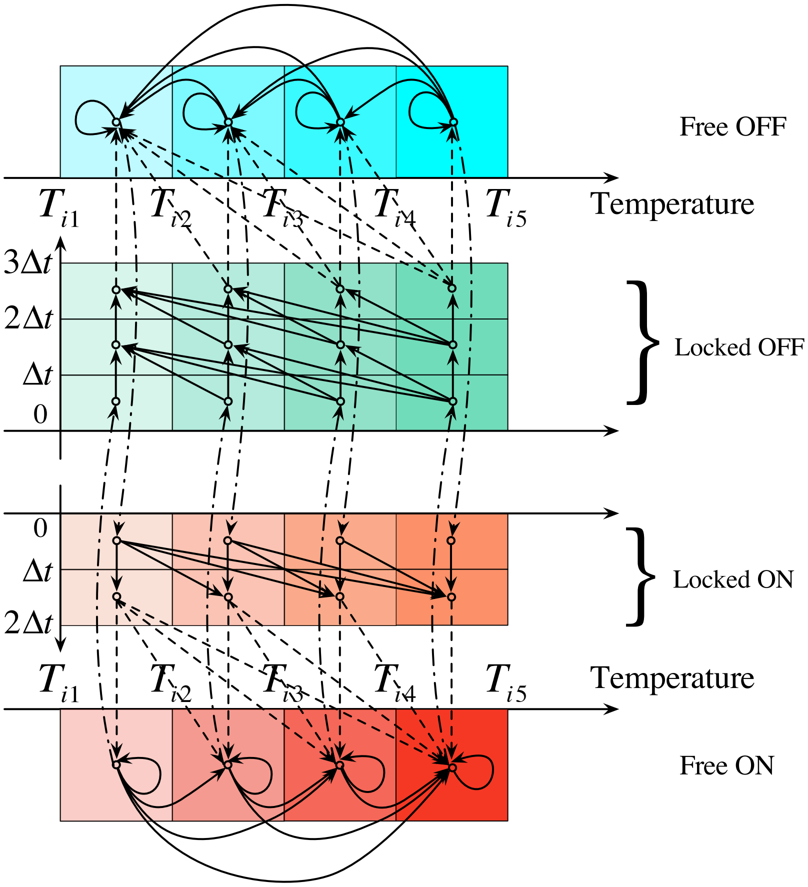

Figure 4.1: Population migration by adding lockout bins.

ON(OFF) bins. In Figure 4.1, dot dashed lines represent the switchings. In addition, every time when a TCA is switched from ON(OFF) to OFF(ON), it has to stay in the OFF(ON) status for at least $3\Delta t(2\Delta t)$ as in Figure 4.1, to maintain a certain duty cycle. To deal with different lockout status, locked TCAs are partitioned into groups according to the lockout depth. TCAs in shallow lockout status can only migrate to bins in the next lockout depth. TCAs in the deepest lockout status can migrate to the free bins which are controllable. Herein, each state value stands for the fraction of the load population in a specific temperature range, lockout depth, and ON/OFF status. Consequently, the system state $\mathscr{X}(k) \in \mathbb{R}^{\frac{N_i}{2}(2+N_1+N_0)}$ can be defined as

$$\mathscr{X}(k) = \left[\mathbf{x}_{\ell_1,\mathrm{off}}(k)^\mathsf{T} \cdots \mathbf{x}_{\ell_{N_0},\mathrm{off}}(k)^\mathsf{T} \; \mathbf{x}_{\ell_F,\mathrm{off}}(k)^\mathsf{T} \; \mathbf{x}_{\ell_1,\mathrm{on}}(k)^\mathsf{T} \cdots \mathbf{x}_{\ell_{N_1},\mathrm{on}}(k)^\mathsf{T} \; \mathbf{x}_{\ell_F,\mathrm{on}}(k)^\mathsf{T}\right]^\mathsf{T}, \tag{4.3}$$

where each vector contained in $\mathscr{X}(k)$ can be represented by $\mathbf{x}_{\ell,\jmath}(k)$ with

$$\ell = \begin{cases} 0 & \text{if FREE,} \\ k & \text{if in } \ell_k \text{ lockout depth,} \end{cases}$$

$$\jmath = \begin{cases} 0 & \text{if OFF,} \\ 1 & \text{if ON.} \end{cases}$$

Herein, the acceptable indoor temperature is equally partitioned into $N_i/2$ bins, the lockout depth for ON(OFF) status is $N_1(N_0)$. To make the derivations clear, in the rest of this chapter, we shall use n to denote $\frac{N_i}{2}(N_1 + N_0 + 2)$.

The upper part of $\mathscr{X}(k)$ represents all bins in OFF status and we have

$$\mathbf{x}_{\ell,\jmath}(k) = [x_{1,\ell,0}(k) \;\; \cdots \;\; x_{\frac{N_i}{2},\ell,0}(k)]^\mathsf{T}, \tag{4.4}$$

and for all bins in ON status, we have

$$\mathbf{x}_{\ell,\jmath}(k) = [x_{\frac{N_i}{2},\ell,1}(k) \;\; \cdots \;\; x_{1,\ell,1}(k)]^\mathsf{T}. \tag{4.5}$$

In (4.4) and (4.5), the first subscription of $x_{\imath,\ell,\jmath}(k)$ represents the temperature range, i.e., larger value represents higher temperature range, and *vice versa*. Please note that, the orders of elements in terms of temperature in OFF status and ON status are swapped for the sake of latter manipulations.

In a state-space form, population migrations among bins can be depicted as

$$\mathscr{X}(k+1) = \mathscr{A}(k)\mathscr{X}(k) + \mathscr{B}(k)\mathscr{U}(k), \tag{4.6}$$

where $\mathscr{A}(k)$ is the system transition matrix, $\mathscr{B}(k)$ is the input matrix, and $\mathscr{U}(k)$ is the control vector. This is a time-varying system and the associated matrices shall be defined in the following sections.

4.2.2 Control Vector $\mathscr{U}(k)$

The control vector $\mathscr{U}(k)$ contains the absolute portion of TCAs in free OFF(ON) bins that needs to be switched. Thus, $\mathscr{U}(k)$ is defined as

$$\begin{aligned} \mathscr{U}(k) &= [u_{1,0,0}(k) \ \cdots \ u_{\frac{N_i}{2},0,0}(k) \ u_{\frac{N_i}{2},0,1}(k) \ \cdots \ u_{1,0,1}(k)]^\mathsf{T} \\ &= [u_1(k) \ u_2(k) \ \cdots \ u_{N_i}(k)]^\mathsf{T} \in \mathbb{R}^{N_i}, \end{aligned}$$

where each element $u_{\imath,\ell,\jmath}(k)$ shares the same subscription as the system state and it will be applied to the corresponding state bin. It should be noted that, though n state bins exist, only N_i of them are controllable.

4.2.3 Input Matrix $\mathscr{B}(k)$

The input matrix $\mathscr{B}(k)$ is constructed in two steps. Since the control input only affect the current TCA status, it must be directly applied on the current state $\mathscr{X}(k)$, which implies

$$\mathscr{X}(k+1) = \mathscr{A}(k)\left(\mathscr{X}(k) + \mathcal{B}\mathscr{U}(k)\right). \tag{4.7}$$

Consequently, we have

$$\mathscr{B}(k) = \mathscr{A}(k)\mathcal{B}. \tag{4.8}$$

Herein, $\mathcal{B}$ should fully reflect the impact on the current system states by implementing the control signal $\mathscr{U}(k)$. The structure of $\mathcal{B}$ can be represented as

$$\mathcal{B} = \left[\mathcal{B}_{1,0}^{\mathsf{T}} \cdots \mathcal{B}_{N_0,0}^{\mathsf{T}} \ \mathcal{B}_{0,0}^{\mathsf{T}} \ \mathcal{B}_{1,1}^{\mathsf{T}} \cdots \mathcal{B}_{N_1,1}^{\mathsf{T}} \ \mathcal{B}_{0,1}^{\mathsf{T}}\right]^{\mathsf{T}}, \tag{4.9}$$

where $\mathcal{B}_{\ell,\jmath}$ reflects the impact on $\mathbf{x}_{\ell,\jmath}(k)$ by implementing $\mathscr{U}(k)$. The evolution process indicates that switches in a free ON bin will directly affect both the free ON bin itself and the first lockout OFF bin, while other bins are not affected, and *vice versa.* Thus, we have

$$\mathcal{B}_{2,0} = \cdots = \mathcal{B}_{N_0,0} = \mathcal{B}_{2,1} = \cdots = \mathcal{B}_{N_1,1} = \mathbf{0}_{\frac{N_i}{2} \times N_i},$$

and

$$\begin{aligned}
\mathcal{B}_{1,0} &= \left[\mathbf{0}_{\frac{N_i}{2}} \ \mathbf{E}_{\frac{N_i}{2}}\right], \\
\mathcal{B}_{0,0} &= \left[-\mathbf{I}_{\frac{N_i}{2}} \ \mathbf{0}_{\frac{N_i}{2}}\right], \\
\mathcal{B}_{1,1} &= \left[\mathbf{E}_{\frac{N_i}{2}} \ \mathbf{0}_{\frac{N_i}{2}}\right], \\
\mathcal{B}_{0,1} &= \left[\mathbf{0}_{\frac{N_i}{2}} \ -\mathbf{I}_{\frac{N_i}{2}}\right],
\end{aligned}$$

where $\mathbf{I}_{\frac{N_i}{2}}$ is the identity matrix with the dimension of $N_i/2$, and $\mathbf{E}_{\frac{N_i}{2}}$ is the reverse identity matrix with the dimension of $N_i/2$. This structure can automatically guarantee that, any switched free population will be deleted from the current bin and added to the opposite-status bin with the shallowest lockout depth.

4.2.4 System Matrix $\mathscr{A}(k)$

System matrix $\mathscr{A}(k)$ depicts the natural evolution process of the system states after switchings. Each element $\mathscr{A}_{ij}(k)$ in $\mathscr{A}(k)$ stands for the probability with which the TCA population in bin j migrates to bin i after one time step. Partitioned by

ON/OFF status, $\mathscr{A}(k)$ can be represented by blocks as

$$\mathscr{A}(k) = \begin{bmatrix} \mathscr{A}_0(k) & \mathbf{0} \\ \mathbf{0} & \mathscr{A}_1(k) \end{bmatrix} \in \mathbb{R}^{n \times n}, \tag{4.10}$$

where $\mathscr{A}_0(k)$ and $\mathscr{A}_1(k)$ depict the internal evolution in OFF and ON status, respectively. As mentioned before, there is no automatic evolution between ON and OFF bins, consequently, we have

$$\mathscr{A}_0(k) = \begin{bmatrix} \mathscr{A}_{0|1,1}(k) & \cdots & \mathscr{A}_{0|N_0,1}(k) & \mathscr{A}_{0|0,1}(k) \\ \boxed{\mathscr{A}_{0|1,2}(k)} & \cdots & \mathscr{A}_{0|N_0,2}(k) & \mathscr{A}_{0|0,2}(k) \\ \mathscr{A}_{0|1,3}(k) & \cdots & \mathscr{A}_{0|N_0,3}(k) & \mathscr{A}_{0|0,3}(k) \\ \vdots & \ddots & \mathscr{A}_{0|N_0,N_0}(k) & \mathscr{A}_{0|0,N_0}(k) \\ \mathscr{A}_{0|1,0}(k) & \cdots & \boxed{\mathscr{A}_{0|N_0,0}(k)} & \boxed{\mathscr{A}_{0|0,0}(k)} \end{bmatrix}. \tag{4.11}$$

In $\mathscr{A}_0(k)$, except for the boxed ones, all blocks are zeros matrices due to the nature of the transition. Each block $\mathscr{A}_{0|\ell_p,\ell_q}(k)$ represents the transition matrix from all temperature bins in lockout depth ℓ_p to all temperature bins in lockout depth ℓ_q. Since for all boxed blocks, lockout time has already been filtered, the structure of each block is constructed regardless of the lockout time, which implies that they share the same structure. Specifically, an example of $\mathscr{A}_{0|2,3}(k)$ can be written as

$$\mathscr{A}_{0|2,3}(k) = \begin{array}{c} \\ \scriptstyle 1,3,0 \\ \scriptstyle 2,3,0 \\ \vdots \\ \scriptstyle \frac{N_i}{2},3,0 \end{array} \begin{array}{c} \begin{array}{cccc} \scriptstyle 1,2,0 & \scriptstyle 2,2,0 & \scriptstyle \cdots & \scriptstyle \frac{N_i}{2},2,0 \end{array} \\ \begin{bmatrix} \star & \star & \cdots & \star \\ 0 & \star & \cdots & \star \\ \vdots & \vdots & \ddots & \vdots \\ 0 & 0 & \cdots & \star \end{bmatrix} \end{array}, \tag{4.12}$$

where $\star$ represents the probability that needs to be derived.

Having the reversed temperature order, the structure of $\mathscr{A}_1(k)$ can be derived by following the similar lines as in $\mathscr{A}_0(k)$. The details are omitted to avoid redundancy.

4.2.5 Analytical Derivations of $\mathscr{A}(k)$

In this Section, the derivations of elements $\star$ in $\mathscr{A}_{0|\ell_p,\ell_q}(k)$ and $\mathscr{A}_{1|\ell_p,\ell_q}(k)$ will be presented. The derivation is proceeded in three cases, in which the former two are heuristic to the third one which will be used in real calculations. As mentioned, since the effect of the lockout depth has been automatically filtered, only the temperature matters. The derivations follow the similar idea as in [65]; however, the starting temperature distribution is generalized.

4.2.5.1 Point-to-Point

We first investigate how to determine the parameter a when a TCA migrates from a temperature point to another temperature point. Continue to use the notations in Chapter 3, let $\zeta_i(k)$, $\zeta_i(k+1)$, and $\zeta_o(k)$ denote the starting indoor temperature point, terminal indoor temperature point, and the ambient temperature, respectively. Then we have

$$\zeta_i(k+1) = a\zeta_i(k) + (1-a)(\zeta_o(k) + g(k)RP), \tag{4.13}$$

where $g(k)$ is 0 when the TCA is OFF and is 1 when the TCA is ON. With the full temperature information, a can be calculated as

$$a = \frac{\zeta_i(k+1) - \zeta_o(k) - g(k)RP}{\zeta_i(k) - \zeta_o(k) - g(k)RP}, \tag{4.14}$$

where $g(k)$ is determined by the status of TCA after the control action. This is to say, any TCA with the parameter a calculated in (4.14) can migrate from $\zeta_i(k)$ to

$\zeta_i(k+1)$ after one time step with ambient temperature $\zeta_o(k)$.

4.2.5.2 Point-to-Range

In this case, a shall be determined by considering the case that TCAs migrate from a temperature point to a temperature range. Different from the previous scenario, the terminal temperature falls into a range, i.e., $\underline{\zeta}_i(k+1) \leq \zeta_i(k+1) \leq \overline{\zeta}_i(k+1)$. Thus (4.14) becomes

$$\underline{a} \leq a \leq \overline{a}. \tag{4.15}$$

On the one hand

$$\begin{aligned} \underline{a} &= \frac{\underline{\zeta}_i(k+1) - \zeta_o(k)}{\zeta_i(k) - \zeta_o(k)}, \\ \overline{a} &= \frac{\overline{\zeta}_i(k+1) - \zeta_o(k)}{\zeta_i(k) - \zeta_o(k)}, \end{aligned} \tag{4.16}$$

when the TCA is OFF; On the other hand,

$$\begin{aligned} \underline{a} &= \frac{\overline{\zeta}_i(k+1) - \zeta_o(k) - RP}{\zeta_i(k) - \zeta_o(k) - RP}, \\ \overline{a} &= \frac{\underline{\zeta}_i(k+1) - \zeta_o(k) - RP}{\zeta_i(k) - \zeta_o(k) - RP}, \end{aligned} \tag{4.17}$$

when the TCA is ON. The reason for swapping $\overline{\zeta}_i(k+1)$ and $\underline{\zeta}_i(k+1)$ in the numerators of $\underline{a}$ and $\overline{a}$ is because of the negative sign caused by $-RP$. Thus, the probability for all TCAs with $\zeta_i(k)$ migrating to $[\underline{\zeta}_i(k+1), \overline{\zeta}_i(k+1)]$ is calculated as

$$\Pr_{\imath_1,\imath_2} = \int_{\underline{a}}^{\overline{a}} p(a)\mathrm{d}a, \tag{4.18}$$

where $\imath_1$ stands for the starting temperature, $\imath_2$ stands for the terminal temperature range, and $p(a)$ is the probability density function of the distribution of a which is directly determined by the distribution of C. In the later simulation, we assume that a follows a uniform distribution according to a specific distribution of C. Other distributions may be considered in the future work. Suppose a is distributed in $[a_l, a_u]$, then any calculated a out of the range is regarded as invalid.

4.2.5.3 Range-to-Range

This section discusses how to calculate the probability when all TCAs in a temperature range migrate to another temperature range. It should be noted that this is the real case for calculating the jumping probability. In addition to the previous scenario, the starting temperature also falls into a range, i.e., $\underline{\zeta}_i(k) \leq \zeta_i(k) \leq \overline{\zeta}_i(k)$. With a fixed $\zeta_i(k)$, the lower and upper bounds for a can be calculated by (4.16) or (4.17). However, the probability in (4.18) will be modified to

$$\Pr_{\imath_1,\imath_2} = \int\limits_{\underline{\zeta}_i(k)}^{\overline{\zeta}_i(k)} p(\zeta_i(k)) \int\limits_{\underline{a}}^{\overline{a}} p(a)\mathrm{d}a\mathrm{d}\zeta_i(k), \tag{4.19}$$

where $\imath_1$ stands for the starting temperature range, $\imath_2$ stands for the terminal temperature range, and $p(\zeta_i(k))$ is the probability density function of the starting air temperature. In this chapter, we follow [65] to assume that the starting air temperature of TCAs is uniformly distributed in $[\underline{\zeta}_i(k), \overline{\zeta}_i(k)]$. This assumption is made due to the fact that the integral intervals are relatively small. In addition, in real cases, this probability distribution is a function of time-varying parameters of the model, e.g., ambient temperature, which results in a time-varying probability distribution. A general form in (4.19) is given for any appropriate distributions. Thus, the probability for TCAs in $[\underline{\zeta}_i(k), \overline{\zeta}_i(k)]$ migrating to $[\underline{\zeta}_i(k+1), \overline{\zeta}_i(k+1)]$ can be calculated by (4.19).

4.2.5.4 Calculate $\star$ in $\mathscr{A}_{\jmath|\ell_p,\ell_q}$

Each element in $\mathscr{A}_{\jmath|\ell_p,\ell_q}$ represents the jumping probability from bin $(\imath_1, \ell_p, \jmath)$ to bin $(\imath_2, \ell_q, \jmath)$, $\forall \imath_1, \imath_2 = 1, \dots, N_i/2$, ℓ_p, ℓ_q, and $\jmath$ are fixed. Herein, $\imath_1$ stands for the starting temperature range $[\underline{\zeta}_i(k), \overline{\zeta}_i(k)]$, and $\imath_2$ stands for the terminal temperature range $[\underline{\zeta}_i(k+1), \overline{\zeta}_i(k+1)]$. Then by determining the temperature information and ON/OFF status from $\imath_1$, $\imath_2$, and $\jmath$, $\star$ can be determined by using (4.16), (4.17), and (4.19).

Remark 4.1: Within a small range of ambient temperature, the transition matrix can be regarded as a constant one. Thus, the ambient temperature can be partitioned into several small pieces in advance and it is possible to make a lookup table to include all transition matrices according to different ambient temperature ranges. By doing so, transition matrices obtained offline can be directly used in the online optimization without any online calculation. ■

4.2.6 System Output

The system output is the aggregated power consumption of all TCAs. Thus, only the TCAs in ON status contribute to this. Suppose ν TCAs with average power P exist in an area, the aggregated power output $y(k)$ can be estimated as

$$y(k) = \mathscr{C}\mathscr{X}(k) + \mathscr{D}\mathscr{U}(k), \tag{4.20}$$

where

$$\begin{aligned} \mathscr{C} &= P\nu[\underbrace{0\ 0\ \cdots\ 0}_{\frac{N_i}{2}(N_0+1)}\ \underbrace{1\ 1\ \cdots\ 1}_{\frac{N_i}{2}(N_1+1)}], \\ \mathscr{D} &= \mathscr{C}\mathcal{B}. \end{aligned} \tag{4.21}$$

4.3 DMPC Design

A DMPC strategy will be developed in this section. In order to better illustrate the DMPC scheme, we introduce the concept *virtual group (VG)*. Essentially, VG is the same as the state bin. This DMPC strategy will partition the overall control objective into n VGs; then each VG computes its own optimal control signal based on the information gathered from other VGs. In [101, 102], DMPC strategies for time-invariant systems were discussed; herein the time-varying case will be studied.

4.3.1 The DMPC Scheme

To make it clear, let m denote N_i. Since we treat each element in $\mathscr{X}(k)$ as the portion of the TCAs in a specific status, by discarding the subscriptions in (4.11), the system matrix can be partitioned for all VGs as

$$\mathscr{A}(k) = \begin{bmatrix} \mathscr{A}_{11}(k) & \mathscr{A}_{12}(k) & \cdots & \mathscr{A}_{1n}(k) \\ \mathscr{A}_{21}(k) & \mathscr{A}_{22}(k) & \cdots & \mathscr{A}_{2n}(k) \\ \vdots & \vdots & \ddots & \vdots \\ \mathscr{A}_{n1}(k) & \mathscr{A}_{n2}(k) & \cdots & \mathscr{A}_{nn}(k) \end{bmatrix} \in \mathbb{R}^{n\times n}. \tag{4.22}$$

And the system states can be equally represented as

$$\mathscr{X}(k) = [x_1(k)\ x_2(k)\ \cdots\ x_n(k)]^{\mathsf{T}} \in \mathbb{R}^n. \tag{4.23}$$

As mentioned, among all n VGs, only m of them are free to be controlled. Thus, $\mathscr{U}(k)$ can be equally represented as

$$\mathscr{U}(k) = [u_1(k)\ u_2(k)\ \cdots\ u_m(k)]^{\mathsf{T}} \in \mathbb{R}^m. \tag{4.24}$$

Consequently, the input matrix $\mathscr{B}(k)$ can be partitioned as

$$\mathscr{B}(k) = \begin{bmatrix} \mathscr{B}_{11}(k) & \mathscr{B}_{12}(k) & \cdots & \mathscr{B}_{1m}(k) \\ \mathscr{B}_{21}(k) & \mathscr{B}_{22}(k) & \cdots & \mathscr{B}_{2m}(k) \\ \vdots & \vdots & \ddots & \vdots \\ \mathscr{B}_{n1}(k) & \mathscr{B}_{n2}(k) & \cdots & \mathscr{B}_{nm}(k) \end{bmatrix} \in \mathbb{R}^{n\times m}. \tag{4.25}$$

Then for the ith VG we have

$$x_i(k+1) = \mathscr{A}_{ii}(k)x_i(k) + \sum_{j\neq i} \mathscr{A}_{ij}(k)x_j(k) + \sum_{h=1}^{m} \mathscr{B}_{ih}(k)u_h(k). \tag{4.26}$$

Define the state prediction vector for the ith VG as

$$X_i(k) = [x_i(k+1|k) \ \cdots \ x_i(k+N|k)]^{\mathsf{T}}, \tag{4.27}$$

where N is the prediction horizon and $x_i(k+l|k)$ is the prediction of $x_i(k+l)$ with the knowledge of $x_i(k)$. Then by recursion, $X_i(k)$ can be written as

$$X_i(k) = \sum_{j=1}^{n} f_{ij}(k)x_j(k|k) + \sum_{j\neq i} g_{ij}(k)X_j(k) + \sum_{h=1}^{m} z_{ih}(k)U_h(k), \tag{4.28}$$

where

$$U_h(k) = [u_h(k|k) \ u_h(k+1|k) \ \cdots \ u_h(k+N-1|k)]^{\mathsf{T}} \tag{4.29}$$

is the input prediction vector and

$$
\begin{aligned}
f_{ij}(k) &= \begin{bmatrix} f_{ij,1}(k)^{\mathsf{T}} & \cdots & f_{ij,N}(k)^{\mathsf{T}} \end{bmatrix}^{\mathsf{T}}, \\
g_{ij}(k) &= \begin{bmatrix} g_{ij,11}(k) & g_{ij,12}(k) & \cdots & g_{ij,1N}(k) \\ g_{ij,21}(k) & g_{ij,22}(k) & \cdots & g_{ij,2N}(k) \\ \vdots & \vdots & \ddots & \vdots \\ g_{ij,N1}(k) & g_{ij,N2}(k) & \cdots & g_{ij,NN}(k) \end{bmatrix}, \\
z_{ij}(k) &= \begin{bmatrix} z_{ij,11}(k) & z_{ij,12}(k) & \cdots & z_{ij,1N}(k) \\ z_{ij,21}(k) & z_{ij,22}(k) & \cdots & z_{ij,2N}(k) \\ \vdots & \vdots & \ddots & \vdots \\ z_{ij,N1}(k) & z_{ij,N2}(k) & \cdots & z_{ij,NN}(k) \end{bmatrix},
\end{aligned}
$$

where

$$
f_{ij,\imath}(k) = \begin{cases} \mathbf{I} & i = j \text{ and } \imath = 1, \\ \mathbf{0} & i \neq j \text{ and } \imath = 1, \\ \prod_{l=N-\imath+1}^{N-2} \mathscr{A}_{ii}(k+N-l)\mathscr{A}_{ij}(k) & \text{else}, \end{cases}
$$

$$
g_{ij,\imath\jmath}(k) = \begin{cases} \mathbf{0} & x = 1 \text{ or } y = 1, \text{ or } \imath \leq \jmath, \\ \prod_{l=N-\imath+1}^{N-\jmath-1} \mathscr{A}_{ii}(k+N-l-1)\mathscr{A}_{ij}(k+\jmath-1) & \text{else}, \end{cases}
$$

$$
z_{ih,\imath\jmath}(k) = \begin{cases} \mathbf{0} & \imath \leq \jmath, \\ \prod_{l=N-\imath+2}^{N-\jmath} \mathscr{A}_{ii}(k+N-l)\mathscr{B}_{ih}(k+\jmath-1) & \text{else}, \end{cases}
$$

$\forall \imath, \jmath = 1, \ldots, N$, $i, j = 1, \ldots, n$, and $h = 1, \ldots, m$.

By augmenting all VGs, we define the augmented system prediction state as

$$
\tilde{X}(k) = \begin{bmatrix} X_1(k)^{\mathsf{T}} & \cdots & X_n(k)^{\mathsf{T}} \end{bmatrix}^{\mathsf{T}} \in \mathbb{R}^{Nn}, \tag{4.30}
$$

and the augmented input vector as

$$\tilde{U}(k) = \begin{bmatrix} U_1(k)^\mathsf{T} & \cdots & U_m(k)^\mathsf{T} \end{bmatrix}^\mathsf{T} \in \mathbb{R}^{Nm}. \tag{4.31}$$

With the state knowledge at time k defined as $x(k|k) = [x_1(k|k)\; x_2(k|k)\; \cdots\; x_n(k|k)]^\mathsf{T}$, we have the augmented system dynamics represented as

$$\mathcal{A}(k)\tilde{X}(k) = \mathcal{E}(k)\tilde{U}(k) + \mathcal{G}(k)x(k|k), \tag{4.32}$$

where

$$\begin{aligned} \mathcal{A}(k) &= \begin{bmatrix} \mathbf{I} & -g_{12}(k) & \cdots & -g_{1n}(k) \\ -g_{21}(k) & \mathbf{I} & \cdots & -g_{2n}(k) \\ \vdots & \vdots & \ddots & \vdots \\ -g_{n1}(k) & -g_{n2}(k) & \cdots & \mathbf{I} \end{bmatrix}, \\ \mathcal{E}(k) &= \begin{bmatrix} z_{11}(k) & z_{12}(k) & \cdots & z_{1m}(k) \\ z_{21}(k) & z_{22}(k) & \cdots & z_{2m}(k) \\ \vdots & \vdots & \ddots & \vdots \\ z_{n1}(k) & z_{n2}(k) & \cdots & z_{nm}(k) \end{bmatrix}, \\ \mathcal{G}(k) &= \begin{bmatrix} f_{11}(k) & f_{12}(k) & \cdots & f_{1n}(k) \\ f_{21}(k) & f_{22}(k) & \cdots & f_{2n}(k) \\ \vdots & \vdots & \ddots & \vdots \\ f_{n1}(k) & f_{n2}(k) & \cdots & f_{nn}(k) \end{bmatrix}. \end{aligned} \tag{4.33}$$

Note that $\mathcal{A}(k)$ is invertible and therefore we have

$$\begin{aligned} \tilde{X}(k) &= \mathcal{A}^{-1}(k)\mathcal{E}(k)\tilde{U}(k) + \mathcal{A}^{-1}(k)\mathcal{G}(k)x(k|k) \\ &= \tilde{\mathcal{E}}(k)\tilde{U}(k) + \tilde{\mathcal{G}}(k)x(k|k), \end{aligned} \tag{4.34}$$

with

$$\begin{aligned}\tilde{\mathcal{E}}(k) &= \begin{bmatrix} \tilde{z}_{11}(k) & \tilde{z}_{12}(k) & \cdots & \tilde{z}_{1m}(k) \\ \tilde{z}_{21}(k) & \tilde{z}_{22}(k) & \cdots & \tilde{z}_{2m}(k) \\ \vdots & \vdots & \ddots & \vdots \\ \tilde{z}_{n1}(k) & \tilde{z}_{n2}(k) & \cdots & \tilde{z}_{nm}(k) \end{bmatrix}, \\ \tilde{\mathcal{G}}(k) &= \begin{bmatrix} \tilde{f}_{11}(k) & \tilde{f}_{12}(k) & \cdots & \tilde{f}_{1n}(k) \\ \tilde{f}_{21}(k) & \tilde{f}_{22}(k) & \cdots & \tilde{f}_{2n}(k) \\ \vdots & \vdots & \ddots & \vdots \\ \tilde{f}_{n1}(k) & \tilde{f}_{n2}(k) & \cdots & \tilde{f}_{nn}(k) \end{bmatrix}.\end{aligned} \tag{4.35}$$

Through the above procedure, the predicted states of different subsystems are decoupled and consequently we have

$$X_i(k) = \sum_{j=1}^{n} \tilde{f}_{ij}(k) x_j(k|k) + \sum_{h=1}^{m} \tilde{z}_{ih}(k) U_h(k). \tag{4.36}$$

Let $Y(k)$ and $Y_0(k)$ denote the predicted aggregated power consumption and the desired power trajectory, respectively, with

$$\begin{aligned} Y(k) &= [y(k|k) \ \cdots \ y(k+N-1|k)]^{\mathsf{T}}, \\ Y_0(k) &= [y_0(k) \ \cdots \ y_0(k+N-1)]^{\mathsf{T}}. \end{aligned} \tag{4.37}$$

Then the centralized objective function at time instant k, which is used for tracking the desired trajectory, can be represented as

$$\min_{\tilde{U}(k)} \mathcal{J}_m(k) = \min_{\tilde{U}(k)} \|Y(k) - Y_0(k)\|_2. \tag{4.38}$$

With the output matrices in (4.20) partitioned as

$$\begin{aligned} \mathscr{C} &= \left[\mathscr{C}_1 \; \mathscr{C}_2 \; \cdots \; \mathscr{C}_n\right], \\ \mathscr{D} &= \left[\mathscr{D}_1 \; \mathscr{D}_2 \; \cdots \; \mathscr{D}_m\right], \end{aligned} \tag{4.39}$$

in which each $\mathscr{C}_i$ represents the output matrix for the corresponding VG and each $\mathscr{D}_h$ represents the output-control matrix for the corresponding free VG. $Y(k)$ can be rewritten as

$$Y(k) = [C_1 \; C_2 \; \cdots \; C_n]\tilde{X}(k) + [D_1 \; D_2 \; \cdots \; D_m]\tilde{U}(k), \tag{4.40}$$

where

$$C_i = \mathrm{diag}\{\mathscr{C}_i\} = \begin{bmatrix} \mathscr{C}_i & & \\ & \ddots & \\ & & \mathscr{C}_i \end{bmatrix}, D_h = \mathrm{diag}\{\mathscr{D}_h\} = \begin{bmatrix} \mathscr{D}_h & & \\ & \ddots & \\ & & \mathscr{D}_h \end{bmatrix}, \tag{4.41}$$

$\forall i = 1, \ldots, n, \; h = 1, \ldots, m$, with appropriate dimensions. Consequently, $\mathcal{J}_m(k)$ can be rewritten as

$$\mathcal{J}_m(k) = \left\| \sum_{i=1}^{n} C_i X_i(k) + \sum_{h=1}^{m} D_h U_h(k) - Y_0(k) \right\|_2 . \tag{4.42}$$

Therefore, we have

$$\sum_{i=1}^{n} C_i X_i(k) + \sum_{h=1}^{m} D_h U_h(k) - Y_0(k) = \sum_{i=1}^{n} C_i \sum_{h=1}^{m} \tilde{z}_{ih} U_j(k) + \sum_{h=1}^{m} D_h U_h(k) + c_c,$$

where

$$c_c = \sum_{i=1}^{n} C_i \sum_{j=1}^{n} \tilde{f}_{ij} x_j(k|k) - Y_0(k). \tag{4.43}$$

In a distributed fashion, when dealing with the sth controllable VG, $U_s(k)$ needs to be extracted from other $U_h(k)$'s, which implies

$$\begin{aligned}\mathcal{J}_m^2(k) &= \sum_{i=1}^{n} C_i \left(\tilde{z}_{is} U_s(k) + \sum_{h \neq s}^{m} \tilde{z}_{ih} U_h(k) \right) + \sum_{h \neq s}^{m} D_h U_h(k) + D_s U_s(k) + c_c \\ &= \sum_{i=1}^{n} C_i \tilde{z}_{is} U_s(k) + \sum_{i=1}^{n} C_i \sum_{h \neq s}^{m} \tilde{z}_{ih} U_h(k) + \sum_{h \neq s}^{m} D_h U_h(k) + D_s U_s(k) + c_c \quad (4.44) \\ &= \left(\sum_{i=1}^{n} C_i \tilde{z}_{is} + D_s \right) U_s(k) + \sum_{h \neq s}^{m} \left(\sum_{i=1}^{n} C_i \tilde{z}_{ih} + D_h \right) U_h(k) + c_c.\end{aligned}$$

Then for the sth controllable VG, the local objective function can be written as

$$\mathcal{J}_s(k) = \left\| \left(\sum_{i=1}^{n} C_i \tilde{z}_{is} + D_s \right) U_s(k) + \sum_{h \neq s}^{m} \left(\sum_{i=1}^{n} C_i \tilde{z}_{ih} + D_h \right) U_h(k) + c_c \right\|_2 . \quad (4.45)$$

Note that only $U_s(k)$ is the optimizer for the sth controllable VG, other $U_h(k)$'s are the control signals obtained from the last iteration or the initial values and they will be treated as constants in this optimization.

4.3.2 Constraints

Since the control signal represents the absolute portion of TCAs in a specific VG that needs to be switched to the opposite status, this control signal must be bounded by

$$\mathbf{0} \leq U_s(k) \leq \mathbf{1}, \ \forall s = 1, \dots, m. \quad (4.46)$$

In addition, the control signal must be limited to avoid over switching the available TCAs, which implies

$$0 \leq x_i(k + l|k) + \sum_{h=1}^{m} \mathscr{B}_{ih}(k) u_h(k + l|k) \leq 1, \quad (4.47)$$

$\forall i = 1, \ldots, n,\ l = 0, \ldots, N-1.$

Note that the system states are not necessary to be limited since the system transition matrix automatically guarantees the states staying between 0 and 1, and $\sum_{i=1}^{n} x_i(k) = 1$.

4.3.3 DMPC Algorithm

At time instant k, the procedure to obtain the control signal can be described as

Algorithm 4.1 Acquisition and implementation of DMPC

```
Collect the current states $x_i(k|k)$ from all VGs.
Initialize $U_s^{(0)}(k)$ (control signal for the $s$th controllable VG) and $\tilde{U}^{(0)}(k)$ (control signal for all VGs).
Maximum iteration $p_{max} \geq 0$. Initialize iteration number $p = 1$.
Infinitesimal $\epsilon > 0$ and tolerance $\rho_s = \Gamma\epsilon$, where $\Gamma \gg 1$.
Updating weight $0 < \omega_s < 1, \sum_{s=1}^{m} \omega_s = 1$.
procedure
    while $\rho_s > \epsilon$, $\forall s = 1, \ldots, m$ and $p \leq p_{max}$ do
        for $s = m$ to 1 do
            $U_s^{*(p)}(k) = \underset{U_s(k)}{\arg\min}\, \mathcal{J}_s(k)$
            s.t. (4.46) and (4.47)
            $U_s^{(p)}(k) = \omega_s U_s^{*(p)}(k) + (1-\omega_s) U_s^{(p-1)}(k)$
        end for
        $\rho_s = \|\tilde{U}^{(p)}(k) - \tilde{U}^{(p-1)}(k)\|_2$
        $p = p + 1$
    end while
    Without considering the lockout status, TCAs that are outside the comfortable temperature range need to be forced to switch, i.e., TCAs with air temperature lower(higher) than $\underline{T}_i(\overline{T}_i)$ are forced to switch ON(OFF). The number of switchings of this type of TCAs falls into the state bins with the same temperature range.
    Only apply the first element of the calculated control action to the system, i.e., $u_s^{(p)}(k|k)$, for each controllable VG. Uncontrollable VGs will evolve naturally.
end procedure
```

Based on the proposed DMPC algorithm, we have the following **Remarks** and **Proposition** to conclude:

Remark 4.2: In the above algorithm, the DMPC problem is always feasible as long as the order of executing the optimization is from $s = m$ to $s = 1$, i.e., from low-temperature ON VGs to high-temperature ON VGs and from high-temperature OFF VGs to low-temperature OFF VGs. In the proposed iterative DMPC algorithm, the optimization problem for the sth VG is executed by assuming states and control inputs of other VGs are fixed and constants. Suppose we are dealing with the sth controllable OFF VG at time k: it has no problem to determine the control input at time k based on the constant setup; however, it is inappropriate to decide the control actions at time $k + 1$ before acquiring the knowledge that how much population left in higher-temperature VGs are available to migrate to the current sth VG. Without having a determined switching actions of higher-temperature VGs, prematurely executing the optimization problem for lower-temperature VGs will encounter a conflict between Eqns. (4.46) and (4.47), which makes the optimization problem infeasible. This implies lower-temperature VGs switch more TCAs than the available number. In contrast, if executing optimizations in an opposite way, there is no migration from lower-temperature VGs to higher-temperature VGs, thus both Eqns. (4.46) and (4.47) can be satisfied. The logic for VGs in ON status is the same. ■

Proposition 4.1: Given the DMPC formulation defined in (4.45) subject to (4.46) and (4.47), $\forall s = 1, 2, \ldots, m$, the sequence of the cost functions $\mathcal{J}_m\big(U_1^{(p)}(k), U_2^{(p)}(k), \ldots, U_m^{(p)}(k); x(k|k)\big)$ generated by the proposed algorithm is non-increasing with the iteration number p. ■

Proof of Proposition 4.1 [102]: In the following proof, we drop the time k. From the above algorithm, we know that

$$\begin{aligned}
&\mathcal{J}_m\left(U_1^{(p-1)},\ldots,U_{s-1}^{(p-1)},U_s^{*(p)},U_{s+1}^{(p-1)},\ldots,U_m^{(p-1)};x(k|k)\right)\\
&\le \mathcal{J}_m\left(U_1^{(p-1)},U_2^{(p-1)},\ldots,U_m^{(p-1)};x(k|k)\right),\\
&\forall s=1,2,\ldots,m.
\end{aligned}$$

From (4.42) we have

$$\mathcal{J}_m=\left\|q_1U_1+\cdots+q_mU_m+c_c\right\|_2, \tag{4.48}$$

where $q_h=\sum_{i=1}^{n}C_i\tilde{z}_{ih}$. At the pth iteration, we have

$$\begin{aligned}
&\mathcal{J}_m\left(U_1^{(p)},\ldots,U_m^{(p)};x(k|k)\right)\\
=&\mathcal{J}_m\left(\omega_1U_1^{*(p)}+(1-\omega_1)U_1^{(p-1)},\ldots,\omega_mU_m^{*(p)}+(1-\omega_m)U_m^{(p-1)};x(k|k)\right)\\
=&\left\|q_1\left(\omega_1U_1^{*(p)}+(1-\omega_1)U_1^{(p-1)}\right)+\cdots+q_m\left(\omega_mU_m^{*(p)}+(1-\omega_m)U_m^{(p-1)}\right)+c_c\right\|_2\\
=&\left\|q_1\left(\omega_1U_1^{*(p)}+\omega_2U_1^{(p-1)}+\cdots+\omega_mU_1^{(p-1)}\right)+\cdots\right.\\
&\left.+q_m\left(\omega_1U_m^{(p-1)}+\omega_2U_m^{(p-1)}+\cdots+\omega_mU_m^{*(p)}\right)+c_c\right\|_2\\
=&\left\|\omega_1\left(q_1U_1^{*(p)}+q_2U_2^{(p-1)}+\cdots+q_mU_m^{(p-1)}+c_c\right)+\cdots\right.\\
&\left.+\omega_m\left(q_1U_1^{(p-1)}+q_2U_2^{(p-1)}+\cdots+q_mU_m^{*(p)}+c_c\right)\right\|_2.
\end{aligned}$$

Because of the convexity of $\mathcal{J}_m(\cdot)$, we can obtain

$$\begin{aligned}
&\mathcal{J}_m\left(U_1^{(p)},\ldots,U_m^{(p)};x(k|k)\right)\\
&\leq \omega_1\left\|q_1U_1^{*(p)}+q_2U_2^{(p-1)}+\cdots+q_mU_m^{(p-1)}+c_c\right\|_2+\cdots\\
&\quad+\omega_m\left\|q_1U_1^{(p-1)}+q_2U_2^{(p-1)}+\cdots+q_mU_m^{*(p)}+c_c\right\|_2\\
&\leq\left\|q_1U_1^{(p-1)}+q_2U_2^{(p-1)}+\cdots+q_mU_m^{(p-1)}+c_c\right\|_2\\
&=\mathcal{J}_m\left(U_1^{(p-1)},\ldots,U_m^{(p-1)};x(k|k)\right),
\end{aligned}$$

in which the equality is obtained if $U_s^{(p)}=U_s^{(p-1)}$, $\forall s=1,2,\ldots,m$. ■

Remark 4.3: Line 16 of Algorithm 4.1 is to guarantee the end-users' comfort level. Since in this problem formulation, the constraint for temperature is not able to be incorporated into, and then if some TCAs are outside the comfort range, they will definitely impair the regulation flexibility. This can be avoided by adding a flexibility penalty to the objective function to steer the TCAs away from the state bins on the boundaries. Then, the objective function can be rewritten as

$$\mathcal{J}_{pm}(k)=\mathcal{J}_m(k)+\mathcal{J}_p(k), \tag{4.49}$$

where $\mathcal{J}_p(k)=\lambda\|\boldsymbol{\mathcal{R}}\tilde{X}(k)\|_2$. Herein, λ is a positive scalar to balance the scale and $\boldsymbol{\mathcal{R}}$ is a diagonal matrix where the elements corresponding to boundary state bins are way larger than those corresponding to the inner bins. The effectiveness of $\mathcal{J}_p(k)$ will be illustrated in later case studies. ■

4.3.4 Case Study

In this section, a set of simulations are conducted for 1000 TCAs using a winter ambient temperature profile. The purpose is to provide primary frequency control. R is selected to be 0.057°C/W. The equivalent heat capacity follows a specific distribution within $[3000, 5900]$J/°C and consequently we have a uniform distribution of a. Rated power for an individual TCA is 3 kW. The comfort range for end-users is ±2°C around 21°C. $N_i = 10$ is set for the aggregation model and a 40-second prediction horizon is set for the DMPC scheme. The desired trajectory construction follows Section 3.4.2.

4.3.4.1 System Performance

The indoor air temperature of 1000 TCAs is initialized in the following way: (1) 20% of them are out of the comfort range. This is to consider the case that some end-users may shut down their appliances in the daytime and go to work, and turn ON when they are back; (2) the other 80% TCAs are randomly distributed within the comfort range and are always available for grid services. By adopting the proposed control schemes (with and without the flexibility penalty introduced in **Remark 4.3**), the indoor air temperature and ambient temperature evolutions within a day can be found in Figure 4.2. It can be readily observed from Figure 4.2 that by including the flexibility penalty, the indoor air temperature can be well restricted within the comfort range; while without this penalty, though the indoor air temperature is more diversified and spreads over the whole comfort range, it involves numerous temperature limit violations. In the beginning of the temperature evolution, those 20% TCAs keep being in ON status to drag the temperature back to the comfort range.

The desired trajectory tracking performance of controllers with and without penalty can be clearly observed from Figure 4.3. For the controller with penalty, the tracking performance in the very beginning is acceptable because there are still 80% TCAs available for switching; however, when most TCAs within the comfort range touch the lower limit where out-of-bound TCAs have not risen to, the tracking performance becomes worse. Large tracking errors occur during this stage due to the loss of con-

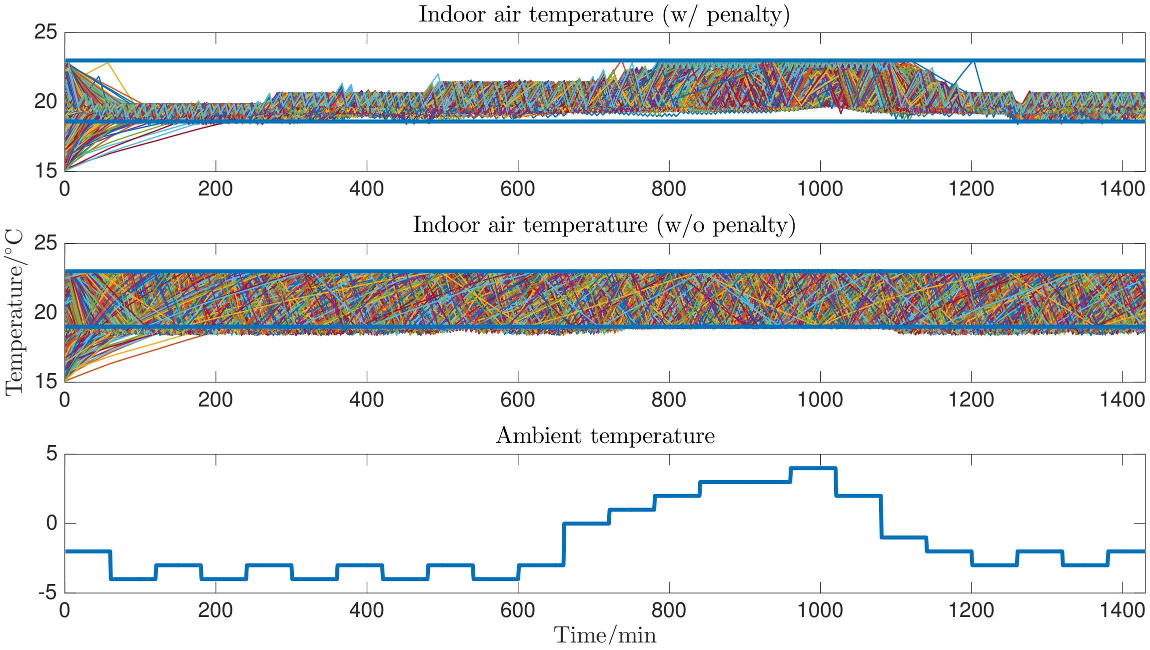

Figure 4.2: Indoor air temperature evolution and ambient temperature.

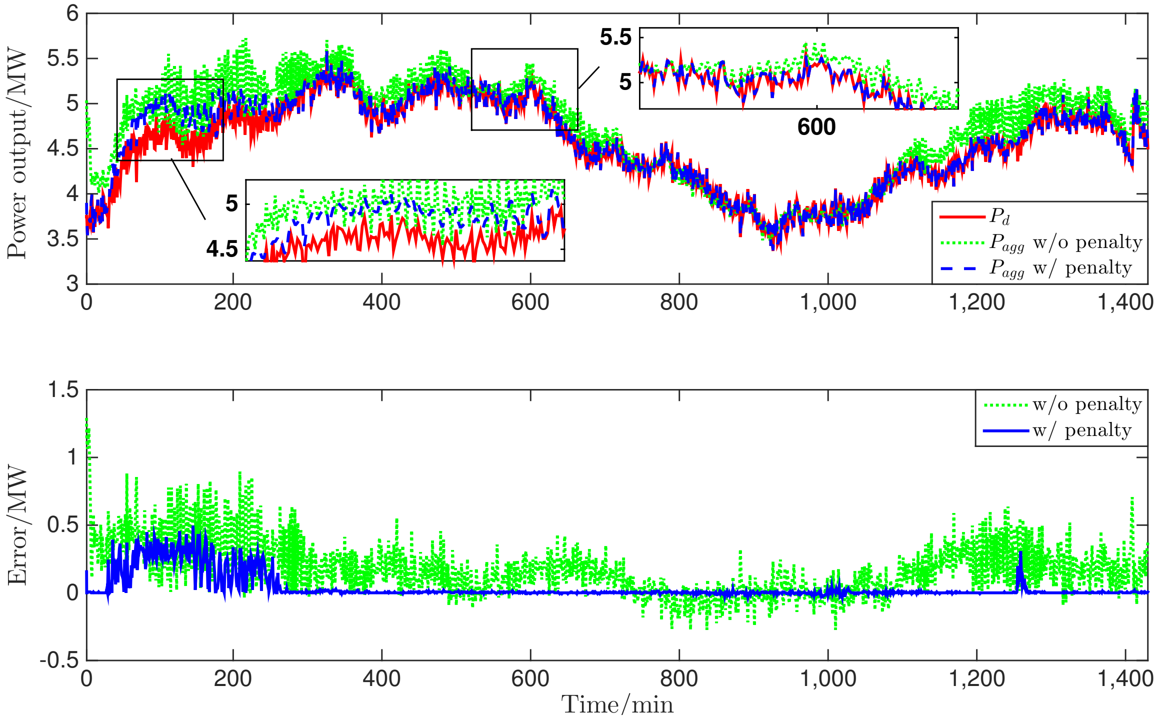

Figure 4.3: Desired trajectory tracking and error.

trollable TCAs. After all TCAs getting back to the comfort range, the tracking performance becomes normal. Except large tracking errors at this stage, most errors are below 0.005 MW while with a spike 0.3 MW near the end. This spike appears because suboptimal solutions are obtained at those points. The direct reason for obtaining suboptimal solutions is the maximum iteration number p_{max}. We set $p_{max} = 5$ to ensure the control sequence can be obtained within an acceptable time. It is proved in **Proposition 4.1** that, as the iteration number rises, the value of the cost function is non-increasing with the iteration number. Though a tolerance is set to check the convergency of the solution, it is still possible to have a slightly decreased cost but distinct control sequences. In engineering problems, it is normal to compromise to a suboptimal solution obtained in a short time instead of pursuing the optimal one in a long time. By the observations of the simulations, in most cases, the optimal solution can be obtained within 5 iterations, however, some may take more than 10 iterations. We examined around the spike by removing the iteration number cap and found out that it would need 15-20 iterations to get the optimal solution. Define the normed error in a day as $\varepsilon = \|P_d - P_{agg}\|/\|P_d\|$, then ε for those 1000 TCAs is only 2.19%. The out-of-bound temperature initialization contributes 80% of the error. For the controller without flexibility penalty, the tracking error is obviously larger at the level of 5.81%. This further reveals that the flexibility penalty in **Remark 4.3** can effectively preserve the aggregate regulation flexibility.

As mentioned in Section 4.3.3, actual switching actions are usually different from the calculated nominal ones because of the temperature limit violations. The comparisons between the calculated and actual switchings of both controllers can be seen in Figure 4.4. For the controller with flexibility penalty, it can be readily observed from the first plot that, the actual total number of switchings can well match the calculated one. In addition, except few spikes, errors rarely exist. The spikes in the

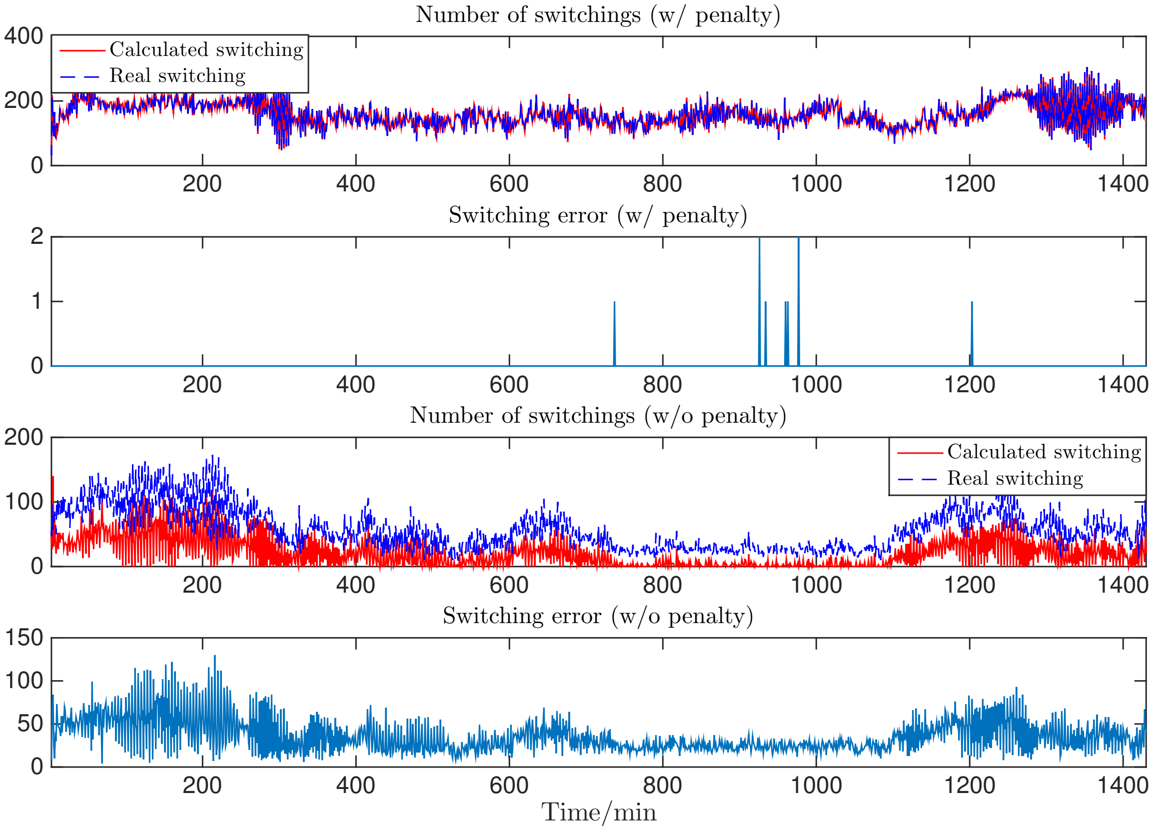

Figure 4.4: Comparisons between the actual and calculated switchings.

second plot of Figure 4.4 are due to the relatively low and high ambient temperature around those points at which some TCAs may need to be forced to switch in order to keep the temperature in the comfort range. However, by dropping the penalty, from the third and fourth plots, actual switchings can hardly match the nominal ones, which directly results in a low-quality tracking.

Comparing with a centralized MPC controller with the same objective function, the proposed DMPC scheme outperforms in terms of the computational load. The size for executing the optimization is reduced from Nm to N. Though several iterations are needed to obtain the control sequences, the computational load has been dramatically reduced, especially when the number of VGs is large. For each time step optimization, the centralized controller averagely takes 1.3 seconds. With the proposed DMPC, having $p_{max} = 5$, $N_i = 10$, it takes no more than 0.5 second to obtain the optimal control sequence. Thus, the proposed DMPC scheme can fully satisfy the time scale of the primary frequency control.

Remark 4.4: The number of state bins N_i also affects the service performance in terms of the modeling accuracy. With less state bins, the temperature range for each state bin becomes larger, which results in an inaccurate classification; with more state bins, the temperature range of each state bin becomes too narrow to involve a reasonable number of TCAs and the calculation of migration probabilities in $\mathscr{A}(k)$ may encounter computational error. We conducted a parametric study in terms of N_i and found out that, the number of state bins versus normed tracking error was a U-shape curve whose minimum value was at around $10 - 20$. After 20, the error increased exponentially. ■

4.4 Optimal Control Design

The previous section discusses the design of a DMPC scheme, showing a promising regulation performance. However, as reviewed in Section 4.1, the predictive control scheme may encounter the problem of lacking regulation signal predictions. Hence, in this section, we shall present an optimal control scheme, which has no requirements on the regulation signal predictions. The derivations is step-by-step induced by a centralized MPC design.

4.4.1 Centralized MPC

Continuously using the population-based model (4.6) proposed in Section 4.2 and given that the prediction horizon is N, then along the prediction horizon, the system state, input, and output can be augmented as

$$\begin{aligned}
\mathbf{X}(k) &= \left[\mathscr{X}(k+1|k)^{\mathsf{T}}\ \mathscr{X}(k+2|k)^{\mathsf{T}}\ \cdots\ \mathscr{X}(k+N|k)^{\mathsf{T}}\right]^{\mathsf{T}},\\
\mathbf{U}(k) &= \left[\mathscr{U}(k|k)^{\mathsf{T}}\ \mathscr{U}(k+1|k)^{\mathsf{T}}\ \cdots\ \mathscr{U}(k+N-1|k)^{\mathsf{T}}\right]^{\mathsf{T}},\\
\mathbf{Y}(k) &= \left[y(k|k)\ y(k+1|k)\ \cdots\ y(k+N-1|k)\right]^{\mathsf{T}},
\end{aligned}$$

where $\mathscr{X}(k+i|k)$, $\mathscr{U}(k+i|k)$, and $y(k+i|k)$ are the predictions of $\mathscr{X}(k+i)$, $\mathscr{U}(k+i)$, and $y(k+i)$ based on the knowledge of $\mathscr{X}(k|k)$. Consequently, in the MPC fashion, the system dynamics can be written as

$$\begin{aligned}
\mathbf{X}(k) &= \mathcal{M}(k)\mathscr{X}(k) + \mathcal{C}(k)\mathbf{U}(k),\\
\mathbf{Y}(k) &= \mathcal{N}(k)\mathscr{X}(k) + \mathcal{D}(k)\mathbf{U}(k),
\end{aligned}$$

where

$$\begin{aligned}
\mathcal{M}(k) &= \begin{bmatrix} \mathbf{I} \\ \mathscr{A}(k) \\ \mathscr{A}(k+1)\mathscr{A}(k) \\ \vdots \\ \prod_{i=2}^{N} \mathscr{A}(k+N-i) \end{bmatrix},\\
\mathcal{N}(k) &= \operatorname{diag}\{\mathscr{C}\} \times \mathcal{M}(k),\\
\mathcal{C}(k) &= \begin{bmatrix} \mathbf{0} & \mathbf{0} & \mathbf{0} & \cdots & \mathbf{0} \\ \mathscr{B}(k) & \mathbf{0} & \mathbf{0} & \cdots & \mathbf{0} \\ \mathscr{A}(k+1)\mathscr{B}(k) & \mathscr{B}(k+1) & \mathbf{0} & \cdots & \mathbf{0} \\ \vdots & \vdots & \ddots & \ddots & \vdots \\ \prod_{i=2}^{N-1} \mathscr{A}(k+N-i)\mathscr{B}(k) & \prod_{i=2}^{N-2} \mathscr{A}(k+N-i)\mathscr{B}(k+1) & \cdots & \mathscr{B}(k+N-1) & \mathbf{0} \end{bmatrix},\\
\mathcal{D}(k) &= \operatorname{diag}\{\mathscr{C}\} \times \mathcal{C}(k) + \operatorname{diag}\{\mathscr{D}\}.
\end{aligned}$$

The design objective is to use the aggregated TCA power consumption to track the desired trajectory. Thus, along the prediction horizon, the objective function can be represented as

$$\mathcal{J}_c(k) = \|\mathbf{Y}(k) - \mathbf{Y}_0(k)\|_{\mathcal{P}} + \|\mathbf{U}(k)\|_{\mathcal{Q}} + \|\mathbf{X}(k)\|_{\mathcal{H}}, \tag{4.50}$$

where $\mathbf{Y}_0(k) = [y_0(k)\ y_0(k+1)\ \cdots\ y_0(k+N-1)]^{\mathsf{T}}$ is the desired trajectory along the prediction horizon; $\mathcal{P}$, $\mathcal{Q}$, and $\mathcal{H}$ are the weighting matrices for the tracking performance, control signal penalty, and reduction of temperature limit violations, respectively. $\|\mathbf{X}(k)\|_{\mathcal{H}}$ exists to steer TCAs away from the boundary temperature bins. $\mathcal{H}$ can be selected as a diagonal matrix with elements corresponding to boundary temperature bins being large and other elements being relatively small. Suppose the desired trajectory can be predicted, then the optimal control sequence along the prediction horizon can be obtained by solving

$$\begin{aligned} \mathbf{U}^*(k) = \arg\min_{\mathbf{U}(k)}\ & (4.50) \\ \text{s.t.}\quad & \mathbf{0} \leq \mathbf{U}(k) \leq \mathbf{1}, \\ & \mathbf{0} \leq \mathbf{X}(k) + \operatorname{diag}\{\mathcal{B}\} \times \mathbf{U}(k) \leq \mathbf{1}. \end{aligned} \tag{4.51}$$

Herein, in an elementary form, the second constraint can be written as

$$0 \leq x_{\imath,0,\jmath}(k) - u_{\imath,0,\jmath}(k) \leq 1, \tag{4.52}$$

$\forall \imath = 1, \ldots, N_i/2,\ \jmath = \{0, 1\}$, which is to guarantee the controller not switching more than the available number of TCAs in the corresponding state bins. Once the optimal control sequence is obtained, only the first element, i.e., $\mathscr{U}^*(k|k)$, is broadcasted to all TCAs.

4.4.2 Optimal Control

The above described centralized MPC scheme possesses the feature of prediction and pre-adjustment. However, the predictions of regulation signals are usually not available. This inspires us to design an optimal controller by only involving the current regulation signal without any predictions.

4.4.2.1 Downgraded Centralized MPC

First we consider a downgraded MPC controller with $N = 1$. Then the objective function in (4.50) becomes

$$\mathcal{J}_o(k) = \|y(k) - y_0(k)\|_{\mathcal{P}} + \|\mathscr{U}(k)\|_{\mathcal{Q}} + \|\mathscr{X}(k+1|k)\|_{\mathcal{H}}. \tag{4.53}$$

Consequently, $\mathscr{U}^*(k)$ can be obtained by solving

$$\begin{aligned} \mathscr{U}^*(k) = \arg\min_{\mathscr{U}(k)} \ & (4.53) \\ \text{s.t.} \quad & \mathbf{0} \leq \mathscr{U}(k) \leq \mathbf{1}, \\ & \mathbf{0} \leq \mathscr{X}(k) + \mathcal{B}\mathscr{U}(k) \leq \mathbf{1}. \end{aligned} \tag{4.54}$$

It is obvious that, the performance of this downgraded MPC controller cannot be comparable with that of a long-horizon MPC controller, for the latter one takes the future possible situations into consideration. Without involving possible future situations, the optimal solution at k may have a good performance at time k yet a bad performance at $k + i$. Thus, on the one hand, we are forced to use the current regulation signal only; on the other hand, it is necessary to preserve the feature of prediction and pre-adjustment. Inspired by this, we introduce a term *regulation capacity* which represents the system's relative capability of providing the regulation service.

4.4.2.2 Regulation-Capacity-Based Optimal Control

Define the regulation capacity $\wp(k)$ at time k as

$$\wp(k) \triangleq \left\| \mathscr{X}_0(k+1|k) \right\|_1 , \tag{4.55}$$

where

$$\mathscr{X}_0(k+1|k) \triangleq \left[\mathbf{x}_{\ell_F,0}(k+1|k)^\mathsf{T} \ \mathbf{x}_{\ell_F,1}(k+1|k)^\mathsf{T} \right]^\mathsf{T}$$

contains all unlocked OFF and ON states, and $\|\cdot\|_1$ stands for 1-norm. Suppose the aggregated power consumption before any switching actions at time k is $P_{agg}(k)$, then the highest and lowest possible aggregated power consumption after the switching actions at time $k+1$ can be calculated as

$$\begin{aligned} \overline{P}_{agg}(k) &= P_{agg}(k) + P\nu \left\| \mathbf{x}_{\ell_F,0}(k+1|k) \right\|_1 , \\ \underline{P}_{agg}(k) &= P_{agg}(k) - P\nu \left\| \mathbf{x}_{\ell_F,1}(k+1|k) \right\|_1 , \end{aligned} \tag{4.56}$$

respectively. Thus, $\wp(k)$ constructs a tube of the aggregated power consumption. The wider the tube is, the larger regulation flexibility the system has. Therefore, one more potential way to preserve the regulation capacity is to maximize $\wp(k)$ while minimizing the error between the aggregated power consumption and the desired trajectory. Implicitly, we have

$$\max_{\mathscr{U}(k)} \wp(k) \Leftrightarrow \min_{\mathscr{U}(k)} \left\| \mathscr{X}_\ell(k+1|k) \right\|_1 , \tag{4.57}$$

where

$$\mathscr{X}_\ell(k+1|k) \triangleq \begin{bmatrix} \mathbf{x}_{\ell_1,0}(k+1|k) \\ \vdots \\ \mathbf{x}_{\ell_{N_0},0}(k+1|k) \\ \mathbf{x}_{\ell_1,1}(k+1|k) \\ \vdots \\ \mathbf{x}_{\ell_{N_1},1}(k+1|k) \end{bmatrix} \tag{4.58}$$

contains all locked OFF and ON states. Then, by integrating (4.57) into (4.53), we have the modified objective function

$$\mathcal{J}_{op}(k) = \|y(k) - y_0(k)\|_{\mathcal{P}} + \|\mathscr{U}(k)\|_{\mathcal{Q}} + \|\mathscr{X}_\ell(k+1|k)\|_{1,\mathcal{R}} + \|\mathscr{X}(k+1|k)\|_{\mathcal{H}}, \tag{4.59}$$

where $\mathcal{R}$ is the weighting scalar for the flexibility penalty. As a result, the improved optimal control signal $\mathscr{U}^*(k)$ can be obtained by solving

$$\begin{aligned} \mathscr{U}^*(k) &= \arg\min_{\mathscr{U}(k)} \ (4.59) \\ \text{s.t.} \quad & \mathbf{0} \le \mathscr{U}(k) \le \mathbf{1}, \\ & \mathbf{0} \le \mathscr{X}(k) + \mathcal{B}\mathscr{U}(k) \le \mathbf{1}. \end{aligned} \tag{4.60}$$

Compared to the centralized MPC, the controller obtained from (4.60) overcomes the barrier of unpredictability of the regulation signal but possesses the same feature of preserving the regulation capacity.

4.4.3 Control Signal Implementation

At time k, the procedure to obtain and to implement the optimal control signal can be briefly described as

Step 1 Collect the current states $\mathscr{X}(k|k)$ from all state bins. Then solve the optimal control problem in (4.51), (4.54), or (4.60) to obtain $\mathscr{U}^*(k)$.

Step 2 Without considering the lockout effect, TCAs with air temperature below(above) $\underline{T}_i(\overline{T}_i)$ are forced to switch ON(OFF). The number of switchings of this type of TCAs falls into the state bins with the same temperature range.

Step 3 Apply the rest of $\mathscr{U}^*(k)$ on each controllable state bin. Uncontrollable TCAs evolve naturally.

4.4.4 Case Study

The case study is conducted by adopting the same TCA parameter setup as in Section 4.3.4. The comfort temperature range for end-users is ±2°C around 21°C. The lockout time step for both the ON and OFF is 30, i.e., 2 minutes. $N_i = 10$ is set for the aggregation model and a 40-second prediction horizon is set for the centralized MPC controller. Weighting matrices and scalars are chosen as $\mathcal{P} = \mathbf{I}$, $\mathcal{Q} = P\mathbf{I}$, $\mathcal{R} = P\nu$, and $\mathcal{H} = P\text{diag}\{h\}$, where

$$h = \begin{bmatrix} 1 & & \\ & 0.1\mathbf{I} & \\ & & 1 \end{bmatrix} \in \mathbb{R}^{\frac{N_i}{2}\times\frac{N_i}{2}}.$$

Herein, $\text{diag}\{h\}$ expands h to appropriate dimensions according to $\mathbf{X}(k)$ and $\mathscr{X}(k+1|k)$. The test regulation signal is taken from the PJM website [99].

The indoor air temperature of 1000 end-users is initialized to be randomly distributed in $[19, 23]$°C. Temperature evolutions of all end-users by adopting the three proposed controllers are shown in Figure 4.5. It can be readily observed that, by implementing three different controllers, though the individual behaviors are different, the indoor air temperature is well restricted within the preset comfort zone. How-

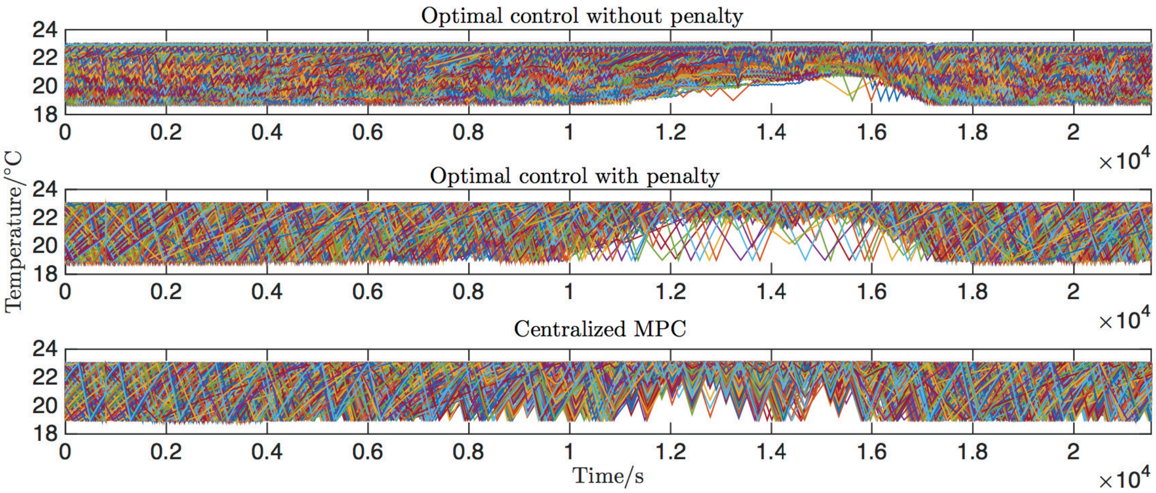

Figure 4.5: Temperature evolution by employing three different controllers.

ever, the centralized MPC has a slightly better temperature control than the other two optimal controllers in terms of a more diversified temperature profile and less temperature limit violations. In addition, penalty $\|\mathbf{X}(k)\|_{\mathcal{H}}$ or $\|\mathscr{X}(k+1|k)\|_{\mathcal{H}}$ can effectively reduce the possibility of temperature limit violations. To make it clear, without this term, the percentage of violations of the above three cases are 3.37%, 0.73%, and 0.33%, respectively; with this term added, those values are reduced to 2.18%, 0.56%, and 0.28%, respectively.

The regulation capacity tube discussed in Section 4.4.2.2 can be shown in Figure 4.6. The black dashed line is the desired trajectory. It can be readily observed that the desired trajectory P_d almost overlaps and, in most cases, goes above the brown dotted line which is the upper bound of the regulation capacity of the optimal controller without the flexibility penalty. These overlaps and exceedings severely impair the regulation performance for the system cannot provide a big enough room for the desired trajectory to vary within. The tracking error of this controller can be observed from Figure 4.7 (brown dotted line). Along a whole day service, compared to the other two controllers, the tracking error of the optimal controller without flexibility penalty has the largest average error, which is 0.09 MW.

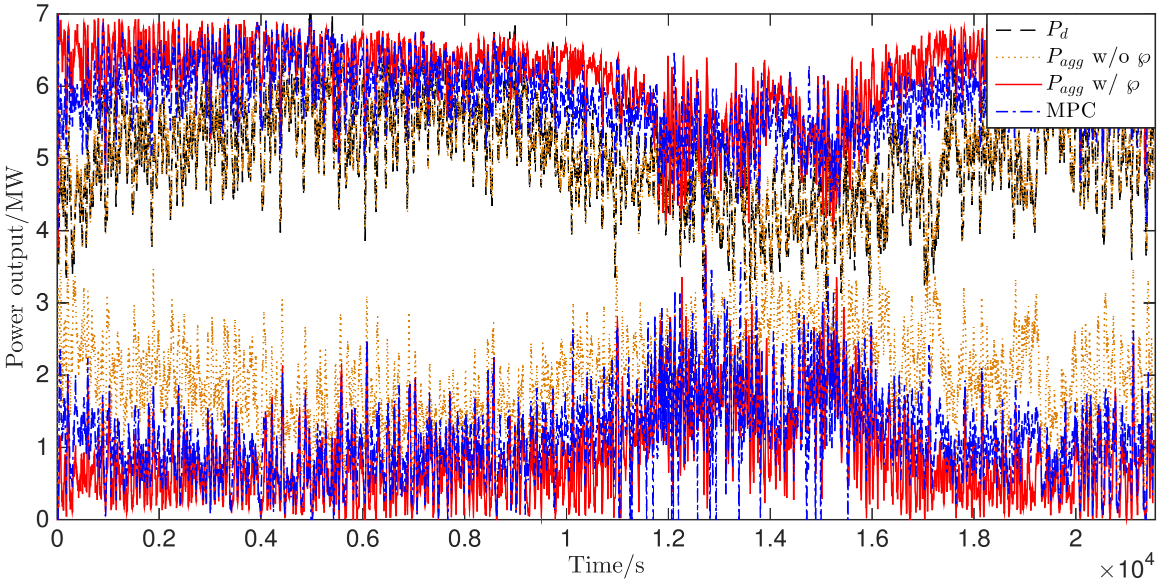

Figure 4.6: Regulation flexibility of three controllers.

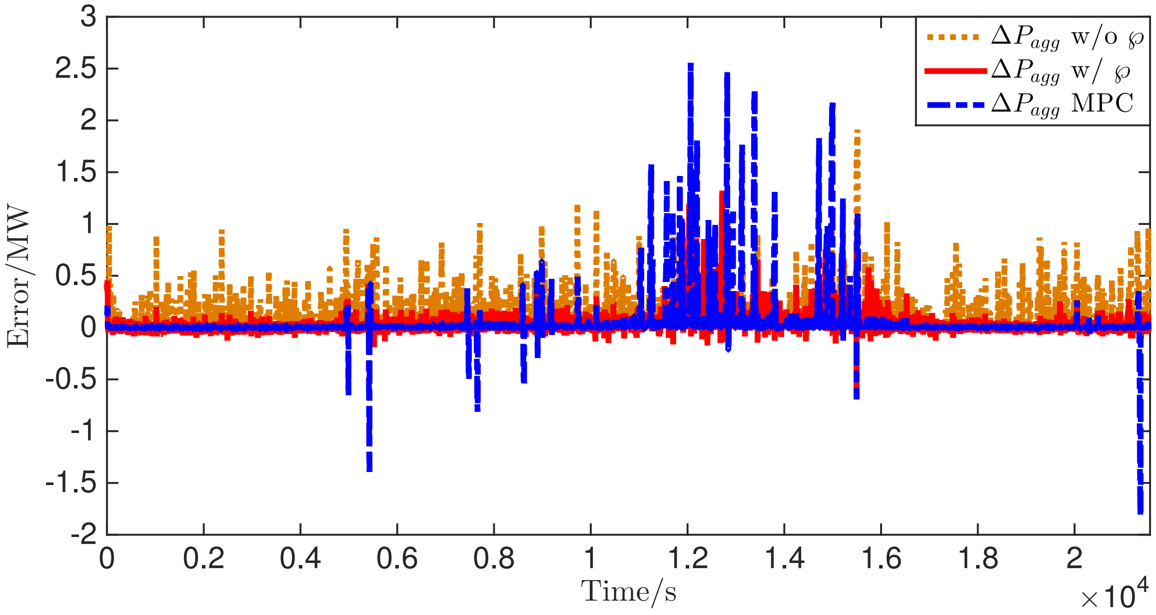

Figure 4.7: Tracking error of three controllers.

It can be observed from Figure 4.6 that the blue dot dashed lines constructed a wider tube which provides a bigger room for the desired trajectory. From Figure 4.7, compared to the other two, the tracking error of the MPC controller stays relatively small in most cases. The average error is approximately 0.04 MW. However, in some special cases, the error is as high as 2.5 MW which is over the regulation capacity. This is due to the relatively short prediction horizon and the extreme weather at those points. Because of those large errors, the relative normed error of the MPC controller is 4.12%.

When implementing the optimal controller with $\wp(k)$ included, from Figure 4.6, we can see that the tube is even enlarged compared to the MPC controller. Because of the adding of $\wp(k)$, those 1000 TCAs provide a much wider tube which allows an even higher-amplitude regulation signal. From Figure 4.7, the tracking error is relatively flat and slightly jittering around 0. The average error is 0.046 MW, which is nearly half of the one of the optimal controller without $\wp(k)$, however slightly higher than the MPC controller nevertheless without any spike. When computing the relative normed error, the optimal controller with $\wp(k)$ has the lowest value 2.31% compared with 4.12% of the MPC controller, and 3.73% of the optimal controller without $\wp(k)$.

Overall, the proposed optimal controller with $\wp(k)$ can drive the system track the regulation signal with relatively small errors due to the feature of regulation capacity preservation. In addition, it is suitable for practical applications since on the one hand, it does not require any prediction of the regulation signal; on the other hand, the computational load is relatively low compared with the centralized MPC controller. The time elapsed for one time step computation is around 0.001 second, which is suitable for primary frequency control.

4.5 Conclusions

In this chapter, an improved population-based model for the aggregation of heterogeneous TCAs is proposed. Lockout effect is explicitly described in the new aggregation model, thus the control signal mismatch caused by the lockout effect can be eliminated. Detailed analytical derivations of the time-varying jumping matrices are provided. As a compensation for the additional state bins, a DMPC scheme is proposed. An additional flexibility penalty is developed for the optimization problem in order to increase the regulation flexibility. Furthermore, to consider the worst case that predictions of regulation signals are not available, an optimal control scheme is investigated. A regulation capacity term is proposed and added to the objective function to compensate for the control scheme. The optimal control scheme also requires low computational effort. Results of case studies verify the effectiveness of the proposed aggregation model and controllers. The optimal control scheme has a comparable tracking performance as the predictive one.

Chapter 5

Aggregation and Charging Control of PHEVs in Smart Grid: A Cyber-Physical Perspective

5.1 Introduction

5.1.1 Background and Literature Review

PHEVs and other types of electric vehicles (EVs) are proved to be effective in increasing energy conversion efficiency and reducing GHG emissions by relieving the usage of fossil-based fuel [72, 104, 105]. From 2013 to 2014, the market share of PHEVs and EVs presented a significant growth in most countries [106, 107]. This growth is no doubt a sign that global social awareness of reducing GHG emissions has been raised. However, apart from the benefits, some challenges arise naturally when integrating PHEVs into power grid: An intensive full-power charging of a large population of PHEVs may elevate the existing demand peak or create new peaks [108]; the stochastic charging patterns of various drivers bring huge uncertainties to the demand side of power grid, which may deviate the power frequency, overload distribution network devices, and increase power loss [109, 110].

As surveyed in Chapter 1, currently there are intensive discussions on the potential of utilizing the charging process of a large population of PHEVs to mitigate the integration impact on grid and to provide ancillary services. Regardless of the various integration modes and purposes, all architectures are established based on advanced metering infrastructures, two-way digital communication networks, physical electricity transmission networks, and embedded computing systems. In other words, the PHEV charging control network constructs a typical cyber-physical system (CPS)–smart grid. CPS is an amalgamation of computational and physical properties [111], of industrialization and informatization, and of individual and network. By using different types of sensors, CPS connects physical devices together and exchanges information among them via the network, thus realizing a smart coordination. In smart grid, through constructing local aggregators and applying CPS techniques, information of PHEVs is collected and processed in the cyber space, and the charging processes are appropriately coordinated in the physical space.

Among all DR service types, studies in a large amount of literature indicate that the best way PHEVs could serve the grid is to fill the overnight load valley, where the non-PHEV electricity is at its lowest [77, 112]. By filling the valley, on the one hand, PHEVs could be charged during the night without causing any inconvenience; on the other hand, the daily operations of power plants and associated cost could be reduced [113]. Currently, utilizing PHEVs to gain the provision of valley-filling has attracted increasing attention. Ma *et al.* [114] proposed a decentralized model predictive control (MPC) strategy for valley-filling based on Nash Games. They further proved the existence of the uniqueness of the Nash equilibrium in [112]. Gan *et al.* [108] developed an optimal decentralized control protocol to realize valley-filling.

The developed algorithm converges to an optimal charging profile for each individual PHEV, thus communication and computational loads of centralized controllers can be relieved. Though the aforementioned decentralized control schemes present promising control performance, they eventually lack centralized monitoring and global management. It is recognizable that the main motivation for the aforementioned literature adopting decentralized control is to consider the large centralized computational load when the number of PHEVs arises. However, the possible heavy computational load in the cyber space is due to the lack of tractable aggregation models which can accurately estimates the running status of individual or grouped PHEVs and allows the design of efficient centralized controllers.

As surveyed in Chapter 1, the study of PHEV charging process aggregation is still in an early stage and many problems remain open. In [75, 76], the proposed aggregation models are essentially stacking models, which still encounter the issue of heavy computational load. Kundu and Hiskens [77] developed a linear state-space aggregation model based on the steady-state probability distributions of chargers in ON and OFF status. A feedback controller is designed based on this model to control the battery SOC deadband. In [78], the authors developed an average battery charging model based on the participation factor of each PHEV. Bashash and Fathy [79] proposed a collective charging scheme for homogeneous PHEVs. This scheme presents the migration dynamics of PHEVs in different SOC levels. A sliding mode control scheme is developed based on this collective model. The aforementioned approaches share one common feature that they are all constructed based on the vehicle SOC information, and one common drawback that the heterogeneity is not fully considered. In practical applications, the heterogeneity presents in the forms of heterogeneous charging dynamics and heterogeneous charging requirements: Individual charging dynamics are determined by various charging stalls, batteries, etc.; individual charging requirements, i.e., by what time the vehicle must be fully charged, are decided by various drivers. In the literature, the first heterogeneity is widely studied, however, the second one is barely touched since the time information is difficult to include. Therefore, it is urged to establish an aggregation model that is centralized-control-oriented and could comprehensively capture both the heterogeneity.

For the control strategy design, MPC [83] has been proved to be successful in many industrial applications for numerous technical constraints can be included in the optimal controller design. In this chapter, a centralized MPC strategy will be investigated for the provision of valley-filling via controlling the PHEV charging processes.

5.1.2 Research Objectives and Contributions

Motivated by the aforementioned points, the design objectives and contributions of this chapter is in three-fold:

- A novel concept of *charging requirement index* is proposed. Being processed in the embedded systems of charging stalls, these indices convey the information of both the battery SOC and drivers' charging requirements.

- Based on the *charging requirement index*, a new PHEV aggregation model is developed to serve the entire cyber space. This model describes the PHEV population migration among different *index* ranges. Since only the *index* information needs to be transmitted to the local aggregator, communication load of the proposed framework is extremely low.

- A nonlinear MPC (NMPC) scheme is studied to obtain the charging rates for PHEVs with different *indices*. Since not associated with the PHEV population size, computational load for the aggregator is extremely low.

5.1.3 Chapter Organization

The rest of this chapter is organized by following the normal CPS design procedure as follows. Section 5.2 presents the physical battery charging dynamics and analytical derivations of the cyber-space aggregation model, followed by a verification against Monte Carlo simulations. In Section 5.3, the control scheme is formulated and the detailed implementation procedure is presented. A case study is conducted in Section 5.4 to verify the valley-filling control performance. Section 5.5 concludes this chapter.

5.2 Aggregation Model Development

5.2.1 PHEV Battery Charging Model

In this chapter, the 1st-order battery charging dynamics is adopted for a single PHEV as [112]

$$\Theta^{+} = \Theta + \frac{a}{b}\nu \Delta t, \tag{5.1}$$

where Θ is the battery SOC at the current time, Θ^{+} is the SOC in the successive time instant, a is the charger efficiency, b is the battery capacity normalized by the rated charging power, ν is the charging rate varying within $[0, 1]$, and Δt is the discrete time step.

5.2.2 Charging Requirement Index

To inherently include the heterogeneous charging deadlines in the aggregation model, we define a novel concept – *charging requirement index* (*index* for short), to represent the completion level of charging. Specifically, for the $\imath$th PHEV, the index is defined as

$$\rho_{\imath} \triangleq \frac{\phi_{\imath}}{\psi_{\imath}}, \tag{5.2}$$

where $\phi_\imath$ represents the remained charging time of the $\imath$th PHEV given that it is in the full-power charging mode, i.e., charging rate $\nu_\imath = 1$, and $\psi_\imath$ represents the remained specified charging time by the driver (no matter what $\nu_\imath$ is). Herein, $\phi_\imath$ depends on the current SOC, charger properties, battery properties, and the charging rate, however, $\psi_\imath$ solely depends on the individual driver's charging requirements. For the convenience of derivations, we write the individual charging dynamics as

$$\Theta_\imath^+ = \Theta_\imath + r_\imath \nu_\imath \Delta t, \tag{5.3}$$

where $r_\imath = a_\imath / b_\imath$.

According to the above definitions, we have the following two dynamic evolutions

$$\phi_\imath^+ = \frac{1 - \Theta_\imath^+}{r_\imath}, \tag{5.4}$$

$$\psi_\imath^+ = \psi_\imath - \Delta t. \tag{5.5}$$

Consequently, the successive index can be calculated as

$$\begin{aligned} \rho_\imath^+ &= \frac{\phi_\imath^+}{\psi_\imath^+} \\ &= \frac{(1 - \Theta_\imath - r_\imath \nu_\imath \Delta t)/r_\imath}{\psi_\imath - \Delta t} \\ &= \frac{\phi_\imath - \nu_\imath \Delta t}{\psi_\imath - \Delta t}. \end{aligned} \tag{5.6}$$

It can be readily observed from (5.6) that the evolution of $\rho_\imath$ is also determined by the driver's charging requirements, SOC level, and the battery properties. Thus, by capturing the dynamics of $\rho_\imath$, it is possible to capture all types of heterogeneity, resulting in a more comprehensive design.

Remark 5.1: When a PHEV is plugged in for charging, it immediately implies $\psi_\imath \geq \phi_\imath$. As the charging process goes, there are two special cases:

- $0 = \phi_\imath^+ \leq \psi_\imath^+$: This indicates that the $\imath$th PHEV has been fully charged and no power can be drawn from the grid by this PHEV.

- $0 < \phi_\imath^+ = \psi_\imath^+$: This indicates that, from the successive time instant, the $\imath$th PHEV must be charged in full power. Otherwise, the remained full-power charging time will be lower than the remained specified charging time, leading to a violation of driver's requirements. In this case, the $\imath$th PHEV draws full power from the grid, i.e., maintaining $\nu_\imath^+ = 1$ until $\phi_\imath = 0$. ■

5.2.3 Index-Based Aggregation Model

In this section, we borrow the population-based model and state bin ideas [65,115,116] to construct the aggregate dynamics of a large population of PHEVs. By equally partitioning the domain of ρ into n parts, we have the aggregation model state constructed as

$$\zeta = [\zeta_1 \; \zeta_2 \; \cdots \; \zeta_n]^{\mathsf{T}}. \tag{5.7}$$

Herein,

$$\zeta_i = \frac{\mathcal{I}_{\varrho_i}}{m}, \; \forall i = 1, \ldots, n, \tag{5.8}$$

where m is the total number of PHEVs, $\varrho_i = \left\{\rho_\imath | \frac{i-1}{n} \leq \rho_\imath < \frac{i}{n}, \imath = 1, \ldots, m\right\}$, and $\mathcal{I}_{\varrho_i}$ is the cardinal number of the set ϱ_i. It is worth mentioning that each state element is called a state bin, containing the PHEV population density information. In other words, each state bin contains the portion of the whole PHEV population with a specific range of ρ. To describe the aggregate dynamics, we shall develop a model in the form of

$$\begin{aligned} \zeta^+ &= f(\zeta, u), && (5.9) \\ y &= \zeta^{\mathsf{T}} u m P_{ave}, && (5.10) \end{aligned}$$

where $u = [u_1 \; u_2 \; \cdots \; u_n]^\mathsf{T}$ represents the charging rates for corresponding state bins, y is the current aggregated power consumption estimated by the average rated charging power P_{ave}, and $f(\cdot, \cdot)$ in (5.9) denotes the nonlinear state evolution dynamics.

5.2.4 Analytical Derivation of the System Dynamic Function

The nonlinear function $f(\zeta, u)$ represents the PHEV population migration from ζ to ζ^+ given the charging rate vector u. This migration depends on the charging rates imposed on different state bins. Written in a state-space form, (5.9) becomes

$$\zeta^+ = A(u)\zeta, \tag{5.11}$$

where

$$A(u) = \begin{bmatrix} a_{11}(u) & a_{12}(u) & \cdots & a_{1n}(u) \\ a_{21}(u) & a_{22}(u) & \cdots & a_{2n}(u) \\ \vdots & \vdots & \ddots & \vdots \\ a_{n1}(u) & a_{n2}(u) & \cdots & a_{nn}(u) \end{bmatrix} \in \mathbb{R}^{n \times n}. \tag{5.12}$$

Herein, each element $a_{ij}(u)$, $\forall i, j = 1, \ldots, n$, is a function of the charging rate vector u and it represents the population migration ratio of all PHEVs in bin j to bin i. Since each element in the control signal, i.e., the charging rate u_j, corresponds to all PHEVs in bin j, the migration ratio $a_{ij}(u)$ only depends on u_j, which indicates

$$a_{ij}(u) = a_{ij}(u_j). \tag{5.13}$$

In the following, the detailed derivations of each $a_{ij}(u_j)$ will be provided. The derivation will be proceeded from the simplest scenario to the most complicated but real one.

5.2.4.1 Point-to-Point

This case is to discuss, under what condition, one PHEV will have a certain index evolution from ρ to ρ^+ after Δt. By dropping the PHEV index $\imath$, from (5.6) we have

$$\rho^+ = \frac{\rho\psi - \nu\Delta t}{\psi - \Delta t}, \tag{5.14}$$

which implies

$$\psi = \frac{\rho^+ - \nu}{\rho^+ - \rho}\Delta t. \tag{5.15}$$

Eqn. (5.15) reveals that, any PHEV having index ρ and being charged by rate ν will evolve to have index ρ^+ after Δt, if and only if its value of the remained specified charging time satisfies (5.15). Eqn. (5.15) sets the foundation for later derivations.

5.2.4.2 Range-to-Point

In this case, we study the nature of PHEVs with $\rho \in [\underline{\rho}, \overline{\rho}]$ migrating to a fixed point ρ^+. Since, in the proposed aggregation scheme, the aggregator only processes the state bin information instead of detailed PHEV index information, the PHEV population migration can only be estimated by evaluating a probability, with which all PHEVs in one state bin would migrate to another. Then, according to (5.15), if the probability distribution of ψ is known, the migration probability can be calculated by determining the upper and lower limits of ψ, namely $\underline{\psi}$ and $\overline{\psi}$. Herein, we assume that, for all PHEVs, the remained specified charging time follows $\psi \sim \mathrm{U}[\psi_l, \psi_u]$, and the probability density function is denoted by $p_\psi(\psi)$. Specifically, we have the following scenarios:

- $\nu < \rho^+$: In this scenario, the numerator of (5.15) is positive, thus it is necessary to determine the range of ρ^+ that makes the denominator positive and obtain a positive range of ψ. Three cases will be separately discussed below.

  - $\rho^+ \geq \overline{\rho}$: All ρ^+ satisfying this condition can generate positive ψ. Consequently, $\underline{\psi}$ and $\overline{\psi}$ can be determined as

$$\underline{\psi} = \min\left\{\max\left\{\frac{\rho^+ - \nu}{\rho^+ - \underline{\rho}}\Delta t, \psi_l\right\}, \psi_u\right\}, \tag{5.16}$$

$$\overline{\psi} = \max\left\{\min\left\{\frac{\rho^+ - \nu}{\rho^+ - \overline{\rho}}\Delta t, \psi_u\right\}, \psi_l\right\}. \tag{5.17}$$

    As a result, the probability for all PHEVs with $\rho \in [\underline{\rho}, \overline{\rho}]$ charged by ν evolving to have the index value ρ^+ can be calculated as

$$\Pr_{[\underline{\rho},\overline{\rho}],\rho^+}(\nu) = \int_{\underline{\psi}}^{\overline{\psi}} p_\psi(\psi)\mathrm{d}\psi. \tag{5.18}$$

    For other cases in the Range-to-Point scenario, since the migration probability only depends on $\underline{\psi}$ and $\overline{\psi}$, we only discuss the acquisition of them without mentioning (5.18) hereinafter.

  - $\underline{\rho} < \rho^+ < \overline{\rho}$: Under this condition, only the PHEVs with the index $\rho \in (\underline{\rho}, \rho^+]$ are possible to migrate. The lower limit $\underline{\psi}$ can be obtained by (5.16); while the upper limit $\overline{\psi}$ would be ψ_u when $\rho = \rho^+$.

  - $\rho^+ \leq \underline{\rho}$: This condition makes all possible ψ values negative, indicating $\Pr_{[\underline{\rho},\overline{\rho}],\rho^+}(\nu) = 0$.

- $\nu > \rho^+$: Similar to the previous scenario, the probability calculation is discussed in the following three cases:

  - $\rho^+ > \overline{\rho}$: This condition drives the value of ψ to negative, which directly indicates $\Pr_{[\underline{\rho},\overline{\rho}],\rho^+}(\nu) = 0$.

  - $\underline{\rho} < \rho^+ < \overline{\rho}$: Under this condition, only PHEVs with the index $\rho \in [\rho^+, \overline{\rho})$ are possible to migrate. The lower and upper integral limits can be calculated by

$$\underline{\psi} = \min\left\{\max\left\{\frac{\rho^+ - \nu}{\rho^+ - \overline{\rho}}\Delta t, \psi_l\right\}, \psi_u\right\}, \tag{5.19}$$

$$\overline{\psi} = \psi_u. \tag{5.20}$$

- $\rho^+ \leq \underline{\rho}$: All ρ^+ satisfying this condition can generate positive ψ. Consequently, $\underline{\psi}$ can be determined by (5.19); while $\overline{\psi}$ is calculated as

$$\overline{\psi} = \max\left\{\min\left\{\frac{\rho^+ - \nu}{\rho^+ - \underline{\rho}}\Delta t, \psi_u\right\}, \psi_l\right\}. \tag{5.21}$$

- $\nu = \rho^+$: This condition implies $\rho^+ = \rho$, further implying $\nu = \rho$. Consequently, any PHEV satisfying this condition would be guaranteed to migrate from ρ to ρ^+. However, the probability mass at a specific point is meaningless, which indicates $\Pr_{[\underline{\rho},\overline{\rho}],\rho^+}(\nu) = 0$.

The Range-to-Point discussions are the foundation for the following Range-to-Range derivations.

5.2.4.3 Range-to-Range

Based on the above-described Point-to-Point and Range-to-Point derivations, below we present the procedure of determining elements in $A(u)$. Compared to the procedure in Range-to-Point, in addition to $\rho \in [\underline{\rho}, \overline{\rho}]$, the destination index also falls in $[\underline{\rho^+}, \overline{\rho^+}]$. The essential idea is still to determine the upper and lower integral limits for ψ. Note that the current and successive index ranges are of equal length, i.e., $\overline{\rho} - \underline{\rho} = \overline{\rho^+} - \underline{\rho^+}$. Based on (5.15), we shall also study three different scenarios with thirteen detailed cases as follows. The look-up chart for different cases can be referred to Figure 5.1.

- $\nu \geq \overline{\rho^+}$: According to the positions of $[\underline{\rho}, \overline{\rho}]$, this scenario can be divided into

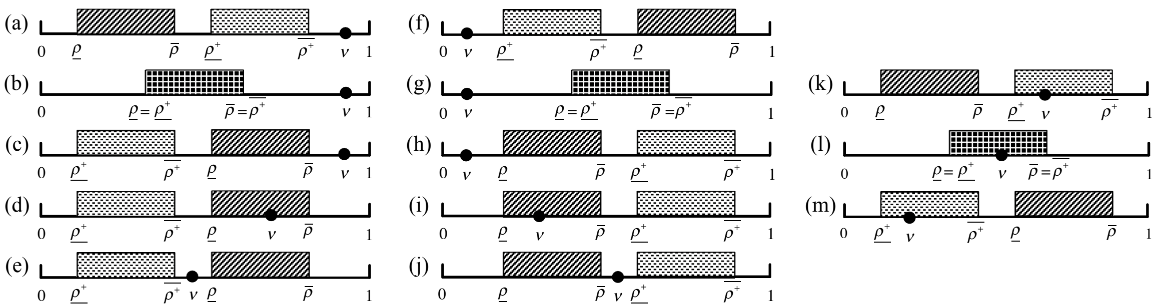

Figure 5.1: Look-up chart for the Range-to-Range derivation of $A(u)$.

five different cases to discuss:

(a) $\overline{\rho} < \overline{\rho^+}$: According to (5.15), under this condition, every combination of ρ and ρ^+ makes the value of ψ negative. Thus, the probability for all PHEVs with $\rho \in [\underline{\rho}, \overline{\rho}]$ jumping to $\rho^+ \in [\underline{\rho^+}, \overline{\rho^+}]$ would be

$$\Pr_{[\underline{\rho},\overline{\rho}],[\underline{\rho^+},\overline{\rho^+}]}(\nu) = 0. \tag{5.22}$$

(b) $\overline{\rho} = \overline{\rho^+}$: In this case, for a fixed ρ, only with $\rho^+ \in [\underline{\rho^+}, \rho]$, the calculated value of ψ can be positive and be possible to be within $[\psi_l, \psi_u]$. The lower integral limit is obtained when $\rho^+ = \underline{\rho^+}$, indicating that

$$\underline{\psi}(\rho) = \max\left\{\min\left\{\frac{\underline{\rho^+} - \nu}{\underline{\rho^+} - \rho}, \psi_l\right\}, \psi_u\right\}. \tag{5.23}$$

The upper integral limit is obtained when $\rho^+ = \rho$, which results in

$$\overline{\psi}(\rho) = \min\{\infty, \psi_u\} = \psi_u. \tag{5.24}$$

Consequently, the probability for all PHEVs with $\rho \in [\underline{\rho}, \overline{\rho}]$ jumping to

$\rho^+ \in [\underline{\rho^+}, \overline{\rho^+}]$ is calculated as

$$\Pr_{[\underline{\rho},\overline{\rho}],[\underline{\rho^+},\overline{\rho^+}]}(\nu) = \int_{\underline{\rho}}^{\overline{\rho}} p_\rho(\rho) \int_{\underline{\psi}(\rho)}^{\overline{\psi}(\rho)} p_\psi(\psi)\mathrm{d}\psi\mathrm{d}\rho, \tag{5.25}$$

where $p_\rho(\rho)$ is the probability density function of the distribution of ρ within $[\underline{\rho}, \overline{\rho}]$. For other cases in the Range-to-Range scenario, since the probability only depends on $\underline{\psi}(\rho)$ and $\overline{\psi}(\rho)$, we only discuss the acquisition of them without mentioning (5.25) hereinafter.

(c) $\overline{\rho^+} < \overline{\rho} < \nu$: Under this condition, the lower integral limit $\underline{\psi}(\rho)$ can be obtained by (5.23); while the upper integral limit is calculated by taking $\rho^+ = \overline{\rho^+}$, which results in

$$\overline{\psi}(\rho) = \min\left\{\max\left\{\frac{\overline{\rho^+} - \nu}{\overline{\rho^+} - \rho}, \psi_u\right\}, \psi_l\right\}. \tag{5.26}$$

(d) $\overline{\rho^+} \leq \underline{\rho} < \nu < \overline{\rho}$: In this case, since the calculations of $\underline{\psi}(\rho)$ and $\overline{\psi}(\rho)$ depend on the relationship between ν and ρ, it is necessary to integral the probability by considering $\underline{\psi}(\rho)$ and $\overline{\psi}(\rho)$ piece-wisely. For a fixed ρ satisfying $\rho \leq \nu$, it can be readily verified that the limit calculations can exactly follow (5.23) and (5.26); however, $\rho \in (\nu, \overline{\rho}]$ leads to

$$\begin{aligned} \underline{\psi}(\rho) &= \max\left\{\min\left\{\frac{\overline{\rho^+} - \nu}{\overline{\rho^+} - \rho}, \psi_l\right\}, \psi_u\right\}, & (5.27) \\ \overline{\psi}(\rho) &= \min\left\{\max\left\{\frac{\underline{\rho^+} - \nu}{\underline{\rho^+} - \rho}, \psi_u\right\}, \psi_l\right\}. & (5.28) \end{aligned}$$

(e) $\overline{\rho^+} \leq \nu \leq \underline{\rho}$: In this case, calculations of the lower and upper limits can fully follow (5.27) and (5.28), respectively.

- $\nu \leq \underline{\rho^+}$: Similarly, the determination of integral limits is divided into five different cases to discuss:

(f) $\overline{\rho^+} < \overline{\rho}$: Every combination of ρ and ρ^+ under this condition leads to a negative ψ value. Thus, the probability for all PHEVs with $\rho \in [\underline{\rho}, \overline{\rho}]$ jumping to $\rho^+ \in [\underline{\rho^+}, \overline{\rho^+}]$ is 0.

(g) $\overline{\rho^+} = \overline{\rho}$: For a fixed ρ, only with $\rho^+ \in [\rho, \overline{\rho^+}]$, the calculated value of ψ can be positive and is possible to be within $[\psi_l, \psi_u]$. The lower integral limit would be obtained by (5.27); the upper limit is determined when $\rho^+ = \rho$, generating $\overline{\psi}(\rho) = \psi_u$.

(h) $\nu \leq \underline{\rho} < \underline{\rho^+}$: The calculation exactly follows the procedure in Case (e).

(i) $\underline{\rho} < \nu < \overline{\rho} < \overline{\rho^+}$: Similar to Case (d), it is necessary to piece-wisely determine $\underline{\psi}(\rho)$ and $\overline{\psi}(\rho)$. For a fixed ρ which satisfies $\rho \leq \nu$, the calculations can exactly follow (5.23) and (5.26); however, when ρ varies within $(\nu, \overline{\rho}]$, the calculations would follow (5.27) and (5.28).

(j) $\overline{\rho} \leq \nu \leq \underline{\rho^+}$: The calculation exactly follows the procedure in Case (c).

- $\underline{\rho^+} < \nu < \overline{\rho^+}$: According to the positions of the range $[\underline{\rho}, \overline{\rho}]$, the determination of integral limits is divided into three different cases:

(k) $\overline{\rho} < \overline{\rho^+}$: According to (5.15), the lower integral limit takes the value when $\rho^+ = \nu$, which implies

$$\underline{\psi}(\rho) = \max\{0, \psi_l\} = \psi_l. \tag{5.29}$$

The upper integral limit would be obtained when $\rho^+ = \overline{\rho^+}$, which follows (5.26).

(l) $\overline{\rho} = \overline{\rho^+}$: Similar as Case (d) and Case (i), it is necessary to determine $\underline{\psi}(\rho)$ and $\overline{\psi}(\rho)$ piece-wisely according to the relationship between ν and ρ. It is worth mentioning that, no matter what the relationship is, $\underline{\psi}(\rho)$ is always ψ_l. When $\underline{\rho} \leq \rho \leq \nu$, $\overline{\psi}(\rho)$ follows (5.28); when $\nu < \rho \leq \overline{\rho}$, $\overline{\psi}(\rho)$ follows (5.26).

(m) $\overline{\rho^+} = \overline{\rho}$: In this case, $\underline{\psi}(\rho)$ also takes value of ψ_l when $\nu = \rho^+$; the calculation of $\overline{\psi}(\rho)$ follows (5.28).

5.2.4.4 Bridging to $A(u)$

When determining elements $a_{ij}(u_j)$, we shall adopt the Range-to-Range approach described in Section 5.2.4.3. Specifically, for any $a_{ij}(u_j)$, j corresponds to the starting index range $[\underline{\rho}, \overline{\rho}]$, where

$$\begin{aligned} \underline{\rho} &= \frac{j-1}{n}, \\ \overline{\rho} &= \frac{j}{n}, \end{aligned} \tag{5.30}$$

and i corresponds to the destination index range $[\underline{\rho^+}, \overline{\rho^+}]$, where

$$\begin{aligned} \underline{\rho^+} &= \frac{i-1}{n}, \\ \overline{\rho^+} &= \frac{i}{n}. \end{aligned} \tag{5.31}$$

Consequently, we have the elements determined by

$$a_{ij}(u_j) = \Pr_{i,j}(u_j). \tag{5.32}$$

5.2.4.5 Curve-Fitting of $A(u)$

It can be readily observed from the above analytical derivations that, each function $a_{ij}(u_j)$ in $A(u)$ is a piece-wisely continuous function. As a result, the decision variable u_j is intractable to be determined in such a function. In order to facilitate the optimization-based controller design, we use polynomials to fit $a_{ij}(u_j)$ and generate a smooth $\hat{a}_{ij}(u_j)$. For example, with $n = 10$, the nominal and 4th-order polynomial curve-fitted $a_{55}(u_5)$ can be shown in Figure 5.2. By fitting all $a_{ij}(u_j)$ off-line, each piece-wisely continuous function becomes smooth and 4th-order differentiable. Thus, the piece-wisely continuous $A(u)$ becomes a smooth and differentiable $\hat{A}(u)$, where each element $\hat{a}_{ij}(u_j)$ is a polynomial.

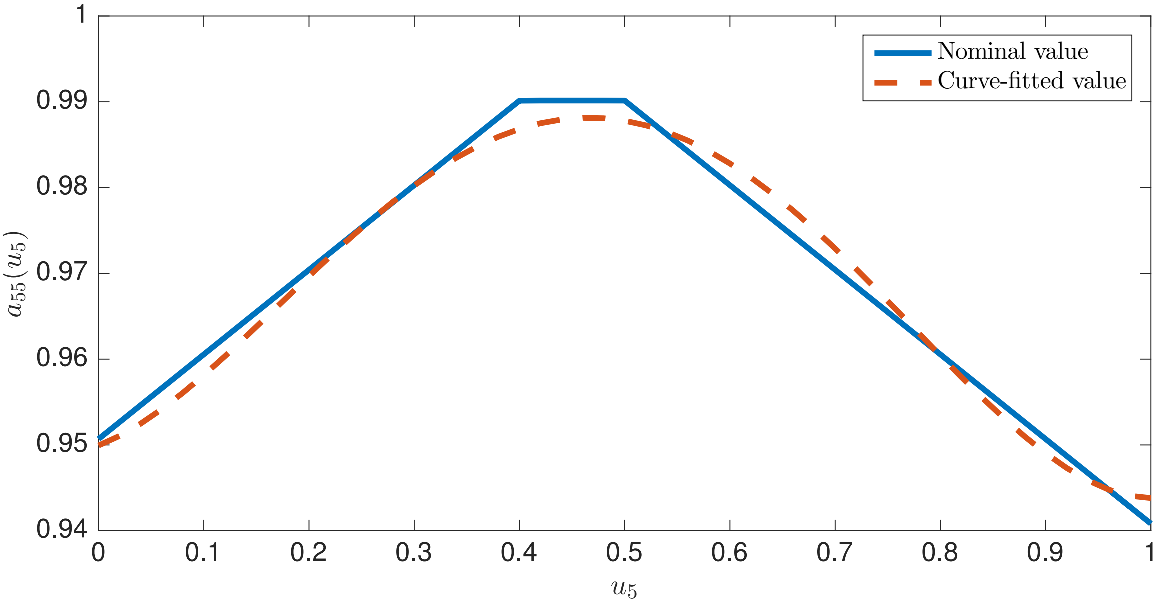

Figure 5.2: 4th-order curve fitting of $a_{55}(u_5)$.

Remark 5.2: In practical applications, to avoid the quantization issue, for the $\imath$th PHEV, we treat its $\rho_\imath$ as 0 when $\rho_\imath \in \left[0, \frac{1}{n}\right]$, and as 1 when $\rho_\imath \in \left[\frac{n-1}{n}, 1\right]$. This treatment indicates that

- Whenever the $\imath$th PHEV enters state bin ζ_1, it can only stay in ζ_1. This implies ζ_1 is an *absorbing* state with $\hat{a}_{11}(u_1) = 1$ and $\hat{a}_{i1}(u_1) = 0$, $\forall i = 2, \ldots, n$. In addition, since ζ_1 contains all fully charged PHEVs, we have $u_1 \equiv 0$.

- Whenever the $\imath$th PHEV enters state bin ζ_n, it can either stay in ζ_n or directly jump to ζ_1. As a result, we have $\hat{a}_{nn}(u_n) + \hat{a}_{1n}(u_n) = 1$ with $\hat{a}_{nn}(u_n) \geq 0$, $\hat{a}_{1n}(u_n) \geq 0$, and $u_n \equiv 1$. Note that, the jumping actions from ζ_n to ζ_1 can neither be captured by the nominal $A(u)$ nor the curve-fitted $\hat{A}(u)$, because those parameters are dependent on SOC, however independent on the control signal. Thus, some amendments need to be made to $\hat{a}_{1n}(u_n)$. This will be elaborated in the following part.

■

5.2.4.6 Model Validation and Amendment

To validate the proposed model and to amend $\hat{a}_{1n}(u_n)$ and $\hat{a}_{nn}(u_n)$, we conducted Monte Carlo simulations. The aim of the Monte Carlo simulations is to verify the fit between the nominal calculated $\hat{A}(u)$ and $\check{A}(u)$ which is identified from real-parameter simulations. By choosing parameters as shown in Table 5.1, the Monte Carlo simulations are executed in MATLAB by following Algorithm 5.1.

Table 5.1: Monte Carlo simulation parameters.

Parameter	Value
Number of PHEVs	$m = 10000$
Average power	$P_{ave} = 3$kW
Number of simulations	$c_{max} = 5000$
Specified charging time	$\psi \sim$ U$[450, 800]$min
Individual indices	$\rho \sim$ U$[0.01, 0.99]$
Full power charging time	Calculated from ψ and ρ
State of charge	$\Theta \sim$ U$[0, 1]$
PHEV charging parameter r	Calculated from SOC and ϕ
Control input step	$\delta_u = 0.02$

Remark 5.3: In Algorithm 5.1, the ordinary least squares (OLS) is adopted to obtain the identified $\bar{A}(u^p)$ row by row. Writing $\bar{A}(u^p)$ in the form of

$$\bar{A}(u^p) = \begin{bmatrix} \bar{A}_1(u^p)^{\mathsf{T}} \\ \vdots \\ \bar{A}_n(u^p)^{\mathsf{T}} \end{bmatrix}, \tag{5.33}$$

Algorithm 5.1 Monte Carlo simulation procedure

```
Control input step number $p = 1$.
procedure
    for $p \leq 1/\delta_u + 1$ do
        Simulation number $c = 1$.
        for $c \leq c_{max}$ do
            Randomly generate $m$ PHEVs according to Table 5.1 and record the state bin information $\zeta_c$.
            Apply $u^p = (p-1)\delta_u \mathbf{1}$ to all PHEVs.
            Record the successive state $\zeta_c^+$.
            $c = c + 1$.
        end for
        Identify $\bar{A}(u^p)$ from $(\zeta_c, \zeta_c^+)$, $c = 1, \ldots, c_{max}$.
        $p = p + 1$.
    end for
    Curve-fit all $\bar{a}_{ij}(u_j)$ to obtain a smooth $\check{a}_{ij}(u_j)$.
end procedure
```

then in the cth simulation, for the ith row, we have

$$\zeta_{ic}^+ = \bar{A}_i(u^p)^\mathsf{T} \zeta_c, \tag{5.34}$$

$\forall c = 1, \ldots, c_{max}$. By adopting the OLS, the best fit $\bar{A}_i^*(u^p)$ can be obtained as follows

$$\begin{aligned} \bar{A}_i^*(u^p) = \arg \min_{\bar{A}_i(u^p)} \sum_{c=1}^{c_{max}} \left\| \zeta_{ic}^+ - \zeta_c^\mathsf{T} \bar{A}_i(u^p) \right\|_2 \\ \text{s.t. } \mathbf{0} \leq \bar{A}_i(u^p) \leq \mathbf{1}, \end{aligned} \tag{5.35}$$

$\forall i = 1, \ldots, n$. ■

Herein, we present a validation example with $n = 10$. Since each column of $A(u) \in \mathbb{R}^n$ is only associated with the corresponding control element u_j, we show the validations column by column in Figure 5.3. Each subfigure shows the function values of $a_{ij}(u_j)$, $\hat{a}_{ij}(u_j)$, $\bar{a}_{ij}(u_j)$, and $\check{a}_{ij}(u_j)$, $i = 1, \ldots, n$, along the corresponding control signal u_j. Solid lines represent the nominal calculated $a_{ij}(u_j)$ and curve-fitted

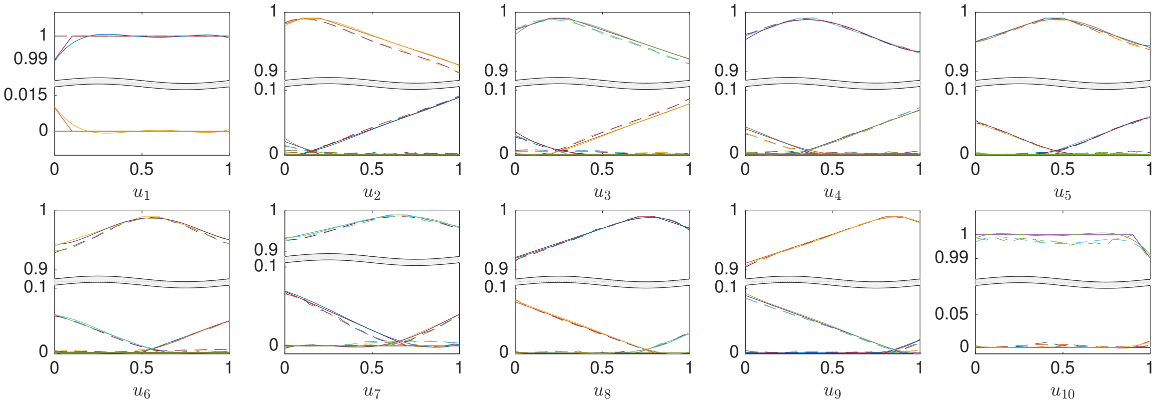

Figure 5.3: Comparisons between the Monte Carlo simulations with the calculated probabilities.

$\hat{a}_{ij}(u_j)$; dashed lines are $\bar{a}_{ij}(u_j)$ and curve-fitted $\check{a}_{ij}(u_j)$ from Monte Carlo simulations. These figures reveal that the proposed probability calculation can well match with the real PHEV population evolution. In addition, as mentioned in **Remark 5.2**, the calculated $\hat{a}_{10\ 10}(u_{10})$ and $\hat{a}_{1\ 10}(u_{10})$ will be replaced by $\check{a}_{10\ 10}(u_{10})$ and $\check{a}_{1\ 10}(u_{10})$, respectively. All of the model parameters will be obtained off-line, thus no extra computational load is needed for the aggregator's real-time computing.

5.3 Controller Design

In this chapter, the control objective is to steer the aggregated charging power of all connected PHEVs to provide overnight valley-filling service. The modeling and control approaches can also be extended to other ancillary services.

5.3.1 Charging Profile

Following [108], we choose per household load profile in the service area of South California Edison from 20:00 on February 13, 2011 to 9:00 on February 14, 2011 as the baseline load profile, which is shown as P_B in Figure 5.4. The basic idea of

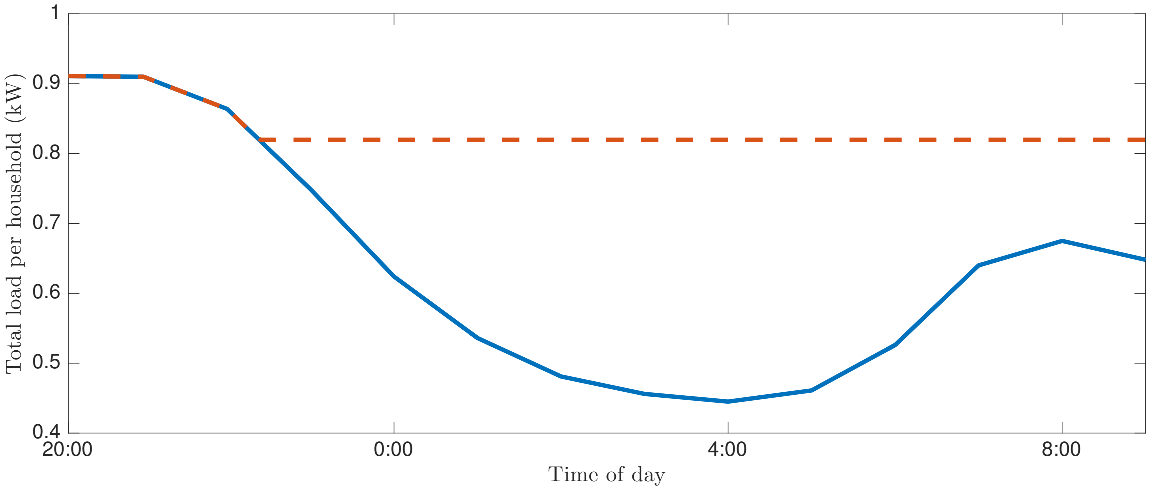

Figure 5.4: Baseline load profile and optimal valley-filling profile per household.

valley-filling is to make use of all available PHEVs' charging power to compensate for the load short when the baseline load profile P_B is lower than the threshold P_t. The dashed line in Figure 5.4 shows the ideal flat load profile, which is the sum of P_B and the aggregated power of PHEVs P_{agg} per household. Thus, the targeting aggregated power consumption at time k can be represented as

$$\hat{P}(k) = \max\left\{0, P_t - P_B(k)\right\}. \tag{5.36}$$

5.3.2 MPC Scheme

In the section, we shall design a centralized MPC scheme to control the charging rates of all PHEVs in different state bins for the purpose of valley-filling. Define the objective function at time k as

$$\mathcal{J}(k) = \sum_{i=0}^{N-1} \left\| y(k+i) - \hat{P}(k+i) \right\|_2 + \sum_{i=1}^{N} \left\| \zeta(k+i) \right\|_Q , \tag{5.37}$$

where Q is the weighting matrix for the 2-norm of $\zeta(k+i)$, and N is the prediction horizon. As mentioned in **Remark 5.2**, to best fulfill customers' charging requirements and to avoid quantization issue, the charging rates for all PHEVs with $\rho_i \in [0, 1/n]$ and with $\rho_i \in [1 - 1/n, 1]$ are 0 and 1, respectively. Consequently, any PHEV in those two state bins are regarded as uncontrollable or having no adjusting flexibility. Thus, it is of significance to suppress the PHEVs' migration to those two state bins. Speaking of that, Q in (5.37) is constructed as

$$Q = \begin{bmatrix} q_{1,1} & & & & & \\ & \ddots & & & & \\ & & q_{\frac{n}{2},\frac{n}{2}} & & & \\ & & & q_{\frac{n}{2}+1,\frac{n}{2}+1} & & \\ & & & & \ddots & \\ & & & & & q_{n,n} \end{bmatrix}, \tag{5.38}$$

where the values of the diagonal elements are descending from $q_{1,1}$ to $q_{\frac{n}{2},\frac{n}{2}}$ and are ascending from $q_{\frac{n}{2}+1,\frac{n}{2}+1}$ to $q_{n,n}$. In the later simulation, we will show the importance of this penalty, especially at the end of the service window.

Since the control signal represents the charging rate, it must satisfy

$$0 \leq u_i(k) \leq 1, \forall i = 1, \ldots, n. \tag{5.39}$$

In addition, from **Remark 5.2**, we have

$$\begin{aligned} u_1(k) &= 0, \\ u_n(k) &= 1. \end{aligned} \tag{5.40}$$

Furthermore, we would like to discuss another important restriction on the control signal. Suppose, for the $\imath$th PHEV, the specified charging time $\psi_\imath$ is large enough to cover the whole service time. Then if $\rho_\imath$ is relatively small, the $\imath$th PHEV could draw sufficiently small amount of power for a sufficiently long time before it is fully charged; if continuously drawing large power, this PHEV will soon be fully charged and then lose the controllability. Similarly, if $\rho_\imath$ is relatively large, the $\imath$th PHEV could draw sufficiently large amount of power for a sufficiently long time before it is fully charged; if continuously drawing small power, this PHEV will soon be forced to draw full power from the grid, resulting in the loss of controllability. Thus, we expect to make use of PHEVs with large ρ first and use ones with smaller ρ to compensate for the rest. By doing so, the service capacity can be continuously preserved. Inspired by this, we have the following ascending constraint for u

$$u_1(k) \leq u_2(k) \leq \ \cdots \ \leq u_n(k). \tag{5.41}$$

Consequently, (5.39) can be discarded because it is inherently included in (5.40) and (5.41).

As a result, the optimal control sequence along the prediction horizon can be obtained by solving

$$\begin{aligned} U^*(k) = \arg \min_{u(k),\ldots,u(k+N-1)} \mathcal{J}(k) \\ \text{s.t. } (5.40) \text{ and } (5.41), \end{aligned} \tag{5.42}$$

where $U^*(k) = \left[u^*(k)^\mathsf{T} \ \cdots \ u^*(k+N-1)^\mathsf{T}\right]^\mathsf{T}$. Once the optimal control sequence $U^*(k)$ is obtained, we only apply the first vector $u^*(k)$ to the corresponding state bins. Note that, problem (5.42) is a nonlinear programming problem.

In the later case study, we shall include another two controllers, i.e., an MPC without penalty on states and a pure optimal tracking controller, as benchmarks to verify the effectiveness of the proposed controller. For convenience, we denote the proposed

MPC with state penalty as Controller #1, denote the MPC without state penalty as Controller #2, and denote the pure optimal controller as Controller #3. Controller #2 is constructed by following Controller #1 and discarding $\sum_{i=1}^{N} \|\zeta(k+i)\|_Q$ in (5.37); Controller #3 is constructed by following Controller #2, shrinking N to 1, and only including (5.38) and (5.39).

5.3.3 Control Signal Implementation

As shown in Figure 1.2, the scheme of controlling a large fleet of PHEVs for valley-filling can be described as

STEP 1 At each discrete time instant, the local aggregator obtains the service signal from the ISO via the communication network.

STEP 2 In the area covered by the local aggregator, chargers in all structures, including workplaces, charging stations, and mostly homes, evaluate the indices of all connected PHEVs from drivers' requirements, SOCs, and battery properties.

STEP 3 Every Δt, chargers send the index information to the local aggregator through the communication link.

STEP 4 The local aggregator aggregates the received information by using (5.9) and (5.10), calculates the control signal by solving (5.42), and then dispatches them to corresponding chargers through the communication network.

STEP 5 According to the dispatched control signal, chargers adjust their charging rate and draw power from the grid to charge PHEVs for the next Δt.

5.4 Case Study

5.4.1 Parameter Selection

In this section, we shall validate the feasibility of the proposed controller by simulations. The simulation parameters can be found in Table 5.2. It is worth mentioning that, parameters in Table 5.2 are sightly different from ones in Table 5.1. For example, in the Monte Carlo simulations, $\rho \sim \text{U}[0.01, 0.99]$, instead, we use $\rho \sim \text{U}[0.35, 0.68]$ in the case study. This is because it is necessary to set ρ to cover all possible values in Monte Carlo simulations, instead, it is more reasonable to shrink that wide range to approximate real-application values in the case study. Similar logics apply to other parameters. By randomly generating 1000 PHEVs according to Table 5.2, we have the distributions of those parameters as shown in Figure 5.5. It can be readily observed from Figure 5.5 that, these distributions closely match the ideal distributions described in Table 5.2. In addition, all generated parameters are close to those employed in real applications, which indicates the case study could be proceeded with the randomly generated parameters.

Table 5.2: Simulation parameters.

Parameter	Value
Number of PHEVs	$m = 1000$
Average rated power	$P_{ave} = 3\text{kW}$
Specified charging time	$\psi \sim \text{U}[450, 800]\text{min}$
Individual indices	$\rho \sim \text{U}[0.35, 0.68]$
Full power charging time	Calculated from ψ and ρ
State of charge	SOC$\sim$ U$[0, 0.5]$
PHEV charging parameter r	Calculated from SOC and ϕ
Number of state bins	$n = 10$
Time step	$\Delta t = 6\text{min}$
Prediction horizon	$N = 5$

As aforementioned, we shall conduct three sets of simulations with Controller #1, Controller #2, and Controller #3. The baseline load profile is scaled to have a peak of

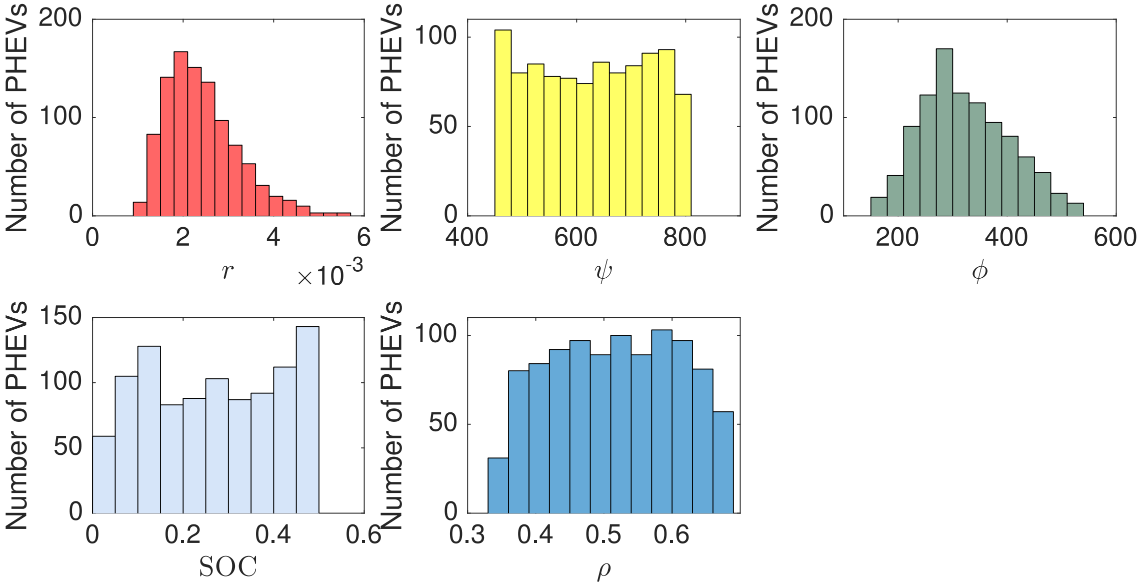

Figure 5.5: Parameter distributions in the case study.

5.46 MW and a bottom of 2.67 MW. The valley-filling threshold is set to be $P_t = 4.92$ MW. The difference between two consecutive hourly load data is linearly fitted by 10 slots, which is corresponding to $\Delta t = 6$ min.

5.4.2 System Performance and Analyses

By applying the three controllers to 1000 PHEVs, the valley-filling performance is shown in Figure 5.6. It can be readily observed that, before 7:00, all of those three controllers can well drive the aggregated power consumption to fill the valley. However, starting from 7:00, P_{agg} generated by Controller #3 starts deviating high from the optimal trajectory; starting from 8:00, P_{agg} generated by Controller #2 starts deviating high from the optimal trajectory. Apparently, the deviation degree of Controller #2 is smaller than that of Controller #3. In contrast, Controller #1 can always perfectly steer P_{agg} to the optimal trajectory. This deviation at the end of the service is due to the following reasons:

- At the beginning of the service, though all PHEVs are already plugged in, there

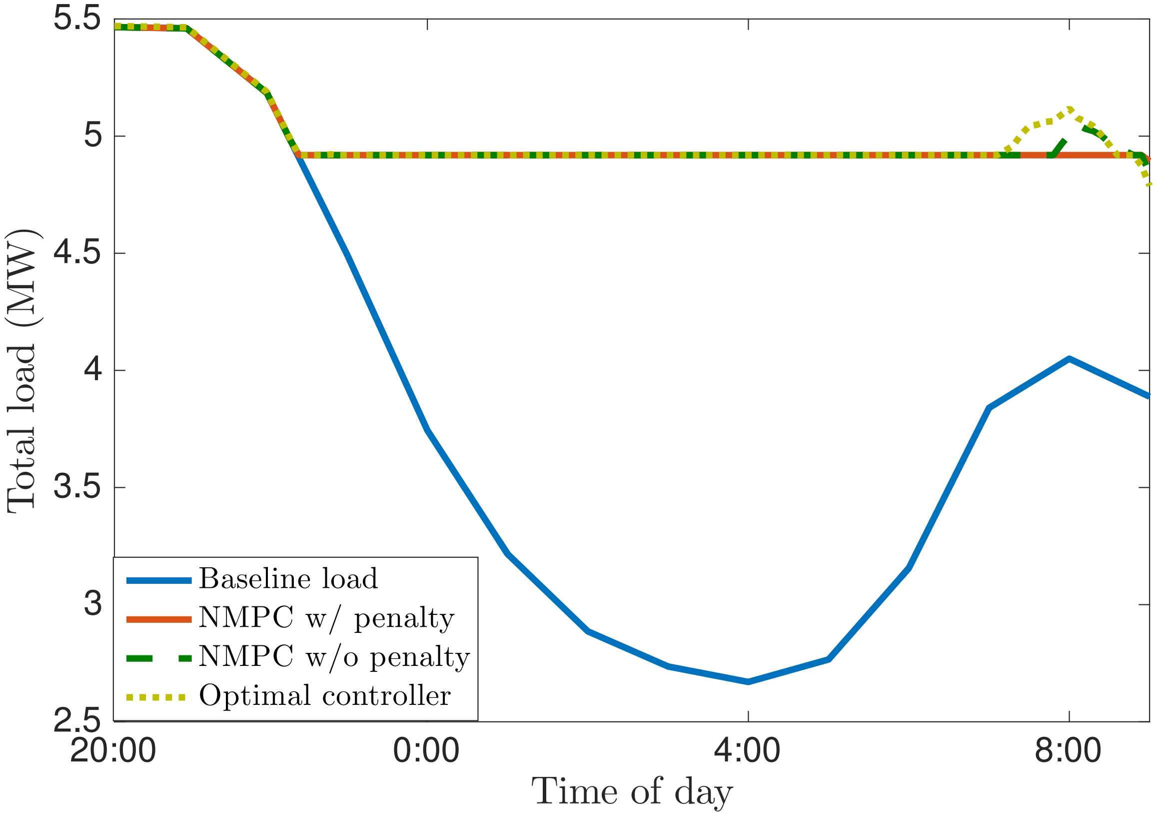

Figure 5.6: Valley-filling performance of three controllers.

is no desired aggregated power. This indicates that all PHEVs are idle, drawing no power from the grid, and the remained specified charging time is continuously decreasing, while the remained full-power charging time remains unchanged. In an extreme case, if the idle time is long enough, all PHEVs will have $\rho = 1$ and immediately start charging in full power. In other words, the idle time in the beginning impairs the valley-filling capacity in the end of the service. This can be revealed from the evolution of PHEVs' indices in Figure 5.7. Because of the long idle time, no matter which controller we use, starting from around 23:00, more or less PHEVs begin to have $\rho = 1$ and being charged in full power.

- The weak scheduling ability of Controller #2 and Controller #3 is also a key

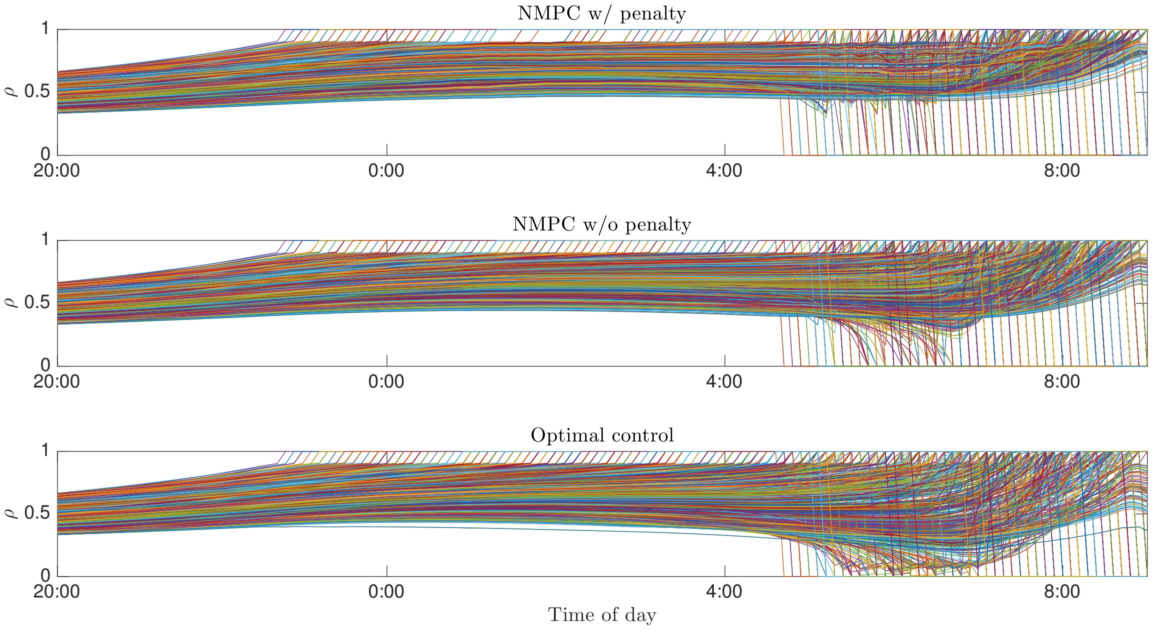

Figure 5.7: Index trajectories of all 1000 PHEVs.

factor. A good controller should be able to coordinate the PHEV population to achieve both the valley-filling service at the current time and to maintain a sufficiently long service time. We can notice from Figure 5.7 that, by applying Controller #3, indices of PHEVs continuously and intensively jump to 1 before 5:00; Controller #2 slightly suppresses this phenomenon in a certain degree but still not comparable with Controller #1. This weak scheduling ability drives most PHEVs charge in full power, thus losing the service capacity in the end. It can be further observed from 7:00 to 9:00 that, PHEVs being controlled by Controller #2 and Controller #3 intensively jump to $\rho = 1$, which severely impairs the service capacity.

- In addition, the number of fully charged PHEVs is also a factor that affects the service quality. If a controller fails to suppress the number of fully charged PHEVs, it cannot have a satisfying service quality at the end of the service, where the required aggregated power is relatively small but few PHEVs are adjustable. In Figure 5.7, after 5:00, numerous PHEVs controlled by Controller #3 get fully charged; Controller #2 can suppress this to a certain level, but the number of fully charged PHEVs is still way larger than that of Controller #1.

We can also analyze the performance from the view of the state trajectories. Figure 5.8 shows the evolutions of 10 elements in ζ. Being controlled by Controller #3, except ζ_1 and ζ_n, all other adjustable states are being driven to consensus then decrease. This decrease directly results in the increase of the number of nonadjustable PHEVs. From 7:00, i.e., the crossing point of ζ_1 and ζ_n, nonadjustable PHEVs dominate the population, implying a bad service for relatively low required charging power. In addition, the full-power charging population always keeps a high level, which directly results in the large deviation high in Figure 5.6. Being controlled by Controller #2, the level of the full-power charging population trajectory is suppressed to some extent, and is always lower than that of Controller #3. However, at around 8:00, though the control signals, which can be shown in Figure 5.9, for other populations are 0, the aggregated power consumption of the full-power charging population still exceeds the desired trajectory. In addition, the number of PHEVs in other populations is

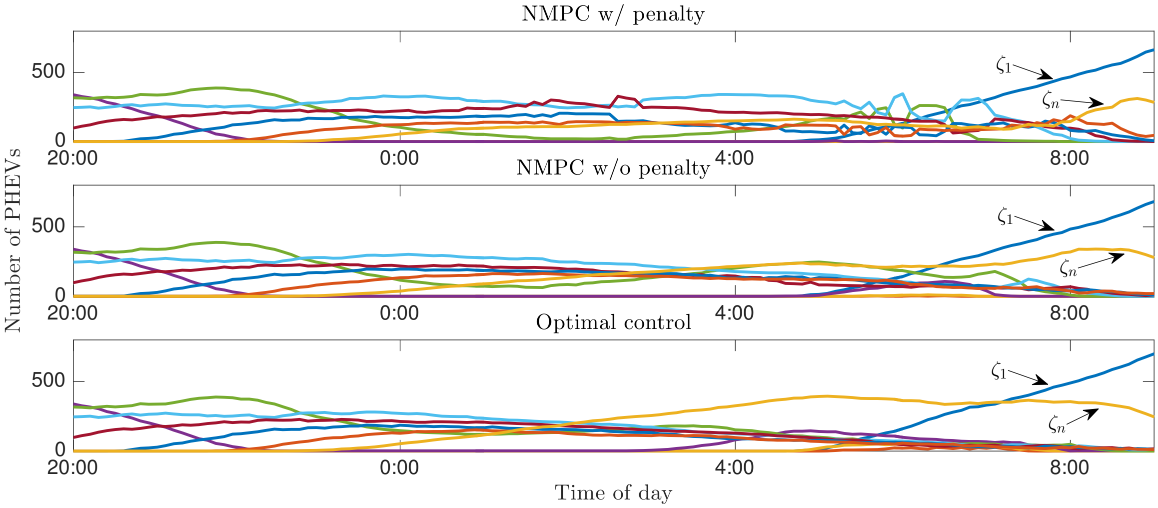

Figure 5.8: State trajectories.

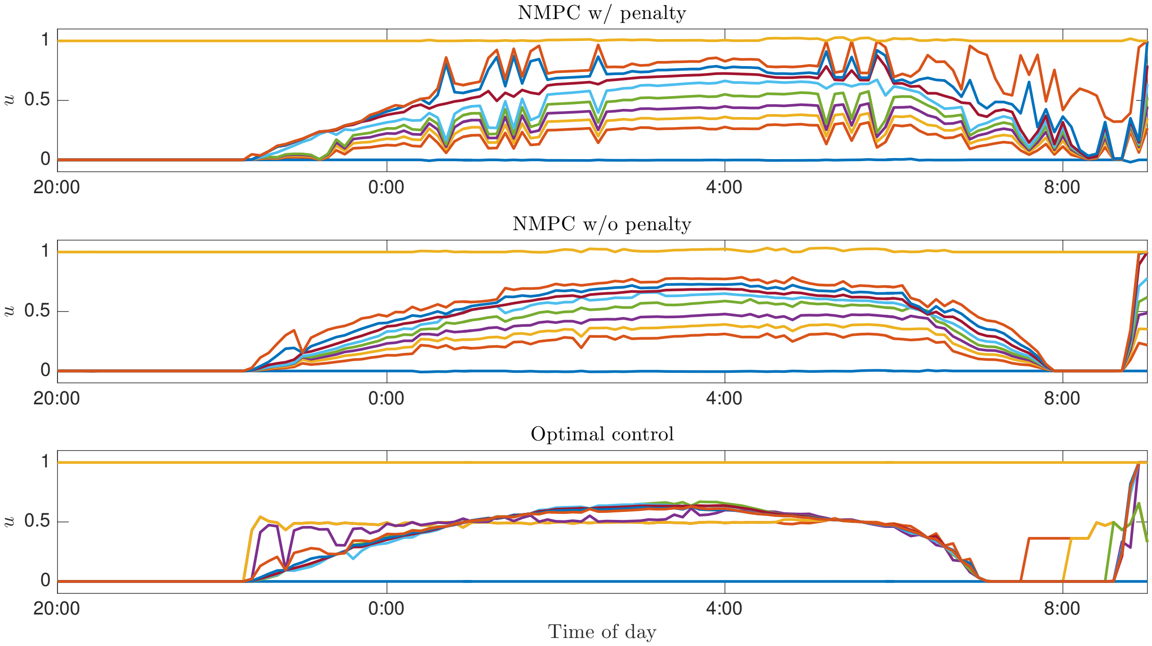

Figure 5.9: Control signal trajectories of 10 state bins.

extremely small. In contrast, being controlled by Controller #1, the trajectory of the full-power charging state ζ_n is always suppressed lower than those of the other two controllers. Especially at the end of the service, the number of full-power charging PHEVs is much lower, allowing a larger room for adjustment. In addition, trajectories of all states being controlled by Controller #1 are more diversified due to the much diversified control signals as shown in Figure 5.9.

As a supplement, Figure 5.10 shows the trajectories of individual charging rates. It can also be clearly observed from Figure 5.10 that, from 7:00, charging rates of PHEVs being controlled by Controller #3 are either 0 or 1; from 7:00 to 8:00, charging rates of PHEVs being controlled by Controller #2 can still vary between 0 and 1, however, after 8:00, all charging rates stay at either 0 or 1. In contrast, for Controller #1, the map of individual charging rates is more diversified; even after 8:00, there are still a sufficient number of PHEVs can draw small amount of power from the grid, providing a satisfying service quality.

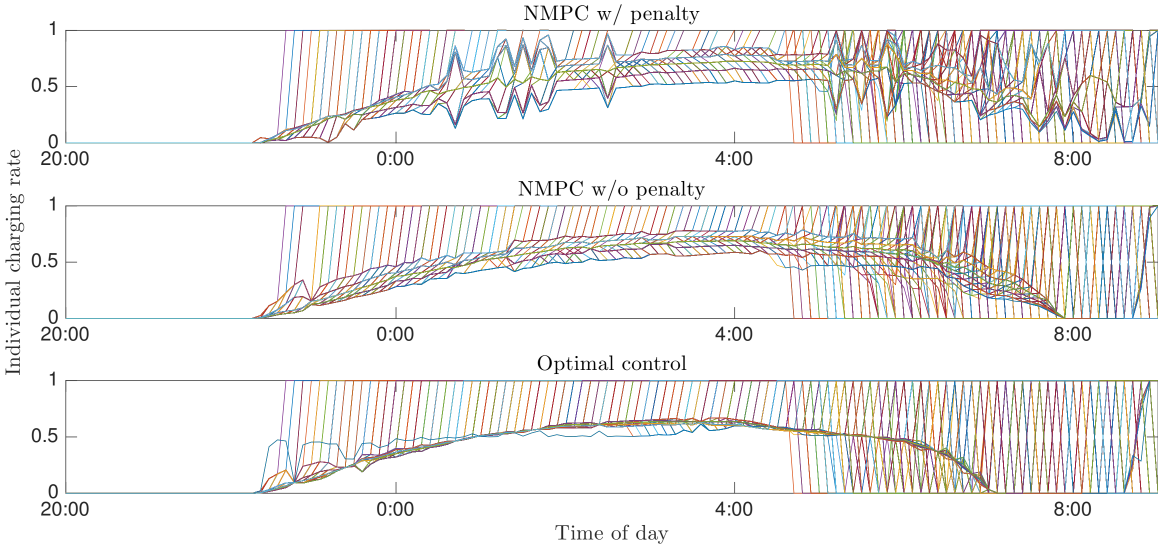

Figure 5.10: Individual charging rate trajectories of all 1000 PHEVs.

The last but not the least, one of the advantages of the proposed aggregation model is that it inherently guarantees drivers' charging requirements. By implementing the proposed aggregation model, individual PHEVs do not need to provide any SOC information through the communication link, which dramatically reduces the communication load in this CPS. The SOC evolutions of all PHEVs being controlled by the aforementioned three controllers can be shown in Figure 5.11. We can clearly observe that, most of the PHEVs are fully charged at the end of the service; some of the population is still being charged without violating charging requirements.

5.5 Conclusion

In this chapter, a novel framework for the aggregation and charging control of PHEVs is constructed from the CPS perspective. In the cyber space, an aggregation model is constructed based on a novel concept – charging requirement index, by which the heterogeneous charging requirements of individual PHEVs can be inherently guaranteed without adding additional constraints. Since only the index information is sent

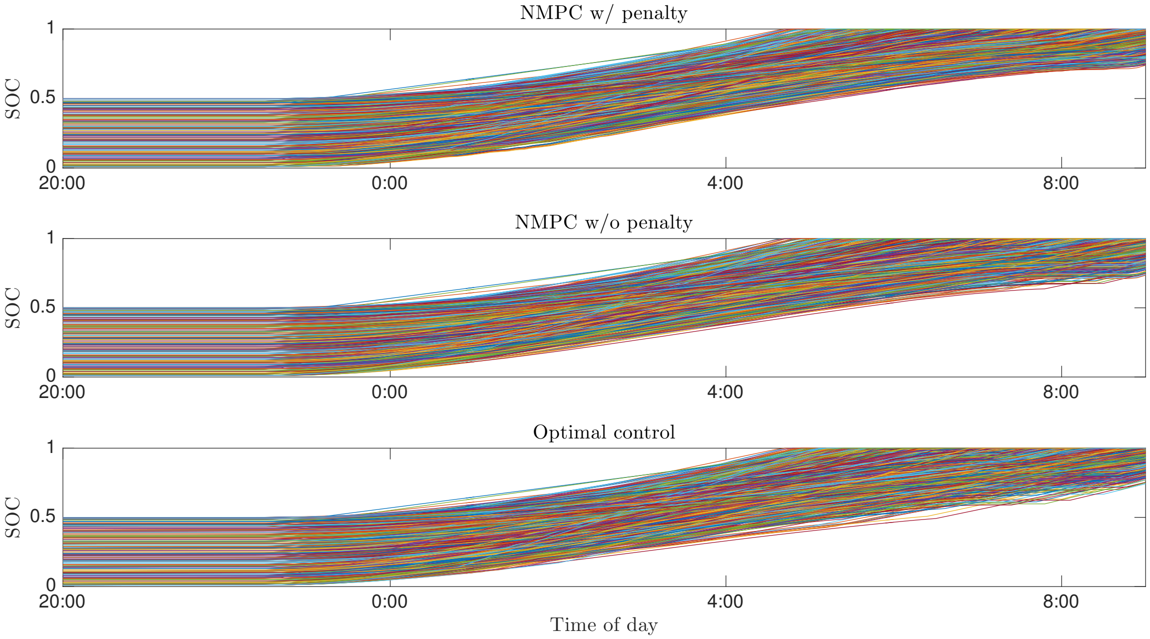

Figure 5.11: SOC trajectories of all 1000 PHEVs.

to the aggregator, the communication load in this framework is extremely low. In addition, the proposed aggregation model allows aggregator's controller to process clustered information to solve for the optimal control signal, which directly reduces the computational pressure. An NMPC control scheme is developed for the overnight valley-filling service. By comparing with another two benchmark controllers through the case study, the proposed controller possesses the merit of preserving the service capacity by diversifying the distribution of PHEVs, thus presenting an outstanding valley-filling service quality.

Chapter 6

Conclusions and Future Work

This PhD thesis concerns two problems in the field of utilizing controllable electric loads for DR: Aggregation Modeling and Control. Both of the TCAs and PHEVs are considered as the terminal loads. For the aggregation model development, we have studied through direct stacking, 2-D population-based model, 1-D improved population-based model, and index-induced population-based model. Investigations of the model proceed step-by-step from the ideal case to the most practical scenario. Based on the proposed models, we investigated various control schemes including centralized MPC, DMPC, and optimal control. Application areas discussed in this thesis include secondary frequency control, primary frequency control, and overnight valley-filling. Substantial case studies show that the proposed approaches are suitable for aggregating and controlling a large population of electric loads in smart grid for DR.

6.1 Conclusions

Chapter 2 studies the direct-stacking aggregation model and control methods of aggregated TCAs for the provision of secondary frequency control. A centralized MPC scheme is firstly presented. TCA lockout effect is explicitly formulated in the constraints of the MPC scheme. A novel method of converting time-integrated interdependent logic lockout conditions into inequalities is proposed in Chapter 2. A case study is conducted with realistic data, validating the feasibility of the proposed modeling and control approaches. Parametric studies in terms of temperature deadband width, ambient temperature, and lockout time, are conducted to investigate the service quality in different circumstances. The test results reveal that a population of diversified TCAs can become a major source of providing ancillary services. In Chapter 2, one step further to the practical application, the scenario in which all TCAs are VFD-free is investigated. A DMPC scheme is proposed based on the alternating searching technique. The DMPC scheme significantly reduces the centralized computational load, thus driving the proposed stacking model and control more practical.

For the purpose of the provision of primary frequency control, Chapter 3 proposes new aggregation modeling and control design approaches for heterogeneous TCAs. A 2-D state bin is proposed to formulate the second-order TCA dynamics in a 2-D population-based model. The population-based model converts the traditional individual dynamic evolutions into population migration probabilities, thus reducing the centralized computational complexity. Detailed procedure of calculating the migration probabilities in the system matrix is provided. In the controller design, a centralized MPC scheme is proposed to obtain the optimal control actions along the prediction horizon. In addition, implementation procedure of the control signal for adjusting TCAs' status is also investigated with practical constraints considered. Case study results reveal the feasibility and efficacy of the proposed modeling and control approaches when applied on a large population of TCAs. Key factors that may affect the service performance are also discussed in this chapter.

To eliminate the control signal mismatch, Chapter 4 proposes an improved population model with lockout time characterized in the aggregate dynamics. Based on that, a DMPC scheme is investigated to control a population of TCAs for the regulation service. Full derivations of the system model and the DMPC scheme are provided. A flexibility penalty is developed and added to the objective function to preserve the regulation flexibility. Simulation results, tested by real data, reveal the feasibility and effectiveness of the proposed methods. Furthermore, in the case when future regulation signals are not available or difficult to predict, an optimal control scheme is proposed. By introducing the regulation capacity in the objective function, the optimal control scheme has comparable performance with the centralized MPC, however, with way less computational load and no requirement on future regulation signals.

In Chapter 5, by following the CPS design approach, a novel framework for the local aggregator to estimate the charging status and solve for the charging control signals for PHEVs is proposed. The physical battery charging is executed by charging stalls, where charging information is processed in the embedded system and only the generated index information is transmitted to the aggregator via communication networks. An aggregation model is developed for the entire cyber space to inherently guarantee heterogeneous charging requirements, i.e., deadlines for charging. Furthermore, an NMPC scheme is developed for the overnight valley-filling service. Both the aggregation model and control strategy are designed based on the PHEV population migration probabilities. From the CPS perspective, both the cyber and physical loads of this novel framework are extremely low. As a part of this chapter, a valley-filling case study is conducted, verifying the proposed approaches.

6.2 Future Work

The current study of service-signal-based DR programs is still in a preliminary stage. In a complete DR framework, three parties, i.e., utilities, aggregators, and customers, actively cooperate to achieve the DR goal. Particularly, aggregators play a role as the intermediary agent between the utility and customers. Speaking of that, aggregators are in charge of grasping the running status from and dispatching control signals to customers. However, with the current smart grid infrastructure in which a fast two-way digital communication network is not complete, it is impossible or economically infeasible for aggregators to receive and process the bulk information from all end-users in real time. Thus, it is urged to design an aggregation model for aggregators to accurately predict or estimate the terminal users running status without real-time monitoring. This aggregation model is the foundation of and desirable for service-signal-based DR programs. In addition, it is promising to design controllers for an area having both controllable TCAs and PHEVs committed [117], hence, the regulation capacity can be significantly enlarged.

Secondly, based on the above-discussed general aggregation model, advanced controllers that can adapt to most types of regulation services are also demanded. These services include primary frequency control, secondary frequency control, and valley-filling. In addition, a high-performance controller must be robust to various disturbances. One type of the disturbance is the random program joining and leaving. When using TCAs as terminal loads, it is possible that, in some circumstances, some end-users may suspend their TCAs for a certain period; when using PHEVs, it is also normal that drivers plug in their PHEVs at random time. This type of disturbance will cause a loss of service capability. Another type of disturbance is mainly caused by human activities, e.g., window opening and emergency PHEV full-power charging, which impacts more on local control. Both of the aforementioned uncertainties urge the design of a robust controller.

Moreover, cyber-attacks are inevitable in a large communication network, especially in smart grid. In the presence of attacks, on the one hand, the customers' privacy is challenged; on the other hand, customers' experience and regulation service quality are severely affected. This inspires the design of an attack-aware controller which actively detects, predicts, and suppresses cyber-attacks, instead of being passively robust to attacks as in traditional attack-tolerant controllers.

Equally importantly, a motivating incentive scheme is imperative to guarantee the success of this new DR framework. Only with a sufficient number of active participants, the aggregated power consumption could be employed for regulation services. Since DR services may increase customers' power consumption in order to fulfill the needs, the incentive should fully cover the increased bill and provide certain rewards.

Appendix A

Publications

- **Refereed journal papers that have been published or accepted**

J1. **M. Liu**, Y. Shi, and H. Gao, "Aggregation and charging control of PHEVs in smart grid: A cyber-physical perspective," *Proceedings of the IEEE*, vol. 104, no. 5, pp. 1071-1085, 2016.

J2. **M. Liu** and Y. Shi, "Model predictive control for thermostatically controlled appliances providing load balancing service," *IEEE Transactions on Control Systems Technology*, to appear, doi: 10.1109/TCST.2016.2535400, 2016.

J3. **M. Liu**, Y. Shi, and X. Liu, "Distributed MPC of aggregated heterogeneous thermostatically controlled loads in smart grid," *IEEE Transactions on Industrial Electronics*, vol. 63, no. 2, pp. 1120-1129, 2016.

J4. **M. Liu** and Y. Shi, "Model predictive control of aggregated heterogeneous second-order thermostatically controlled loads for ancillary services," *IEEE Transactions on Power Systems*, vol. 31, no. 3, pp. 1963-1971, 2016.

J5. **M. Liu**, Y. Shi, and F. Fang, "Load forecasting and operation strategy design for CCHP systems using forecasted loads," *IEEE Transactions on Control Systems Technology*, vol. 23, no. 5, pp. 1672-1684, 2015.

J6. **M. Liu**, Y. Shi, and F. Fang, "Combined cooling, heating and power systems: A survey," *Renewable & Sustainable Energy Reviews*, vol. 35, pp. 1-22, 2014.

J7. **M. Liu**, Y. Shi, and X. Liu, "T-S fuzzy-model-based $\mathcal{H}_2$ and $\mathcal{H}_\infty$ filtering for networked control systems with two-channel Markovian random delays," *Digital Signal Processing*, vol. 27, pp. 167-174, 2014.

J8. H. Zhang, **M. Liu**, J. Sheng, and Y. Shi, "Extended LMI representatives for stability and stabilization of discrete-time Takagi-Sugeno fuzzy systems," *Optimal Control Applications and Methods*, vol. 35, no. 6, pp. 647-655, 2014.

J9. **M. Liu**, Y. Shi, and F. Fang, "Optimal power flow and PGU capacity of CCHP systems using a matrix approach," *Applied Energy*, vol. 102, pp. 794-802, 2013.

J10. H. Zhang, Y. Shi, and **M. Liu**, "$\mathcal{H}_\infty$ step tracking control for networked discrete-time nonlinear systems with integral and predictive actions," *IEEE Transactions on Industrial Informatics*, vol. 9, no. 1, pp. 337-345, 2013.

J11. H. Zhang, Y. Shi, and **M. Liu**, "$\mathcal{H}_\infty$ switched filtering for networked systems based on delay occurrence probabilities," *ASME Journal of Dynamic Systems, Measurement, and Control*, vol. 135, no. 6, pp. 061002, 2013.

J12. **M. Liu**, Y. Shi, and F. Fang, "A new operation strategy for CCHP systems with hybrid chillers," *Applied Energy*, vol. 95, pp. 164-173, 2012.

- **Refereed conference papers that have been published**

C1. **M. Liu** and Y. Shi, "Optimal control of aggregated heterogeneous thermostatically controlled loads for regulation services," in *Proceedings of IEEE Conference on Decision and Control*, Osaka, Japan, December 15-18, 2015, pp. 5871-5876.

C2. **M. Liu** and Y. Shi, "Distributed model predictive control of thermostatically controlled appliances for providing load balancing service," in *Proceedings of IEEE Conference on Decision and Control*, Los Angeles, California, USA, December 15-17, 2014, pp. 4850-4855.

C3. **M. Liu** and Y. Shi, "An energy efficient optimal operation strategy design for CCHP systems," in *Proceedings of Canadian Society of Mechanical Engineers (CSME) International Congress*, Winnipeg, Manitoba, Canada, June 4-6, 2012, pp. 1-8.

- **Theses**

T1. **M. Liu**, *Energy Efficient Operation Strategy Design for the Combined Cooling, Heating and Power System*, Master of Applied Science Thesis, Department of Mechanical Engineering, University of Victoria, Canada, 2012.

T2. **M. Liu**, *ZigBee Wireless Location Technology-Based 3D Real-Time Simulation*, Bachelor of Engineering Thesis, Department of Control Science and Engineering, Harbin Institute of Technology, China, 2010.

Bibliography

[1] H. Farhangi, "The path of the smart grid," *IEEE Power & Energy Magazine*, vol. 8, no. 1, pp. 18–28, 2010.

[2] Department of Energy, "The smart grid: An introduction," Department of Energy, USA, Tech. Rep., 2014.

[3] ——, "Smart grid," 2014. [Online]. Available: http://energy.gov/oe/services/technology-development/smart-grid

[4] V. Balijepalli, V. Pradhan, S. Khaparde, and R. Sherref, "Review of demand response under smart grid paradigm," in *Proceedings of IEEE PES Innovative Smart Grid Technologies*, Kollam, Kerala, India, December 1-3 2011, pp. 236–243.

[5] Department of Energy, "Benefits of demand response in electricity markets and recommendations for achieving them," Department of Energy, Tech. Rep., 2006.

[6] S. Hunt, *Making Competition Work in Electricity.* New York: John Wiley & Sons, 2002.

[7] Federal Energy Regulatory Commission, "Assessment of demand response and advanced metering," Federal Energy Regulatory Commission, Tech. Rep., 2012.

[8] ——, “Assessment of demand response and advanced metering,” Federal Energy Regulatory Commission, Tech. Rep., 2013.

[9] ——, “Assessment of demand response and advanced metering,” Federal Energy Regulatory Commission, Tech. Rep., 2006.

[10] Department of Energy, “Energy efficiency and renewable energy,” Department of Energy, Tech. Rep., 2008.

[11] Intercontinental Exchange, Inc. (2014). [Online]. Available: https://www.theice.com

[12] U.S. Energy Information Adminstration. (2014). [Online]. Available: http://www.eia.gov/electricity/wholesale/

[13] W. Hogan, “On an ‘energy only’ electricity market design for resource adequacy,” Center for Business and Government, John F. Kennedy School of Government, Harvard University, Tech. Rep., 2005.

[14] M. Albadi and E. El-Saadany, “A summary of demand response in electricity markets,” *Electric Power Systems Research*, vol. 78, pp. 1989–1996, 2008.

[15] J. Aghaei and M. Alizadeh, “Demand response in smart electricity grids equipped with renewable energy sources: A review,” *Renewable & Sustainable Energy Reviews*, vol. 18, pp. 64–72, 2013.

[16] J. Wang, C. Bloyd, Z. Hu, and Z. Tan, “Demand response in China,” *Energy*, vol. 35, no. 4, pp. 1529–1597, 2010.

[17] J. Torriti, M. Hassan, and M. Leach, “Demand response experience in Europe: Policies, programmes and implementation,” *Energy*, vol. 35, no. 4, pp. 1575–1583, 2009.

[18] A. Abdollahi, M. Parsa, M. Rashidinejad, and M. Sheikh-El-Eslami, "Investigation of economic and environmental-driven demand response measures incorporating UC," *IEEE Transactions on Smart Grid*, vol. 3, no. 1, pp. 12–25, 2012.

[19] S. Borenstein, "The trouble with electricity markets: Understanding California's reconstructing diaster," *Journal of Economic Perspectives*, vol. 16, no. 1, pp. 191–211, 2002.

[20] K. Spees and L. Lave, "Demand response and electricity market efficiency," *The Electricity Journal*, vol. 20, no. 3, pp. 69–85, 2007.

[21] C. King and D. Delurey, "Efficiency and demand response: Twins, siblings, or cousins?" *Public Utilities Forthinghtly*, vol. 143, no. 3, pp. 54–61, 2005.

[22] F. Rahimi and A. Ipakchi, "Demand response as a market resource under the smart paradigm," *IEEE Transactions on Smart Grid*, vol. 1, no. 1, pp. 82–88, 2010.

[23] Federal Energy Regulatory Commission, "Order No. 719," Federal Energy Regulatory Commission, Tech. Rep., 2008.

[24] ——, "Order No. 745," Federal Energy Regulatory Commission, Tech. Rep., 2011.

[25] ——, "Order No. 1000," Federal Energy Regulatory Commission, Tech. Rep., 2011.

[26] The Recovery Accountability and Transparency Board, "American recovery and reinvestment act," The Recovery Accountability and Transparency Board, Tech. Rep., 2009.

[27] P. Siano, “Demand response and smart grids–a survey,” *Renewable & Sustainable Energy Reviews*, vol. 30, pp. 461–478, 2014.

[28] J. Medina, N. Muller, and I. Roytelman, “Demand response and distribution grid operations: Opportunities and challenges,” *IEEE Transactions on Smart Grid*, vol. 1, no. 2, pp. 193–198, 2010.

[29] S. Mohagheghi, J. Stoupis, Z. Wang, Z. Li, and H. Kazemzadeh, “Demand response architecture–integration into the distribution management system,” in *Proceedings of IEEE International Conference on Smart Grid Communications*, Gaithersburg, MD, USA, October 4-6 2010, pp. 501–506.

[30] R. Poudineh and T. Jamasb, “Distributed generation, storage, demand response and energy efficiency as alternatives to grid capacity enhancement,” *Energy Policy*, vol. 67, pp. 222–231, 2014.

[31] G. Strbac, “Demand side mangement: Benefits and challenges,” *Energy Policy*, vol. 36, pp. 4419–4426, 2008.

[32] S. Madaeni and R. Sioshansi, “Usign demand response to improve the emission benefits of wind,” *IEEE Transactions on Power Systems*, vol. 28, no. 2, pp. 1385–1394, 2013.

[33] N. Gilbraith and S. Powers, “Residential demand response reduces air pollutant emissions on peak electricity demand days in New York City,” *Energy Policy*, vol. 59, pp. 459–469, 2013.

[34] J. Kondon, “Direct load control for wind power integration,” in *Proceedings of IEEE Power and Energy Society General Meeting*, San Diego, CA, USA, July 24-29 2011, pp. 1–8.

[35] A. Kowli and S. Meyn, “Supporting wind generation deployment with demand response,” in *Proceedings of IEEE Power and Energy Society General Meeting*, San Diego, CA, USA, Jul. 24-29 2011, pp. 1–8.

[36] S. Madaeni and R. Sioshansi, “The impacts of stochastic programming and demand response on wind integration,” *Energy Systems*, vol. 4, no. 2, pp. 109–124, 2013.

[37] H. Chao, “Demand response in wholesale electricity markets: The choices of customer baseline,” *Journal of Regulatory Economics*, vol. 39, no. 1, pp. 68–88, 2011.

[38] H. Fraser, “The importance of an active demand side in the electricity industry,” *The Electricity Journal*, vol. 14, no. 9, pp. 52–73, 2001.

[39] N. Venkatesan, J. Solanki, and S. Solanki, “Residential demand response model and impact on voltage profile and losses of an electric distribution network,” *Applied Energy*, vol. 96, pp. 84–91, 2012.

[40] Oak Ridge National Laboratory, “Assessment of industrial load for demand response across U.S. regions of the western interconnect,” Oak Ridge National Laboratory, Tech. Rep., 2013.

[41] N. Motegi, M. Piette, D. Watson, S. Kiliccote, and P. Xu, “Introduction to commercial building control strategies and techniques for demand response,” Lawrence Berkeley National Laboratory, Tech. Rep., 2007.

[42] R. Hornby, D. Hurley, and P. Knight, “A review of demand response potential in the United States,” Synapse Energy Economics Inc., Tech. Rep., 2011.

[43] P. Bradley, M. Leach, and J. Torriti, "A review of the costs and benefits of demand response for electricity in the UK," *Energy Policy*, vol. 52, pp. 312–327, 2013.

[44] P. Grünewald and J. Torriti, "Demand response from the non-domestic sector: Early UK experiences and future opportunities," *Energy Policy*, vol. 61, pp. 423–429, 2013.

[45] H. Sæle and O. Grande, "Demand response from household customers: Experiences from a pilot study in Norway," *IEEE Transactions on Smart Grid*, vol. 2, no. 1, pp. 102–109, 2011.

[46] J. MacDonald, P. Cappers, D. Callaway, and S. Kiliccote, "Demand repsonse providing ancillary services–a comparison of opportunities and chanllenges in the US wholesale markets," Lawrence Berkeley National Laboratory, Tech. Rep., 2012.

[47] D. Callaway and I. Hiskens, "Achieving controllability of electric loads," *Proceedings of the IEEE*, vol. 99, no. 1, pp. 184–199, 2011.

[48] I. Hiskens and D. Callaway, "Achieving controllability of plug-in electric vehicles," in *Proceedings of IEEE Vehicle Power and Propulsion Conference*, Dearborn, MI, USA, September 7-10 2009, pp. 1215–1220.

[49] S. Kundu, N. Sinitsyn, S. Backhaus, and I. Hiskens, "Modeling and control of thermostatically controlled loads," in *Proceedings of Power Systems Computation Conference*, Stockholm, Sweden, August 22-26 2011, pp. 969–975.

[50] N. Lu, "An evaluation of the HVAC load potential for providing load balancing service," *IEEE Transactions on Smart Grid*, vol. 3, no. 3, pp. 1263–1270, 2012.

[51] W. Zhang, J. Lian, C.-Y. Chang, and K. Kalsi, "Aggregated modeling and control of air conditioning loads for demand response," *IEEE Transactions on Power Systems*, vol. 28, no. 4, pp. 4655–4664, 2013.

[52] H. Hao, B. Sanandaji, K. Poolla, and T. Vincent, "Aggregated flexibility of thermostatically controlled loads," *IEEE Transactions on Power Systems*, vol. 30, no. 1, pp. 189–198, 2015.

[53] N. Lu and D. P. Chassin, "A state-queueing model of thermostatically controlled appliances," *IEEE Transactions on Power Systems*, vol. 19, no. 3, pp. 1666–1673, 2004.

[54] J. Kondon, N. Lu, and D. Hammerstrom, "An evaluation of the water heater load potential for providing regulation service," in *Proceedings of IEEE Power and Energy Society General Meeting*, San Diego, CA, USA, July 24-29 2011, pp. 1–8.

[55] N. Lu, P. Du, and Y. Markov, "The potential of thermostatically controlled appliances for intra-hour energy storage applications," in *Proceedings of IEEE Power and Energy Society General Meeting*, San Diego, CA, USA, July 22-26 2012, pp. 1–6.

[56] Y. Zhang and N. Lu, "Demand-side management of air conditioning cooling loads for intra-hour load balancing," in *Proceedings of IEEE PES Innovative Smart Grid Technologies*, Washington, DC, USA, February 24-27 2013, pp. 1–6.

[57] N. Lu and Y. Zhang, "Design considerations of a centralized load controller using thermostatically controlled appliances for continuous regulation reserves," *IEEE Transactions on Smart Grid*, vol. 4, no. 2, pp. 914–921, 2013.

[58] Y. Zhang and N. Lu, “Parameter selection for a centralized thermostatically controlled appliances load controller used for intra-hour load balancing,” *IEEE Transactions on Smart Grid*, vol. 4, no. 4, pp. 2100–2108, 2013.

[59] K. Kalsi, F. Chassin, and D. Chassin, “Aggregated modeling of thermostatically loads in demand response: A system and control perspective,” in *Proceedings of IEEE Conference on Decision and Control and European Control Conference*, Orlando, FL, USA, December 12-15 2011, pp. 15–20.

[60] K. Kalsi, M. Elizondo, J. Fuller, S. Lu, and D. Chassin, “Development and validation of aggregated models for thermostatic controlled loads with demand response,” in *Proceedings of Hawaii International Conference on System Science*, Maui, HI, USA, January 4-7 2012, pp. 1959–1966.

[61] E. Vrettos, J. Mathieu, and G. Andersson, “Control of thermostatic loads using moving horizon estimation of individual states,” in *Proceedings of Power Systems Computation Conference*, Wroclaw, Poland, August 18-22 2014, pp. 1–7.

[62] D. Guo, W. Zhang, G. Yan, Z. Lin, and M. Fu, “Dencentralized control of aggregated loads for demand response,” in *Proceedings of American Control Conference*, Washington, DC, USA, June 17-19 2013, pp. 6601–6606.

[63] R. Malhamé and C.-Y. Chong, “Electric-load model synthesis by diffusion approximation of a high-order hybrid-state stochastic-system,” *IEEE Transactions on Automatic Control*, vol. 30, no. 9, pp. 854–860, 1985.

[64] D. Callaway, “Tapping the energy storage potential in electric loads to deliver load following and regulation, with application to wind energy,” *Energy Conversion and Management*, vol. 50, no. 5, pp. 1389–1400, 2009.

[65] S. Koch, J. Mathieu, and D. Callaway, "Modeling and control of aggregated heterogeneous thermostatically controlled loads for ancillary services," in *Proceedings of Power Systems Computation Conference*, Stockholm, Sweden, August 22-26 2011, pp. 1–7.

[66] J. Mathieu and D. Callaway, "State estimation and control of heterogenerous thermostatically controlled loads for load following," in *Proceedings of Hawaii International Conference on System Science*, Maui, HI, USA, January 4-7 2012, pp. 2002–2011.

[67] J. Mathieu, S. Koch, and D. Callaway, "State estimation and control of electric loads to manage real-time energy imbalance," *IEEE Transactions on Power Systems*, vol. 28, no. 1, pp. 430–440, 2013.

[68] E. Vrettos, J. Mathieu, and G. Andersson, "Demand response with moving horizon estimation of individual thermostatic load states from aggregate power measurement," in *Proceedings of American Control Conference*, Portland, OR, USA, June 4-6 2014, pp. 4846–4853.

[69] B. Sanandaji, H. Hao, and K. Poolla, "Fast regulation service provision via aggregation of thermostatically controlled loads," in *Proceedings of Hawaii International Conference on System Science*, Waikoloa, HI, USA, January 6-9 2014, pp. 2388–2397.

[70] W. Zhang, K. Kalsi, J. Fuller, M. Elizondo, and D. Chassin, "Aggregate model for heterogeneous thermostatically controlled loads with demand response," in *Proceedings of IEEE Power and Energy Society General Meeting*, San Diego, CA, USA, July 22-26 2012, pp. 1–8.

[71] A. Hota, M. Juvvanapudi, and P. Bajpai, "Issues and solution approaches in PHEV integration to smart grid," *Renewable & Sustainable Energy Reviews*, vol. 30, pp. 217–229, 2014.

[72] C. Liu, K. T. Chau, D. Wu, and S. Gao, "Opportunities and challenges of vehicle-to-home, vehicle-to-vehicle, and vehicle-to-grid technologies," *Proceedings of the IEEE*, vol. 101, no. 11, pp. 2409–2427, 2013.

[73] F. Tuffner and M. Kintner-Meyer, "Using electric vehicles to meet balancing requirements associated with wind power," Pacific Northwest National Laboratory, Tech. Rep., 2011.

[74] ——, "Using electric vehicles to mitigate imbalance requirements associated with an increated penetration of wind generation," in *Proceedings of IEEE Power and Energy Society General Meeting*, San Diego, CA, USA, Jul. 24-29 2011, pp. 1–8.

[75] J. Escudero-Garzás, A. Garciá-Armada, and G. Seco-Granados, "Fair design of plug-in electric vehicles aggregator for V2G regulation," *IEEE Transactions on Vehicular Technology*, vol. 61, no. 8, pp. 3406–3419, 2012.

[76] W. Zhang, C. Xu, and C.-Y. Chang, "Demand dynamics aggregation using hybrid systems," in *Proceedings of the Annual Allerton Conference on Communication, Control and Computing*, Monticello, IL, USA, October 1-5 2012, pp. 1475–1481.

[77] S. Kundu and I. Hiskens, "Hysteresis-based charging control of plug-in electric vehicles," in *Proceedings of IEEE Conference on Decision and Control*, Maui, HI, USA, December 10-13 2012, pp. 5598–5604.

[78] S. Izadkhast, P. Garcia-Gonzalez, and P. Frías, "An aggregation model of plug-in electric vehicles for primary frequency control," *IEEE Transactions on Power Systems*, vol. 30, no. 3, pp. 1475–1482, 2015.

[79] S. Bashash and H. Fathy, "Transport-based load modelling and sliding mode control of plug-in electric vehicles for robust renewable power tracking," *IEEE Transactions on Smart Grid*, vol. 3, no. 1, pp. 526–534, 2012.

[80] U.S. Energy Information Adminstration, "Electric power monthly," U.S. Energy Information Adminstration, Tech. Rep., 2013.

[81] S. Bashash and H. Fathy, "Modeling and control of aggregate air conditioning loads for robust renewable power management," *IEEE Transactions on Control Systems Technology*, vol. 21, no. 4, pp. 1318–1327, 2013.

[82] S. Soudjani and A. Abate, "Aggregation and control of populations of thermostatically controlled loads by formal abstractions," *IEEE Transactions on Control Systems Technology*, vol. 23, no. 3, pp. 975–990, 2015.

[83] E. Camacho and C. Bordons, *Model Predictive Control.* London: Springer, 2013.

[84] V. Veselý, D. Rosinová, and T. Quang, "Networked output feedback robust predictive controller design," *International Journal of Innovative Computing, Information and Control*, vol. 9, no. 10, pp. 3941–3953, 2013.

[85] H. Li and Y. Shi, "Networked-based predictive control for constrained nonlinear systems with two-channel packet dropouts," *IEEE Transactions on Industrial Electronics*, vol. 61, no. 3, pp. 1574–1582, 2014.

[86] G. Mantovani and L. Ferrarini, “Temperature control of a commercial building with model predictive control techniques,” *IEEE Transactions on Industrial Electronics*, vol. 62, no. 4, pp. 2651–2660, 2015.

[87] H. Han and J. Qiao, “Nonlinear model-predictive control for industrial processes: An application to wastewater treatment process,” *IEEE Transactions on Industrial Electronics*, vol. 61, no. 4, pp. 1970–1982, 2014.

[88] X. Luo, M. Wei, F. Xu, X. Zhou, and S. Wang, “Input feedback control of manipulated variables in model predictive control,” *International Journal of Innovative Computing, Information and Control*, vol. 10, no. 3, pp. 963–977, 2014.

[89] J. Yao, G. Costanzo, G. Zhu, and B. Wen, “Power admission control with predictive thermal management in smart buildings,” *IEEE Transactions on Industrial Electronics*, vol. 62, no. 4, pp. 2642–2650, 2015.

[90] S. Mariéthoz and M. Morari, “Modelling and hierarchical hybrid optimal control of prosumers for improved integration of renewable energy sources into the grid,” in *Proceedings of American Control Conference*, Montréal, QC, Canada, June 27-29 2012, pp. 3114–3119.

[91] G. Ledva, R. Vujanic, S. Mariéthoz, M. Morari, and J. Frunt, “Model predictive control of a large fleet of thermal loads and electric power generators, with an assessment for the Netherlands,” in *Proceedings of International Conference on the European Energy Market*, Stockholm, Sweden, May 27-31 2013, pp. 1–8.

[92] G. Larsen, N. van Foreest, and J. Scherpen, “Distributed control of the power supply-demand balance,” *IEEE Transactions on Smart Grid*, vol. 4, no. 2, pp. 828–836, 2013.

[93] G. Larsen, S. Trip, N. van Foreest, and J. Scherpen, "Distributed MPC for controlling μ-CHPs in a network," in *Proceedings of American Control Conference*, Montréal, QC, Canada, June 27-29 2012, pp. 3089–3094.

[94] A. Bemporad and M. Morari, "Control of systems integrating logic, dynamics, and constraints," *Automatica*, vol. 35, pp. 407–427, 1999.

[95] K. Srinivas and N. Lu, "Evaluation of residential HVAC control strategies for demand response programs," *ASHRAE Transactions*, vol. 1, no. 12, pp. 1–12, 2006.

[96] S. Ihara and F. C. Schweppe, "Physically based modeling of cold load pick up," *IEEE Power Engineering Review*, vol. PER-1, no. 9, pp. 27–28, 1981.

[97] R. Sonderegger, "Dynamic models of house heating based on equivalent thermal parameters," Ph.D. dissertation, Department of Mechanical and Aerospace Engineering, Princeton University, 1978.

[98] N. Wilson, B. Wagner, and W. Colborne, "Equivalent thermal paramenters for an occupied gas-heated house," *ASHRAE Transactions*, vol. 91, 1985.

[99] PJM. (2015) Regulation data. [Online]. Available: http://www.pjm.com/

[100] C.-Y. Chang, W. Zhang, J. Lian, and K. Kalsi, "Modeling and control of aggregated air conditioning loads under realistic conditions," in *Proceedings of IEEE PES Innovative Smart Grid Technologies*, Washington, DC, USA, February 24-27 2013, pp. 1–6.

[101] D. Jia and B. Krogh, "Distributed model predictive control," in *Proceedings of American Control Conference*, Arlington, VA, USA, June 25-27 2001, pp. 2767–2772.

[102] A. Venkat, I. Hiskens, J. Rawlings, and S. Wright, "Distributed MPC strategies with application to power system automatic generation control," *IEEE Transactions on Control Systems Technology*, vol. 16, no. 6, pp. 1192–1206, 2008.

[103] M. Liu and Y. Shi, "Distributed model predictive control of thermostatically controlled appliances for providing balancing service," in *Proceedings of IEEE Conference on Decision and Control*, Los Angeles, CA, USA, December 15-17 2014, pp. 4850–4855.

[104] C. C. Chan, "The state of the art of electric, hybrid, and fuel cell vehicles," *Proceedings of the IEEE*, vol. 95, no. 4, pp. 704–718, 2007.

[105] K. T. Chau and C. C. Chan, "Emerging energy-efficient technologies for hybrid electric vehicles," *Proceedings of the IEEE*, vol. 95, no. 4, pp. 821–835, 2007.

[106] J. Cobb. (2015) Top 6 plug-in vehicle adopting countries – 2014. [Online]. Available: http://www.hybridcars.com/top-6-plug-in-vehicle-adopting-countries-2014/

[107] Z. Shahan. (2014) Electric vehicle market share in 19 countries. [Online]. Available: http://www.abb-conversations.com/2014/03/electric-vehicle-market-share-in-19-countries/

[108] L. Gan, U. Topcu, and S. Low, "Optimal decentralized protocol for electric vehivle charging," *IEEE Transactions on Power Systems*, vol. 28, no. 2, pp. 940–951, 2013.

[109] C. Roe, F. Evangelos, J. Meisel, A. Meliopoulos, and T. Overbye, "Power system level impacts of PHEVs," in *Proceeding of Hawaii International Conference on System Sciences*, Big Island, HI, USA, January 5-8 2009, pp. 1–10.

[110] K. Clement, E. Haesen, and J. Driesen, “Coordinated charging of multiple plug-in hybrid electric vehicles in residential distribution grids,” in *Proceedings of IEEE/PES Power Systems Conference and Exposition*, Seattle, WA, USA, March 15-18 2009, pp. 1–7.

[111] S. Karnouskos, “Cyber-physical systems in the SmartGrid,” in *Proceedings of IEEE International Conference on Industrial Informatics*, Caparica, Lisbon, July 26-29 2011, pp. 20–23.

[112] Z. Ma, D. Callaway, and I. Hiskens, “Decentralized charging control of large populations of plug-in electric vehicles,” *IEEE Transactions on Control Systems Technology*, vol. 21, no. 1, pp. 67–78, 2013.

[113] P. Denholm and W. Short, “An evaluation of utility system impacts and benefits of optimally dispatched plug-in hybrid electric vehicles,” National Renewable Energy Laboratory, Tech. Rep., 2006.

[114] Z. Ma, I. Hiskens, and D. Callaway, “A dencentralized MPC strategy for charging large populations of plug-in electric vehicles,” in *Proceedings of IFAC World Congress*, Milano, Italy, August 28 - September 2 2011, pp. 10 493–10 498.

[115] M. Liu and Y. Shi, “Model predictive control of aggregated heterogeneous second-order thermostatically controlled loads for ancillary services,” *IEEE Transactions on Power Systems*, vol. PP, no. 99, pp. 1–9, 2015.

[116] M. Liu, Y. Shi, and X. Liu, “Distributed MPC of aggregated heterogeneous thermostatically controlled loads in smart grid,” *IEEE Transactions on Industrial Electronics*, vol. 63, no. 2, pp. 1120–1129, 2015.

[117] M. Galus, S. Koch, and G. Andersson, “Provision of load frequency control by PHEVs, controllable loads, and a cogeneration unit,” *IEEE Transactions on Industrial Electronics*, vol. 58, no. 10, pp. 4568–4582, 2011.